ABSTRACT

Title of dissertation: PARTICLE TURBULENCE INTERACTION OF SUSPENDED LOAD BY A FORCED JET IMPINGING ON A MOBILE SEDIMENT BED

Rahul Mulinti, Doctor of Philosophy, 2014

Dissertation directed by: Professor Ken Kiger
Department of Mechanical Engineering

Phase-resolved two-phase flow experiments have been conducted to predict particle suspension and sedimentation within coupled particle-laden flows relevant to rotorcraft brownout conditions. Single phase and dual-phase PIV experiments have been conducted to study the interaction of a mobile sediment bed with characteristic flow structures similar to those within a rotor wake. Even though sediment transport has been extensively studied in the past, the rapidly evolving transient nature of brownout calls many of the simplifying assumptions that have been made to understand sediment transport mechanisms into question.

Image intensity based phase-separation and a hybrid PIV/PTV techniques have been implemented to identify the gas and solid phases as well as to the resolve multi-valued velocity displacements within a given interrogation region. A calibration technique to identify the measurement volume using size-brightness as well as PIV correlation based criteria has been outlined. Simultaneous velocity measurements of the fluid and dispersed phase in two vertical co-planar planes are analyzed to examine the role of vortex interaction and its subsequent breakdown on sediment transport process. The mobilization conditions and wall-normal flux of particulates by the vortex-wall interaction are reported and are correlated to the local vortex conditions such as proximity to the wall and subsequent decay. The effect of the

changing sediment bed profile on sediment transport rates is also studied. Modulation of mean and stochastic fluid flow properties due to the presence of particles and the effect of turbulent coupling between the particle and fluid momentum, as based on a modified drag law with dependence on particle Reynolds number as well as local volume fraction has been examined. A mesoscopic Eulerian formalism has been implemented to study the effect of particle inertia on the suspension process.

PARTICLE TURBULENCE INTERACTION OF SUSPENDED LOAD BY A FORCED JET IMPINGING ON A MOBILE SEDIMENT BED

By

Rahul Mulinti

Dissertation submitted to the Faculty of Graduate School of the
University of Maryland, College Park in partial fulfillment
of the requirements for the degree of
Doctor of Philosophy
2014

Advisory Committee:
Dr. Kenneth Kiger, Advisor
Dr. J. Gordon Leishman
Dr. James Duncan
Dr. Johan Larsson
Dr. Michael Zachariah

Acknowledgments

I would like to sincerely thank my advisor and dissertation committee chair, Dr. Ken Kiger for his guidance and advice throughout the duration of my research. He has taught me how good experimental work in fluid mechanics is done. Working with him has been an intellectually enriching experience and I express my gratitude for giving me the opportunity to work with him on this challenging project. I would also like to thank Dr. J. Gordon Leishman, Dr. James Duncan, Dr. Johan Larsson and Dr. Michael Zachariah for sparing their valuable time to serve on my dissertation committee.

I would also like to thank my colleagues Jayson Geiser, Dana Ehyaei, Nate Washuta, Mary Larson, Kyle Corfman, Chang Liu and Farhad Saffaraval for extending their assistance. Dr. Anya Jones and her students have been very obliging and I really appreciate them for letting me use their equipment for some of the tests.

I also would like to express my deepest appreciation for my family. For my parents who raised me with a love of science and supported me in all my pursuits. For my sisters who have been unwavering in their support and encouragement throughout. This work would not have been possible without the constant comfort and encouragement of Soumya Chigurupati. She had to bear the brunt of my eccentricities and yet she has always been kind and caring while supporting me and even helping me with a couple of tests in the lab.

Finally, I would like to acknowledge the people working at the main office of Mechanical Engineering Department for making my life a lot easier by taking care of the administrative work. Thank you.

Rahul Mulinti
University of Maryland - College Park
July 2014

I would like to acknowledge the support of the Air Force Office of Scientific Research (AFOSR) under Multidisciplinary University Research Initiative Grant No. W9.

Contents

List of Figures

1 Introduction

Sediment suspension and transport due to the interaction of semi-coherent vortical flows with a mobile particulate bed has been studied extensively to understand a range of environmental and industrial applications. One of the important relevant applications that exemplifies sediment suspension and erosion by vortical structures is rotorcraft brownout, which is characterized by dust suspension that is uplifted during rotorcraft operations such as landing, takeoff or hover in a dusty environment (Fig. 1.1). The main flow features within the rotor wake are intense vortices shed from the tips of the rotor blades, which are advected in the downwash in a helical path and subsequently interact with the ground plane in a turbulent stagnation point flow. These structures undergo complex transient interactions when they encounter the sediment bed, which include vortex/vortex interactions, vortex bundling, generation of new vorticity, 3-dimensional instabilities, and viscous dissipation. The complexity of the phenomenon and the underlying mechanisms at play during the development of the brownout dust cloud are illustrated in Fig. 1.2.

Figure 1.1: Dust cloud formation around the landing zone under brownout conditions, image courtesy Leishman (2010) [1]

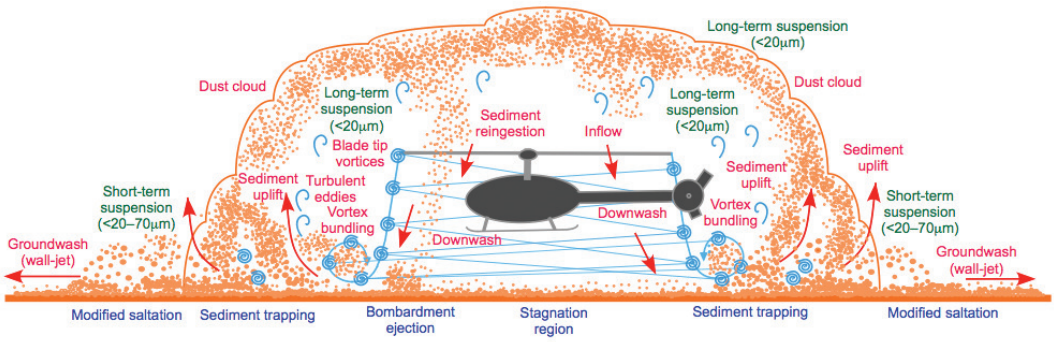

Figure 1.2: A schematic illustration of underlying mechanisms responsible for the formation and development of brownout dust cloud [2]

As the intensity of suspension increases, it creates several detrimental scenarios which can potentially lead to a severe mishap. The downwash from the main rotor is strong enough to suspend large amounts of dust as well as sand and the resulting dust cloud can severely impair pilot's visibility causing disorientation which can adversely affect his/her ability to successfully maneuver the rotorcraft. It has been observed that in a full-scale brownout dust cloud, the small suspended particles remain in suspension for long periods of time causing severe visual obscurity and making the landing zone unsafe for other rotorcrafts to operate. According to Department of Defense estimates, brownout conditions are the leading cause of human-factor related mishaps during military rotorcraft operations. Moreover, the suspended particles can get re-ingested by the rotor causing pitting damage on the blades, as well as sucked in by the engines causing significant wear on engine components. This can result in significant costs in terms of replacing parts and maintenance.

Several strategies including sensor technology to allow visual penetration of the dust cloud as well as specialized landing and takeoff maneuvers by pilots to outrun the dust cloud are currently being employed to improve flight safety under brownout conditions. These strategies have worked with

reasonable success but they have many drawbacks including but not limited to increased operational costs and increased risk to the pilot or the vehicle due to repetitive hard landings. Moreover, different rotorcrafts have different brownout signatures and it is not possible to successfully employ a single set of strategies that can improve operational safety under all possible brownout conditions. Therefore, it is highly desirable to find the root cause of the phenomenon and obtain a more feasible solution.

Mitigation of brownout requires a thorough understanding of the particle uplift behavior under brownout conditions as a function of wall/vortex interaction parameters and the initiation mechanisms of events like saltation and scouring. From a fluid mechanics perspective, brownout belongs to a broader class of unsteady multi-phase flows. Even though there have been several numerical as well as experimental studies on sediment transport mechanisms, the current models predicting particle motion are based upon assumptions of a quasi-equilibrium development, which are inadequate in predicting the suspension process in this highly transient flow. Rapid erosion of sediment, and formation of topographic structures on comparatively short time-scales can potentially alter the boundary conditions from a nominally planar surface in significant ways, leading to a coupling between the evolution of the air and sediment phases.

The primary focus of this project is to measure and understand the particle suspension mechanisms within the rotor wake. Large emphasis is placed on quantifying particle/turbulence interaction within the suspended load which is necessary for the formation of the dust cloud. Depending on the local volume fraction of suspended particles, there can potentially be two-way or four-way coupling between the two phases involved. Two-phase flows are notoriously difficult to study using experimental techniques as intrusive mea-

surement methods tend to modify the flow pattern and fragile instruments like hot-wires are not suitable to measure velocities due to the presence of particles. Two-dimensional experimental data is even rare given that most experimental techniques provide point measurements. Particle Image Velocimetry (PIV) has been widely used since early 90s to study multi-phase flows, however, each experimental study has a relatively narrow scope. This work aims to provide an unprecedented assessment of the particle dynamics under replicated brownout conditions, giving a measure of the particle concentration, velocity and flux, in conjunction with the corresponding unsteady fluid structure and statistics. To that end, two-phase PIV experiments have been conducted to measure the velocities of both phases simultaneously as well as obtain local volume fractions within the flow.

The organization of the thesis is as follows:

In chapter 2, a background on multi-phase flows including major relevant parameters will be provided. A brief overview of theoretical, numerical and experimental work conducted on both steady and unsteady multi-phase flows will also be provided.

Chapter 3 focuses on experimental setup and parametric space used in this study. A brief description of data acquisition methods and processing algorithms as well as validation methods will be given.

Chapter 4 outlines a novel calibration method to estimate the measurement volume for multi-phase PIV experiments. Two approaches, one based on size-brightness criteria and the other based on PIV correlation will be discussed.

Chapter 5 will go over the results from single phase and two-phase ex-

periments. Detailed description of observed phenomena as well as comparisons to existing models in literature will be provided.

The final chapter will include a brief summary of the research, important conclusions drawn from the results and scope for future work in this field.

2 Background and Motivation

Two-phase flows are ubiquitous both in nature as well as in industry, yet there are large gaps in our current understanding of these flows. This chapter will provide some insight into the basic concepts of multi-phase flows, relevant parameters as well as models that have been proposed to predict particle uplift mechanisms and particle-turbulence interactions. Different theoretical, numerical and experimental approaches that have been used to understand multi-phase flows will be outlined. Finally, the necessity to pursue more advanced studies to understand the underlying physics in unsteady multi-phase flows such as rotorcraft brownout will be justified.

2.1 Sediment transport from a bed

In general, Aeolian particle transport is characterized by three modes: 1) creep, in which particles roll along the boundary; 2) saltation, in which stochastic stress events are sufficient to temporarily lift a particle and initiate a bouncing trajectory but are insufficient to fully suspend the particle; and 3) suspension, where the particles become fully suspended in the turbulent flow. Saltation plays a critical role, as the impact of heavier particles often supplies the necessary energy for disrupting the cohesive forces binding the smaller dust particles into aggregates, hence circumventing the larger hydrodynamic stress required to initiate their motion. For sheet flows, the near bed region is crucial but measurements are difficult due to the small size and the relatively high sediment concentration. In particular, the presence of sediment renders most acoustic and optical methods inaccurate. Early experiments in sediment transport were made using suction samplers and pitot tubes away from the bed surface. Mea-

surements close to the bed surface were very difficult to measure and the bed load transport was measured using bed load traps.

2.1.1 Threshold models

In sediment transport two important concepts are settling rate and boundary layer shear stress. Settling rate describes the tendency for sediment particles to fall out of suspension, and boundary layer shear stress describes the tendency for moving fluid to bring sediment particles into suspension. Some of the earliest experiments on sediment and granular flows were conducted on interaction of wind with sand dunes. Thresholds for sediment erosion were arrived at from experiments conducted in steady turbulent channel flows where the mean flow and friction velocity are well defined. Shields (1936) [4] proposed that there exists a threshold wind velocity below which no particle motion occurs along a sediment bed unless there is an external auxiliary force other than the steady wind. One of the widely used criteria used to describe this incipient particle motion from a sediment bed is Shields parameter which is effectively the ratio of hydrodynamic lift to the buoyancy force.

$$\Theta = \frac{\rho_f u^{*2}}{(\rho_p - \rho_f) g d_p} \quad \text{where} \tag{1}$$

ρ_f and ρ_p are the fluid and particle densities respectively, u^* is the fluid friction velocity given by $u^* = \sqrt{\frac{\tau_b}{\rho_f}}$, τ_b is the bed shear stress and d_p is the mean particle diameter. The mechanism can be viewed either as the minimum shear stress needed to move a given particle, or as the largest grain size that can be moved by a given shear stress. Another important parameter that is relevant

from a scaling perspective is friction Reynolds number defined as:

$$Re^* = \frac{u^* d_p}{\nu} \quad \text{where} \tag{2}$$

ν is the fluid kinematic viscosity. Shields conducted experiments and fitted a curve to show the dependence of critical Shields parameter Θ_c and Re^* (Fig. 2.1). The curve forms the boundary in the parametric space where incipient particle motion is possible.

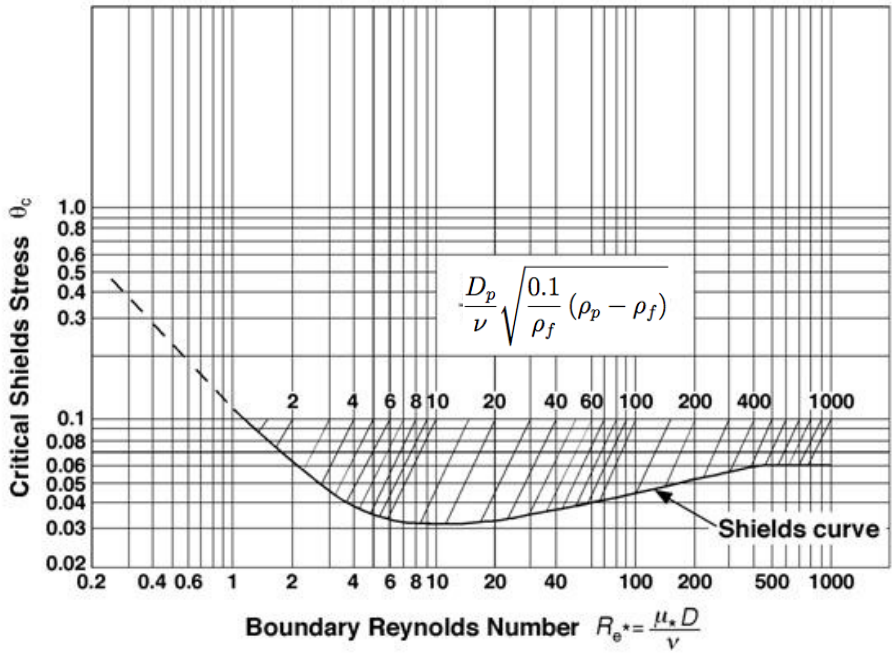

Figure 2.1: Shields curve for sediment transport [4]

Once the particles enter suspension due to entrainment by fluid turbulence, there exists a threshold criteria to keep these particles in suspension. Bagnold (1966) [3] proposed that the vertical velocity of fluid should be equal to or greater than the particle fall velocity (W_s), which is expressed by another parameter:

$$\Theta_s = 0.64 \frac{\rho_f W_s^2}{(\rho_p - \rho_f) g d_p} \tag{3}$$

Later studies showed that these models can be correlated with a functional form dictated by aerodynamic, gravitational, and inter-particle cohesive forces ([5], [6]). The threshold velocity models can be applied for statistically steady flows where a well defined friction velocity u^* can be defined under the assumption of a logarithmic boundary layer. This severely limits the application of threshold velocity models to predict particle motion in unsteady multi-phase flows such as brownout.

2.1.2 Sediment transport rate

Sediment transport mechanisms are classified into two modes depending on the proximity of bed with the suspended particles: a) bed load and b) suspended load. The bed load transport occurs close to the surface of the bed where the particles are scouring, saltating and rolling along the bed surface. Particle-particle and particle-bed interactions play a dominant role in this relatively thin region of high particle volume fraction where bed shear stress plays an important role. Away from the bed, fluid-particle interactions become dominant and the different regimes in this mode are outlined in a later section. The rate of sediment transported (Q_T) from a bed is the summation of sediment concentration multiplied by the particle velocity within the flow domain. The total amount of sediment discharge is usually segregated into bed load (Q_B) and suspended load (Q_S).

Meyer-Peter and Müller (1948) [7] measured the bed load transport rate Q_B using bed load traps and came up with an empirical relationship between critical Shields parameter Θ_c and Q_B:

$$Q_B = \begin{cases} m(\Theta - \Theta_c) & \text{if } \Theta \geqslant \Theta_c \\ 0 & \text{if } \Theta \leqslant \Theta_c \end{cases} \tag{4}$$

where m=8. Wilson (1966) [8] also conducted the same experiment under sheet flow conditions ($\Theta > 1$) and came up with a value of m=12.

Bagnold [3] modeled the suspended load transport rate by integrating the product of concentration and particle velocity:

$$Q_s = \int_{z_0}^{h} c(z) u_p(z) dz \quad \text{where} \tag{5}$$

z_0 is the lower limit of the suspension layer and h is the height of the flow domain. It is critical to choose an accurate boundary between the bed load layer and suspended load layer in order to model the sediment transport rate precisely. These models have been extended to oscillatory flows [9] by incorporating a time-dependent Shields parameter. It is imperative to note that these empirical models are based on highly simplified assumptions and do not provide a comprehensive picture of physics behind the phenomenon, hence have a limited range of applicability.

2.2 Particle-Turbulence Interactions

In order to understand particle-turbulence interactions, classification has been made based on the volume or mass load [10]. Concentration is defined as the ratio of total number of suspended dispersed phase particles to the volume of the domain in which they are suspended:

$$c = \frac{n_p}{L^3} \tag{6}$$

The volume fraction (Φ_v) can be obtained by multiplying the concentration with the volume of individual particles.

$$\Phi_v = \frac{\pi}{6}\frac{n_p d_p^3}{L^3} \quad \text{where} \tag{7}$$

n_p is the number of particles suspended in a volume of L^3.

The interaction or coupling between the two phases involved is then classified as:

1. **One-way coupling:** In this regime, the effect of particles on fluid phase is negligible and the particles behave as non-ideal tracers following all, some or none of the fluid motion. Existing literature[11] states that this regime ends at $\Phi_v \approx 10^{-6}$. The fluid and particle equations of motion can be solved separately in this regime.

2. **Two-way coupling:** In this regime, the particle motion affects fluid phase resulting in augmentation or attenuation of fluid turbulence levels depending on particle characteristics. The range in which this regime is active is $10^{-5} < \Phi_v < 10^{-2}$. The fluid and particle equations of motion have to solved simultaneously and this coupling phenomenon can cause preferential concentration regimes within the flow domain [12].

3. **Four-way coupling** As the particle volume load is further increased, particle-particle interactions (collisions and hydrodynamic interactions) come into play. This regime is most commonly found in fluidized bed reactors.

Inter-phase momentum transport can be estimated by calculating the forces experienced by particles in suspension. Appropriate modeling of the forces exerted on the particle by the fluid and the resulting feedback from

the particle to the fluid via Newton's third law of motion forms the basis for understanding momentum exchange in two-phase flows. In general, drag, added-mass and Bassett history force due to the presence of particles are considered ([13], [14]). The non-dimensional velocity for the suspended load is given by the particle Reynolds number based on particle slip velocity.

$$Re_p^i = \frac{|u_f^i - u_p^i| d_p}{\nu} \tag{8}$$

where u_f and u_p are fluid and particle velocities respectively. The drag law can be used to describe the forces exerted on the particles by the fluid. For $Re_p < 0.5$ and dilute flows, Stokes regime or creeping flow approximation can be made and the drag force is given by:

$$\boldsymbol{F_d} = 3\pi\rho_f \nu n_p d_p (\boldsymbol{u_f} - \boldsymbol{u_p}) \tag{9}$$

In general, if the concentration of the particles is higher, the drag coefficient is dependent on both the concentration and Reynolds number as estimated by Richardson and Zaki (1954) [15]:

$$\begin{aligned} \boldsymbol{F_d} &= \Phi_v C_d (\boldsymbol{u_f} - \boldsymbol{u_p}) \quad \text{where} \\ C_d &= \frac{\rho_f \nu}{d_p^2} \left(18.0 + 0.3 Re_p\right) \frac{1}{(1-\Phi_v)^n} \end{aligned} \tag{10}$$

The factor n depends on the particle Reynolds number as follows:

$$n = \begin{cases} 4.35 Re_p^{-0.03} - 1 & 0.2 \leqslant Re_p \leqslant 1.0 \\ 4.45 Re_p^{-0.1} - 1 & 1.0 \leqslant Re_p \leqslant 500 \\ 1.39 & 500 \leqslant Re_p \end{cases} \tag{11}$$

If the effect of finite Reynolds number and added mass is neglected, a particle

relaxation time can be estimated as:

$$\tau_p = \frac{\rho_p}{\rho_f} \frac{d_p^2}{18\nu} \tag{12}$$

For the fluid phase, the characteristic time scale is based on Kolmogorov scale,

$$\tau_k = \frac{\eta^2}{\nu} \quad \text{where} \tag{13}$$

η is the Kolmogorov length scale. One of the most important non-dimensional parameters used to describe particle-fluid interaction is the Stokes number, which can then be defined as the ratio of particle time scale to the fluid time scale.

$$St = \frac{\tau_p}{\tau_k} \tag{14}$$

Particles with low Stokes number follow fluid streamlines (perfect advection) whereas for large Stokes number, the particle's inertia dominates so that the particle will continue along its initial trajectory.

The other terms in the two-phase momentum equation are the added mass and lift force as outlined by Drew (1983) [13]:

$$\begin{aligned} F_a^i + F_l^i = {} & \rho_f \Phi_v C_M \left(\frac{\partial u_f^i}{\partial t} + u_p^i \frac{\partial u_f^i}{\partial x^j} - \frac{\partial u_p^i}{\partial t} u_f^j \frac{\partial u_p^i}{\partial x^j} \right) \\ & + \rho_f \Phi_v C_M (1 - \lambda_{fs}) \left(u_f^j - u_p^j \right) \frac{\partial \left(u_f^i - u_p^i \right)}{\partial x^j} \\ & + \rho_f \Phi_v C_L \left(u_f^j - u_p^j \right) D_f^{ij} \quad \text{where} \end{aligned} \tag{15}$$

C_M and C_L are the added-mass and lift coefficients respectively, λ_{fs} is a parameter and D_f^{ij} is the fluid strain tensor given by:

$$D_f^{ij} = \frac{1}{2} \left(\frac{\partial u_f^i}{\partial x^j} + \frac{\partial u_f^j}{\partial x^i} \right) \tag{16}$$

2.2.1 Numerical Studies on Particle-Turbulence Interactions

Using DNS, Squires and Eaton (1990 and 1994) [16, 17] studied particle motion in Stokes regime in a statistically stationary, homogeneous, isotropic turbulence. They found that increasing particle mass loading decreased total fluid kinetic energy at small wave members where most of the energy is stored. Elghobashi and Truesdell (1993) [11] examined particles in decaying isotropic turbulence. They found that coupling between the phases led to an increase in turbulent energy at large wave numbers compared to the energy at small wave numbers. They also concluded that the large wave number kinetic energy for a flow with particles is higher compared to the large wave number energy for single phase fluid flow at the same time during the decay process. Squires and Eaton [17] attributed turbulence modulation to preferential concentration of particles in the turbulent flow field. They showed that particles with small response time ($St << 1$) show high tendency for preferential concentration in regions of low vorticity and high strain rate which in turn leads to an increase in small-scale turbulent velocity fluctuations. These small scale velocity fluctuations subsequently cause viscous dissipation in the carrier fluid. Boivin et al. (1998) [18] made detailed DNS studies of modulation of statistically stationary, homogeneous and isotropic turbulence by particles. They found that particles with both high and low response times had a damping effect on smaller wave numbers of the fluid turbulence. At larger wave numbers, the turbulence kinetic energy is damped by particles with a large response time while the particles with small response time augmented the fluid turbulence kinetic energy.

Gravity and buoyancy also play an important role in sediment flows. Dritselis and Vlachos (2008) [19] found that addition of particles into turbulent

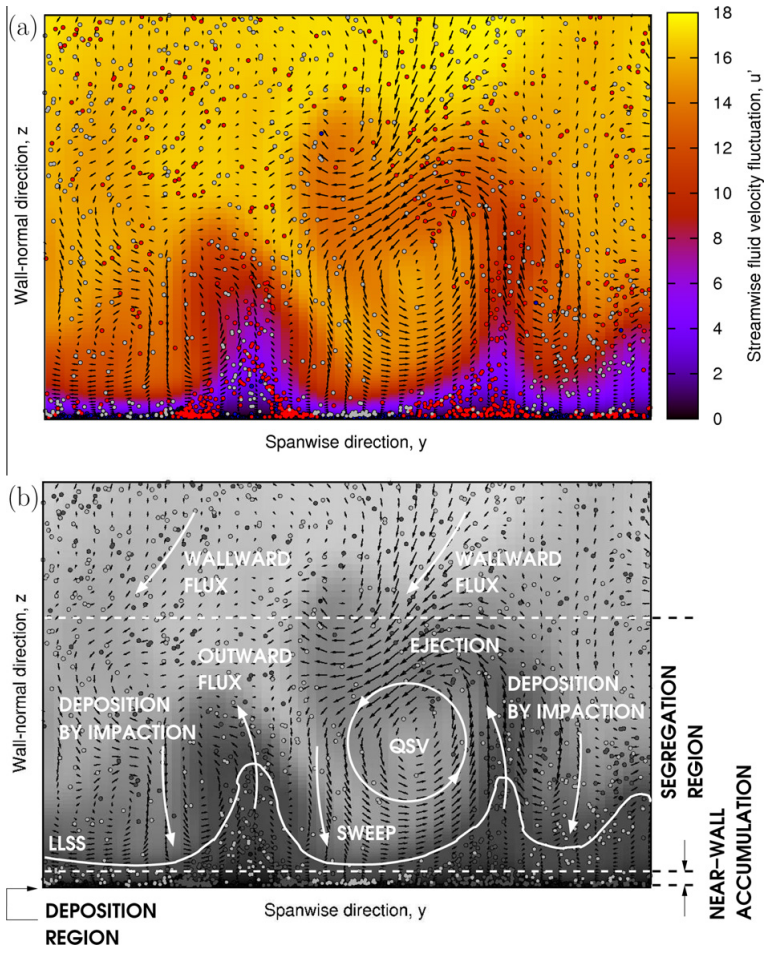

Figure 2.2: a) DNS simulations of instantaneous flow field and sediment distribution in near-wall regions of high concentration b) Sediment transport mechanisms (Soldati and Marchioli) [22]

channel flows alters the length scales and strength of quasi-streamwise vortices that vary with the orientation of the channel indicating the strong effect of gravity as well as buoyancy on these interactions. Introducing unsteady features into the flow such as waves or oscillations increases the complexity of the problem. Amoudry et al. (2008) [20] used a modified $k-\epsilon$ closure model that incorporated additional physics of particle-fluid interactions. They used concentration weighted averages of velocities and were able to match their results with experimental data under sheet flow as well as oscillatory flow conditions,

while resolving the transitions from the stationary bed to the collisional granular flow and the the turbulent suspension regime.

Ozdemir et al (2010) [21] conducted simulations of fine sediment transport in oscillatory boundary layer using pseudo-spectral flow solver and DNS. The flow was dilute enough that there was no modulation of the carrier phase by the suspended particles. Soldati and Marchioli (2012) [22] examined the limitations of the current state-of-the-art in DNS and LES of sediment dynamics in turbulence. They focused on sediment transport mechanisms near the bed where the concentration is typically high (Fig. 2.2) and evaluated numerically critical conditions where local high concentration violates the one-way coupling assumption as well as the significant fluctuations in particle concentration that may not be represented by a single volume-averaged indicator. They concluded that current capabilities of LES in predicting dispersed flows are strongly limited by the modeling of the sub-grid scale turbulence effects on particle dynamics, and that further efforts must be taken in this direction. Accurate two-way coupling formulations where turbulence modulations by sediment are incorporated via density stratification and higher order inertia effect, are still under development.

2.2.2 Experimental Studies in Turbulent Open Channels

There have been several experimental studies in the recent years investigating the effect of addition of particles on bulk velocities, turbulence intensities and associated energy spectra of homogeneous isotropic channel flows. Sheet flows and oscillatory flows have been extensively studied using experimental methods, mostly from coastal sediment dynamics perspective.

Sumer and Oğuz (1977) [23] used a moving camera system to observe

motion of heavy suspended particles in an open channel. They proposed that particle lift-up from the bottom is a result of the temporary local adverse pressure gradient which is imposed on the particle by a burst passing overhead. According to this mechanism, the rise of the lifted particle is strongly controlled by the bursting flow structure, which enters the main body of the flow together with the particle owing to the same adverse pressure gradient. Niño and Gracia (1996) [24] used a high speed video system to study particle-turbulence interactions in the near-wall region for smooth and transitionally rough beds at Reynolds numbers less than 30000. They noticed formation of wall streaks in the smooth channel, which were attributed to the presence of counter-rotating quasi-streamwise vortices. These vortices led to particle sorting along low-speed streaks when the particle sizes are less than the thickness of viscous sublayer. In the case of a rough boundary, the roughness elements disrupt the structure of the viscous sublayer, and although the wall streaks also develop in these conditions, they lose coherence, persistence, and spatial extent. They found that the intensity of flow ejections responsible for particle suspension increased with the bed shear stress.

Kiger and Pan (2002) [25] conducted PIV experiments in a horizontal water channel with a centerline velocity of 0.6 m/s over a bed of 200 μm glass particles. They showed that presence of the particles noticeably alters the carrier phase turbulence properties through an effective increase in the wall friction velocity of approximately 7%, and an increase of the normal and shear Reynolds stress by approximately 8-10% in the outer flow (Fig. 2.3).

Hout (2011) [26] studied the spatio-temporal interaction of near-neutrally buoyant polystyrene beads with coherent near-wall structures using time-resolved PIV in a horizontal water channel. He speculated that the absence of enhancement of turbulent kinetic energy of the fluid is due to vortex shedding by

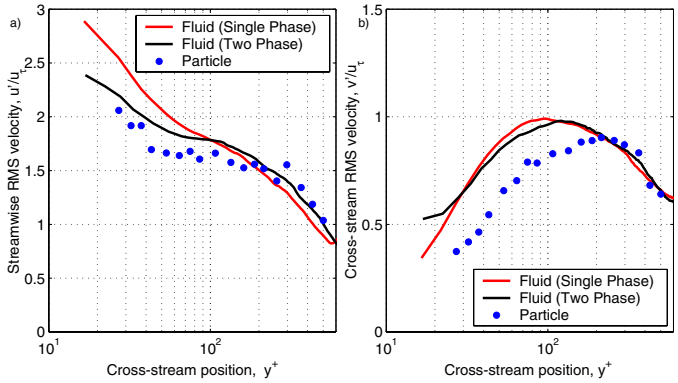

(a) Streamwise and wall-normal turbulent stress profiles of the fluid (with particles present) the dispersed phase particles and the clear (single-phase) fluid. (Kiger and Pan 2002) [25]

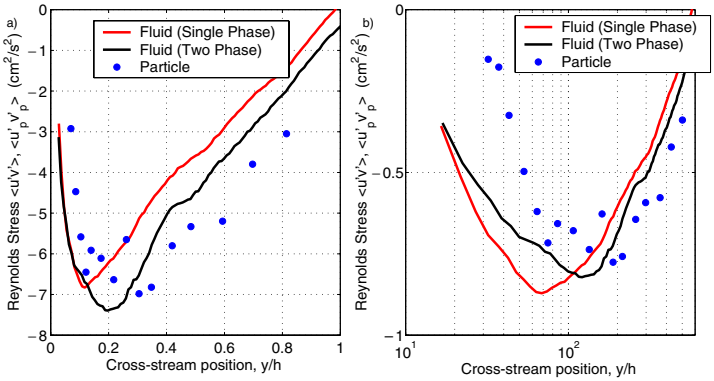

(b) Reynolds stress profiles of the fluid (with particles present) the dispersed phase particles and the clear (single-phase) fluid. (Kiger and Pan 2002) [25]

Figure 2.3: Effect of presence of particles on turbulent stress and Reynolds stress

the particles is caused by low particle Reynolds numbers in the experiments ($Re_p < 100$). In this neutrally-buoyant scenario, the particles ascending from the wall were transported upwards by the slow moving ejections while the descending particles were moving at similar stream wise fluid velocity. More recently, Li et al. (2012) investigated turbulence modification of a dilute gas-particle flow in the boundary layer. They found that addition of particles changes the turbulence intensities and mean velocities even at very low volume fractions. They also found that the mean stream-wise fluid velocity is increased close to the wall while it reduced away from the wall due to particle

inertia (Fig. 2.4).

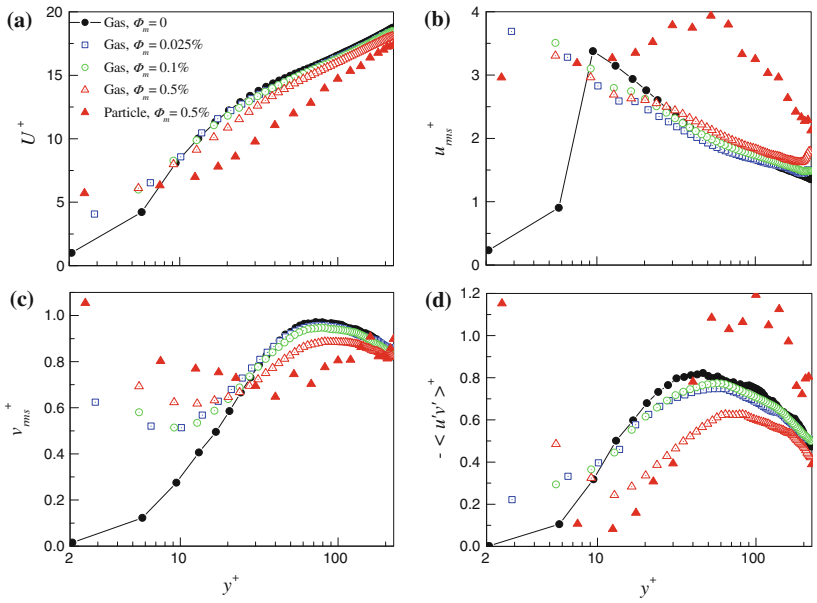

Figure 2.4: Distribution of a) mean fluid velocity b), c) RMS velocities and d) Reynolds stress in wall-coordinates at different mass fractions (Li et at 2012) [27]

2.3 Vortex impingement on sediment layer

There have been few studies over the years on the interaction of quiescent vortex rings with sediment beds. The creation of vortex rings from orifices or tubes represents a robust, repeatable, and easily conducted experiment. Although this model problem differs from the interaction of naturally occurring flows with particle layers, an improved understanding of the mechanisms that govern the resuspension of particles by a vortex ring will shed light on more complicated flows. A vortex ring's circulation and impulse are well defined and measurements of velocities and vorticity can be achieved with methods such as particle image velocimetry (PIV). Furthermore, the existence of an analytical solution for the inviscid flow field generated by a translating vortex ring in the presence of a solid boundary allows for a systematic investigation

of the effects of a particle layer on the flow field. Sutherland (1967) was the first to qualitatively study the interactions of channel flows with pulsating jets and vortex rings with particle layers. Sutherland discovered that the viscous sub-layer is disrupted as a coherent vortex approached the sediment layer, resulting in an increase in the local shear on the surface. He then suggested that an exposed particle can be expected to be lifted up from the bed when the vertical component of the drag force associated with the eddy exceeds the particle's immersed weight plus any forces arising from interference with neighboring grains. Chung and Trout (1988) [29] studied particle dispersion in an axisymetric jet following particle trajectories in a jet flow simulated by discrete vortex rings. The found a strong correlation between particle dispersion and the ratio of particle response time and the characteristic time of the jet flow or in other words, Stokes number with the fluid time scale based on mean jet characteristics. Their simulation indicated that there exists a specific range of Stokes numbers, at which optimal dispersion of particles in the turbulent mixing layer of an axisymmetric free jet may be achieved.

More recently, Munro et al. (2009) [30] also confirmed that intense vortical flow establishes local regions of high shear adjacent to the bed surface exposing the near-surface sediment grains to greater hydrodynamic drag and lift forces. They also studied the erosion characteristics of a solitary vortex ring impinging on a mobile sediment bed made of particles of different size classes. Based on erosion patterns left on the sediment bed, it was shown that the particles are primarily displaced by the radial velocity component while the azimuthal instabilities resulted in asymmetric small-scale scaring features on the bed surface. They also showed that the effects of viscous damping were found to be significant for $d_p/\delta < 15$, where δ denotes the viscous sublayer thickness. Bethke and Dalziel (2012) [31] continued this work

and found that the velocity induced above the particle layers matched the inviscid velocity obtained from the line vortex model, indicating a free-slip boundary on the surface. Their results also suggest that the particle layer permeability influences the induced bed velocity as it admits a flow through the interface and therefore within the bed, which may affect the growth and detachment of the boundary layer as well as the magnitude of the bed velocity.

2.4 Rotorcraft brownout

While it is imperative to understand the phenomenon of full-scale rotorcraft brownout, it is difficult to extract details of the mechanisms involved in the actual entrainment of the particles at this scale. To overcome the problem arising due to scale and to have control over the environment, several studies have focused on studying single and two-phase flowfields around laboratory-sized rotors. Nathan and Green (2008) [32] conducted two-phase PIV and flow visualization experiments using a micro-rotor to study particle suspension and subsequent entrainment by the rotor downwash and the tip vortices under different operating conditions. They used talcum-powder as dispersed phase and found that these particles tend to accumulate near regions of high vorticity (Fig. 2.5).

Johnson et al. (2009) [33] performed both single and two-phase simulations of the flow environment induced by a small-scale rotor hovering above a sediment bed. High-resolution, near-wall, PIV measurements showed large excursions in the boundary layer velocity profiles due to the presence of the convecting vortices. The highest sediment entrainment levels were seen to occur at regions where the vortices were closest to the ground since this resulted in increased groundwash and wall shear in those regions. In addition, this

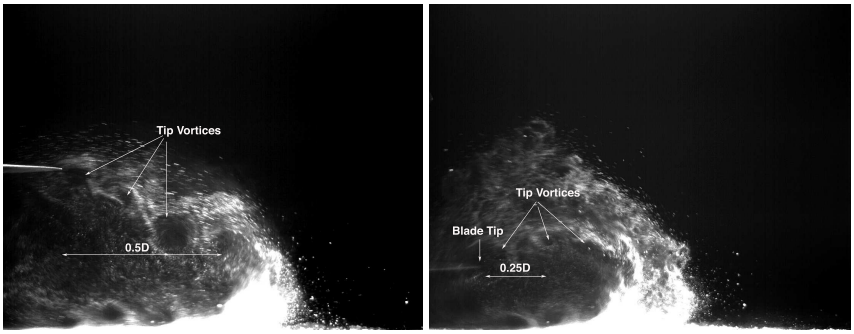

Figure 2.5: Stills from high speed video sequences of simulated brownout. a) Rotor operating at a distance 0.5D above the ground b)Rotor operating at 0.25D above the ground (Nathan and Green 2008) [32]

study observed the highly aperioidic phenomena of vortex pairing and merging of adjacent turns of the blade tip vortices. These phenomena were found to play a key role in increasing local induced velocities, and consequently shear stresses, at the ground plane, which in turn increased initial mobilization and uplift of particles from the bed. Sydney et al. (2011) [34] performed similar experiments using 1- and 2-bladed rotors and identified different particle mobilization and suspension mechanisms within the rotor wake:

1. **Creep** - particles moving slowly along the bed surface
2. **Modified saltation bombardment** - uplifted particles return to the bed and upon impact, eject more particles
3. **Vortex trapping** - uplifted particles entrained by the vortices
4. **Unsteady pressure effects** - particles are uplifted in a direction perpendicular to the direction of jet flow due to a pressure gradient between the sediment bed and the vortex core
5. **Reingestion bombardment** - uplifted particles are accelerated around a vortex and then fall back to the ground causing the release of more particles from the sediment bed

6. **Secondary suspension** - particles are kept in suspension by being transferred from one vortex to the next

Over the last few years, researchers modeling brownout have employed aerodynamic models of various levels of sophistication. Syal et al. [2] performed computational analysis of full-scale rotorcraft brownout clouds using a sediment tracking algorithm coupled with a time- accurate, free-vortex method (FVM) with an image plane to simulate the ground. Thomas (2013) [35] implemented a hybrid Eulerian-Lagrangian methodology to help better understand the rotorcraft brownout environments. His dual-phase simulations were able to resolve key transport phenomena in the dispersed phase such as creep, vortex trapping and sediment wave formation.

2.5 Aim of this work

Very little physical understanding in terms of laboratory scale experiments has been obtained about the mechanisms that govern sediment transport in these types of complex vortical flows. As illustrated above, there are a number of semi-empirical models relating the rate of sediment transport to flow parameters like bed shear stress and friction velocity. However, in the case of brownout, rapid erosion of sediment, and formation of topographic structures on comparatively short time-scales can potentially alter the boundary conditions from a nominally planar surface in significant ways, leading to a coupling between the evolution of the air and sediment phases. The coherence of the vortex will allow it to focus that energy in a highly localized and violent interaction at the bed surface.

This work examines the influence of the mean fluid motion on particle

suspension mechanisms and the role of vortex impingement and its subsequent dissipation on particle flux. Flow visualization and particle image velocimetry techniques have been used used to understand and quantify the behavior and microscale physics of the suspension and turbulence interaction problem. The results will be used to determine and validate the appropriate constructs for the modeling of the sediment entrainment. Evolution of bed surface over time has been examined to gain insight into locations of high shear on the bed surface along with the formation of topological structures on the surface and their influence on particle suspension. The spatial distribution of the particles and its effect of the carrier phase has also been examined. The effect of particle volume fraction and slip velocity on the mean and fluctuating drag fields within suspension will be reported.

3 Experimental Setup, Data Acquisition and Processing

3.1 Experimental Setup

Rotorcraft flows in general are extremely complex; the base flow consists of a downwash jet bounded by coherent tip vortices shed from the ends of each rotor blade (Fig. 3.1). The generation and induced motion of these vortices leads them to form in a helical pattern, which induces a swirl component to the downwash. There is also sheet vorticity emanating from the span on the rotor which also convects towards the ground, sometimes assimilated by the tip vortex depending on working conditions. In order to understand the more basic physics of the suspension process, the coherent tip vortices can be approximated as vortex rings convecting towards the ground. In the current work, an impinging wall-jet is forced by modulating the flow at the exit plane to produce a highly coherent vortex ring (Fig. 3.2). This is achieved by acoustically forcing the jet within the supply plenum of a vertical wind tunnel using a loud speaker. While this flow retains the essential features of a coherent vortex embedded within an axisymmetric stagnation flow, a significant difference is that the rings themselves are nominally axisymmetric, and not helical as would be the case in a rotorcraft wake. The objective is to generate repeatable coherent vortex rings superimposed within an axisymmetric stagnation point flow in the presence of a mobile sediment bed.

A 12″ 2000W subwoofer has been used as the forcing loudspeaker for the jet, using a pure tone harmonic signal as the forcing input. In order to match velocity conditions and circulation strength found in an actual micro-

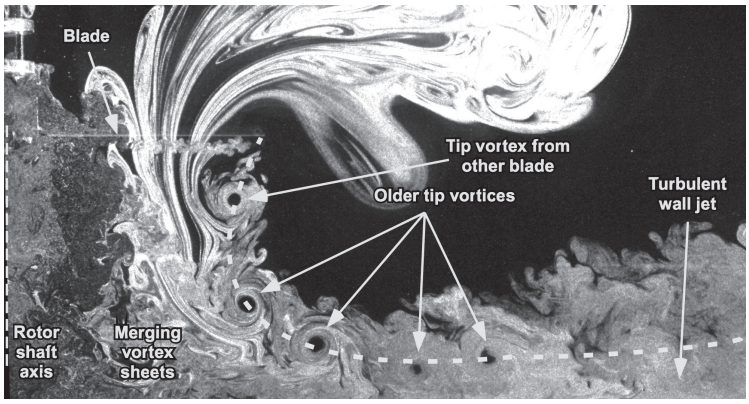

Figure 3.1: Flow visualization of tip vortices shed from a single bladed rotor, image courtesy Leishman (2010) [1]

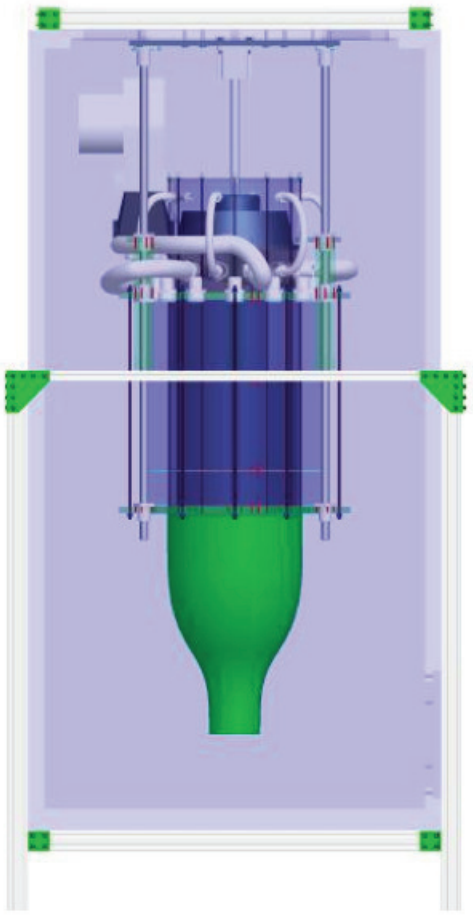

Figure 3.2: Schematic of the experimental setup

rotor setup [1], a parametric study has been conducted to establish the operating point for this setup in terms of the mean axial jet velocity, the forcing

amplitude and forcing frequency. The blower of the wind tunnel is driven by a LABVIEW virtual instrument supplying a DC voltage, while the subwoofer is powered by a function generator that generated sinusoidal waves with a given amplitude and frequency. The output velocity at the nozzle is estimated initially with a pitot probe while monitoring the pressure drop in the wind tunnel. This served as a calibration criteria between the input voltage to the blower and the output velocity at the nozzle exit. The experimental facility has been extensively tested by conducting single phase experiments under various operating conditions. Detailed experimental parameters and corresponding results are illustrated in Geiser et al (2011) [36]. The conditions for the tests reported here correspond to a mean jet exit velocity of about 4.1 m/s, which is chosen based on observations of incipient particle motion along the bed surface while using an unforced jet. Superimposed over this jet is a pressure fluctuation produced by the loudspeaker that is forced at a frequency of 35 Hz. The frequency is chosen to be very close to the frequency of the natural vortex shedding due to Kelvin-Helmholtz instabilities at the nozzle edge, so that the vorticity embedded in the shear layer can be effectively rolled up into these naturally shed vortices. The amplitude of the forcing was adjusted to give velocity fluctuation amplitude of $\pm 4m/s$ about the mean jet velocity. These conditions resulted in a similar circulation strength of the vortices generated by the micro-rotor setup reported by Johnson et al [1] in their studies. The diameter of the vortex core in a typical full-scale rotorcraft is about 1/100 the diameter of the rotor. The diameter of the vortex core generated by this setup is about 1/10 of the diameter of the nozzle. So the length scales of the flow are not matched, however, the mechanisms governing particle suspension and particle-turbulence interaction would be similar in both the cases.

The jet was positioned 2 jet nozzle radii (R = 5 cm) above a 1.5 cm

thick sediment bed (See Table 3.1). The sediment bed is comprised of loosely packed glass spheres that have been sifted and heated to remove clumps as well as moisture. Several size classes have been tested for their regularity in size and shape as well as mobility under current working conditions (Fig. 3.3). It has been found that the particles of size class 45-63 μm, manufactured by Mo-Sci Corporation performed favorably under current test conditions. When the particle size goes below this range, the cohesive forces due to van der Waals attractive forces as well as electrostatic forces become dominant and there is a substantial departure from the free flowing particulate systems. On the other hand, if the particle size increases, inertia effects dominate and higher critical stress is required to induce motion.

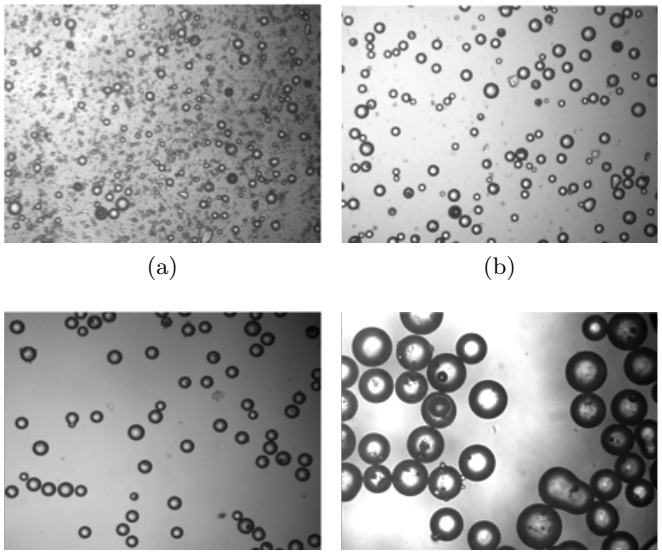

Figure 3.3: (a) Unwashed batch of 35-45 μm particles (b) Washed 35-45 μm particles (c) 45-63 μm particles, (d) 125-150 μm particles.

Table 3.1: Flow conditions and particle characteristics

Nozzle Radius, (R, cm)	5
Mean jet exit velocity (V_o, ms^{-1})	4.1
Forcing frequency (n, Hz)	35
Velocity fluctuation $(\Delta V, \text{ms}^{-1})$	± 4
Fluid density $(\rho_f, \text{kgm}^{-3})$	1.2
Particle density $(\rho_p, \text{kgm}^{-3})$	2500
Particle mean diameter $(D_p, \mu\text{m})$	50
Thickness of sediment bed (h, cm)	1.5
Standoff height (H, cm)	10

3.2 Data Acquisition

Phase resolved particle imaging velocimetry (PIV) has been used to study the particle dynamics under replicated brownout conditions, giving a measure of the particle concentration, velocity and flux, in conjunction with the corresponding unsteady fluid structure and statistics. A single camera two-phase PIV system has been implemented to quantitatively study this flow field. The light source used in these experiments is a Litron Nano-L PIV laser operating at 532 nm. Two 2048×2048 pixel, 14 bit CCD cameras (LaVision Imager Pro X4M) have been used to capture the composite two-phase PIV images. A vertical imaging plane directly beneath the tip of the nozzle has been used to characterize the single phase flow emanating from the nozzle. Two-phase data has been recorded in two overlapping co-planar vertical planes; an upstream plane close to the stream-wise location where the vortices rebound after the initial impact and a downstream plane where the vortex undergoes a rapid three-dimensionalization and dissipation due to its interaction with the ground plane and suspended particles (Fig. 3.4). The field of view in both planes is $5.8cm \times 5.8cm$, using a Nikon 80-200mm $f/4$ ED AF Zoom Nikkor lens with the aperture set to $f/8$. The left edge of the upstream plane is about 3 jet nozzle radii away from the center of the nozzle. The light sheet is about 1.5

mm thick in the field of view. The imaging system is phase locked with the forcing cycle of the speaker and images were recorded at 8 phase angles for each plane. A delay time of 50 μs between the two frames of each image pair has been used for the PIV measurement, which was selected as a compromise between the higher-speed fluid motion and the slower suspended particles.

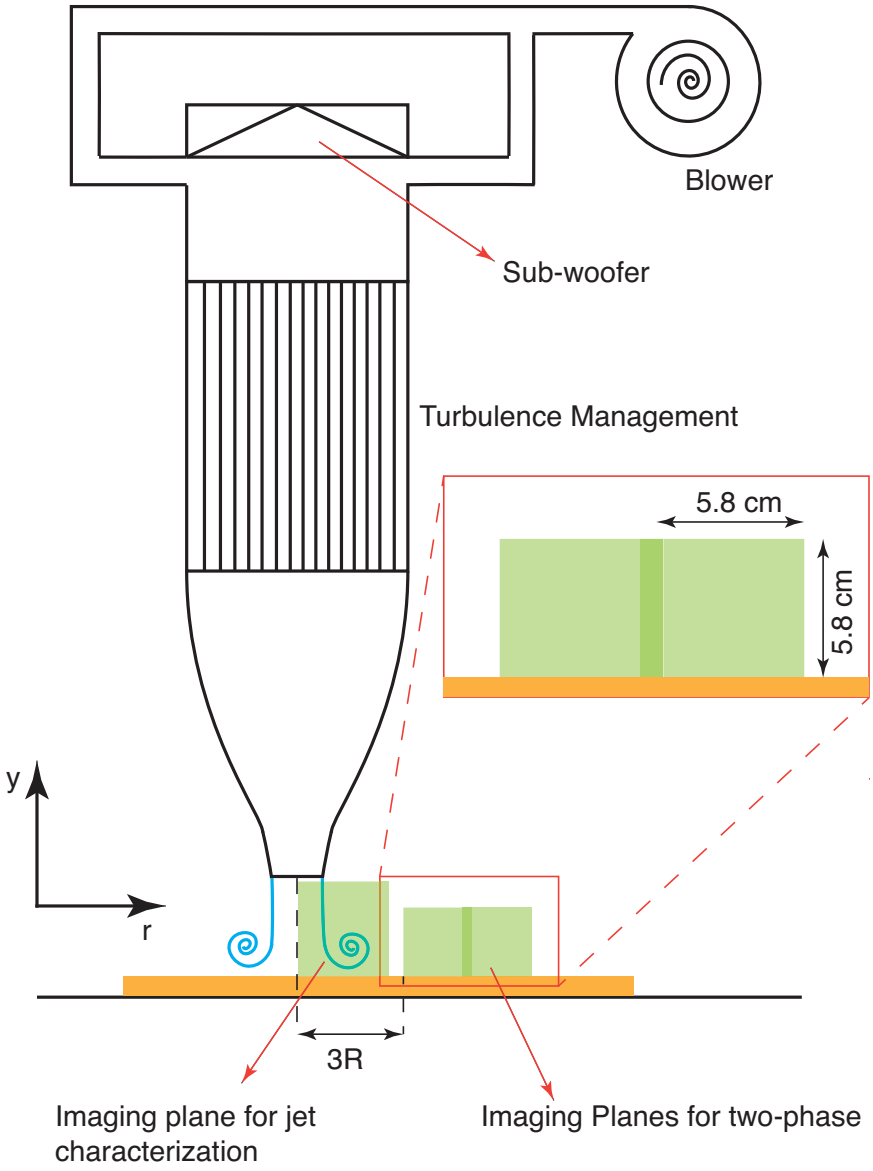

Figure 3.4: Experimental setup showing the imaging planes for acquisition of dual-phase PIV images

Table 3.2: Experimental settings for data acquisition

Aperture ($f\#$)	8
Light sheet thickness (mm)	1.5
Delay time ($\Delta t, \mu s$)	50
Field of view (cm^2)	5.8×5.8
Interrogation window size (pixels)	32×32 (with 50% overlap)

3.3 Data Processing

Conventional PIV has serious limitations when applied to study two-phase flows. Most of these problems and conventional ways to mitigate these problems have been outlined by Brücker [37]. These issues arise due to the fact that the suspended particles, even at moderate loads tend to cause light sheet attenuation and create blockage of line-of-sight of the imaging cameras.

3.3.1 Phase Separation

Phase separation is a technique that is employed to separate the fluid tracer signal and dispersed particles' signal in order to estimate velocities of individual phases. One of the main criteria of the separation is that there should be no significant contamination of individual signals or in other words the amount of "cross-talk" should be minimal. There are traditionally two methods that have been widely employed to perform phase separation in multi-phase PIV images.

1. Fluorescent or Optical Phase Separation

2. Intensity based Phase Separation

3.3.2 Fluorescent phase separation

Fluorescent or optical phase separation is based on wavelength of the scattered light from the two phases involved. The most common way to do this is by doping one of the two phases with a fluorescent dye that is excited at the wavelength of the light source used. Using a combination of filters and two cameras, each phase can be captured separately [38, 39]. Efforts have been made to mix Rhodamine 6G dye (excitation wavelength $\approx$ 532 nm) and Stilbene dye (excitation wavelength $\approx$ 355 nm) with potential organic solvents such as Ethylene Glycol, Ethanol and Bis-2-Ethyl Hexyl Sebacate (BEHS) that could be atomized into fine droplets forming the carrier phase. These solutions were atomized and the droplets were then examined using a zeta-sizer to check for the size distribution. The Ethanol solution could not be atomized because of its low viscosity. The other two solutions resulted in droplets that had non-uniform size distribution, which is not optimal for PIV measurements. As a last effort to make the fluorescent phase separation method work, a protocol has been found to fluorescently dope initially non-fluorescent dispersed phase (glass spheres). The method relies on making the glass particles porous by heating the glass to its phase transition temperature, which causes the boron compounds to aggregate. The boron-rich regions were then leached out using nitric acid, leaving a porous sphere, which could be impregnated with fluorescent dyes. The spheres were soaked in high concentration mixtures of either stilbene or rhodamine dissolved in either water or ethylene glycol. Unfortunately, once sufficiently dry for the glass spheres to become mobile, there was insufficient solvent left in the pores and only a weak fluorescent signal was produced.

3.3.3 Intensity based phase separation

While further refinements could have been probably be made (using solid oxide fluorescent salts, for example), a decision was made to adopt the intensity based technique using a single camera that has been used successfully with liquid/solid flows in the past. This method has restrictions, however, and requires more effort and care for reliable phase separation. Kiger and Pan (2000) [40] successfully demonstrated phase-separation by means of image processing using a two-dimensional median filter, which acts as a low pass filter. The resulting filtered image contains only the large dispersed phase particles and the tracer phase image can be obtained by subtracting the filtered image from the original image (Fig. 3.5). The resulting "holes" left behind after the subtraction process will result in erroneous vectors when they pass through the PIV cross-correlation process and hence need to be addressed carefully. Khalitov and Longmire (2002) [41] used second order intensity gradients and intensity saturation based criteria to identify all the particles in a composite two-phase image and separated the phase information based on size and brightness of all identified objects. These two methods have been adopted to implement phase separation in the present work and the detailed steps involved as well as some of the limitations of this technique and their impact on results will be discussed in later sections.

The imaging conditions have been optimized to satisfy two opposing criteria, a) the light sheet intensity has to be high enough to illuminate the small tracer particles (carrier phase) such that their signal is of sufficient strength to be recorded by the camera and b) the light sheet intensity has to be low enough such that the light scattered by large glass spheres (dispersed phase) and the bed surface do not saturate the camera sensor. These two cri-

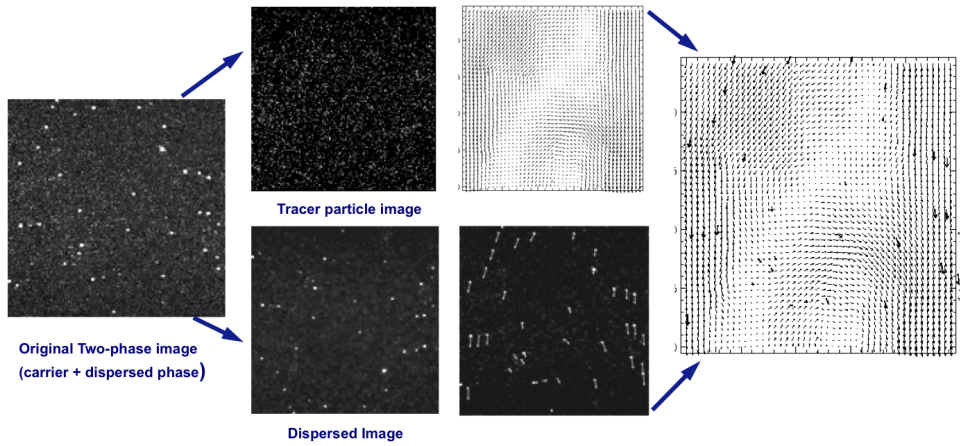

Figure 3.5: Phase separation and estimation of velocities of carrier and dispersed phases

teria have been met by finding the right combination of light sheet intensity, proper laser alignment and the lens' *f#* (See Table 3.2). The images are first pre-processed to minimize reflections from the sediment bed by employing a sliding minimum background subtraction. In order to improve the signal-to-noise ratio, a uniform minimum intensity threshold is applied. The CCD on the camera saturates at 10000 counts while the noise floor under current illumination conditions is approximately 20 counts. A minimum threshold of 25 counts is employed to filter this sensor noise. A two-dimensional 3×3 median filter is applied on these images [40] and the resulting image is subtracted from the original image to generate the carrier phase (tracers only) image. The dispersed phase is then identified by first constructing an object identification mask. A binary template is produced by following the method developed by Khalitov and Longmire [41] that employs two-dimensional intensity gradients along with saturation threshold criteria to identify the location of particle images:

$$\frac{\partial^2(\ln I_p)}{\partial x^2} < 0 \qquad \text{or} \qquad I_p > I_{sat} \qquad \text{where} \tag{17}$$

I_p is the pixel intensity and I_{sat} is the saturation criteria. This object detection algorithm is very sensitive to high-frequency noise because it uses second order spatial derivatives. The derivatives amplify the noise, resulting in identification of many erroneous objects. To avoid this erroneous object detection, a low-pass spatial filter (Gaussian smoothing) is applied to each image prior to computation of derivatives. The mask is constructed by applying the Gaussian smoothing function with pixel radius of 1.25 pix to the median filtered image to smooth the edges of the large and bright dispersed phase object images. The smoothing function used is given by

$$k = \exp \frac{-(x^2 + y^2)}{2r} \qquad \text{where} \tag{18}$$

k is the smoothed value, and x and y are the local neighboring data points for the data to be smoothed. The controlling parameter in the above equation is the smoothing radius r, which is varied based on the image quality and particle density. Artificial images were used to conduct a parametric study on the effect of r on identifying the objects. A multi-step smoothing operation with 2 passes with an r value of 1.25 was found to be optimum in 3 cases with different particle sizes and similar distribution. This resulted in an increase of 3-4% in the total number of particles identified (Fig. 3.6).

Once all the objects in the original image are identified, the size and brightness of each identified object is used as discriminating criteria to identify dispersed phase objects. With this information, a dispersed phase-only image is generated and the intensity values from the original image are then copied onto these identified locations (Fig. 3.7). Sample images with carrier-phase only and dispersed-phase only have been used to identify reliable separation criteria for the current imaging conditions to minimize cross-talk and maximize

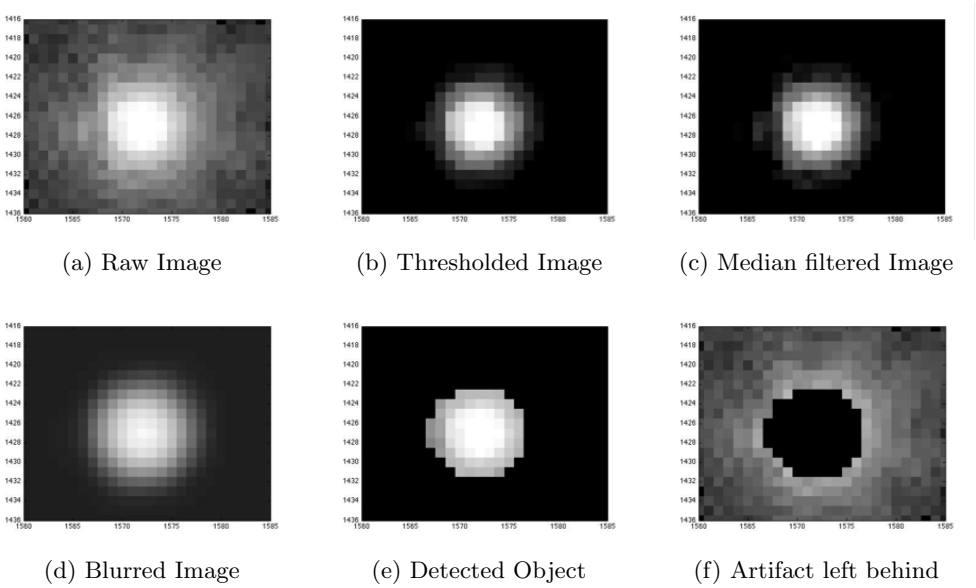

(a) Raw Image (b) Thresholded Image (c) Median filtered Image

(d) Blurred Image (e) Detected Object (f) Artifact left behind

Figure 3.6: Processing steps used to identify dispersed phase image from a composite dual-phase image

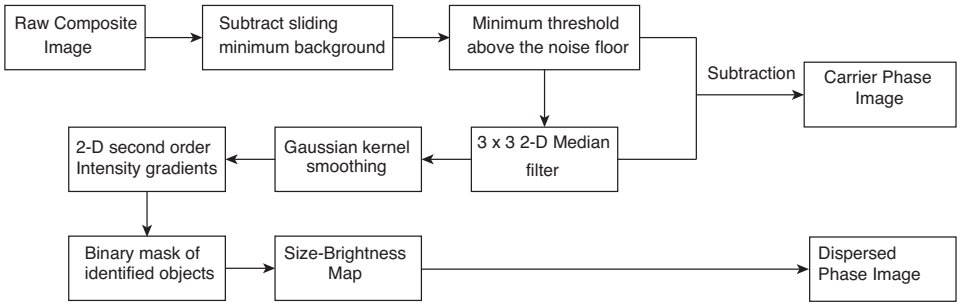

Figure 3.7: Phase separation algorithm

the number of correctly identified dispersed phase particles (Fig. 3.8). The tracers are generated from an atomized spray of Bis-2-Ethyl-Hexyl Sebacate (BEHS) with a droplet size of about 1-2 μm.

However, not all identified particles are suitable for accurate velocity measurements. In regions of high particle loading, especially very close to the bed, it is not possible to discriminate individual particles and hence cannot be used to estimate concentration or velocities. Particles that are on the edge of the measurement volume appear as large, dim and out of focused and hence

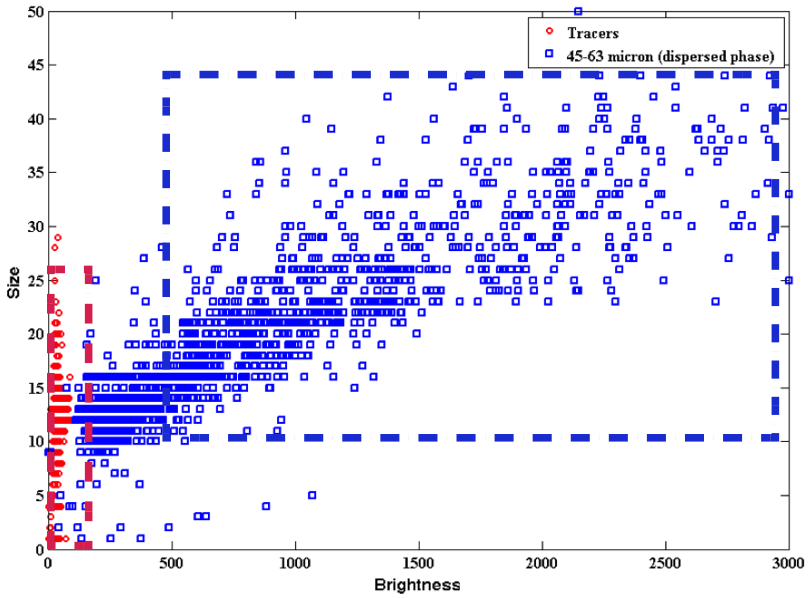

Figure 3.8: Size-brightness map of dispersed phase particle images and tracer particle images. The two non-overlapping regions shown in red and blue correspond the size-brightness thresholds used to separate the carrier phase and dispersed phase images respectively

not ideal for accurate velocity measurements. (Fig. 3.9 and Fig. 3.10). Using a size criteria of $25 < A_p < 100$ pixels, as well as an average brightness criteria of B >500 counts gave a cross-talk error of 2%, while correctly identifying 95% of the dispersed phase particles. The distance between the measurement plane and the camera sensor plane for the two-phase experiments is 0.5 m. Given the short distance, the blockage effect due to suspended particles is minimal.

3.3.4 Vector calculation and super-resolution PIV

The carrier-phase images are then used to extract the fluid velocity field by performing standard cross-correlation using LaVision's Davis software (version 8.0.5). A multi-pass routine with an interrogation window size of 32×32 pixels with 50% overlap in the final pass has been used. The particle flow field is

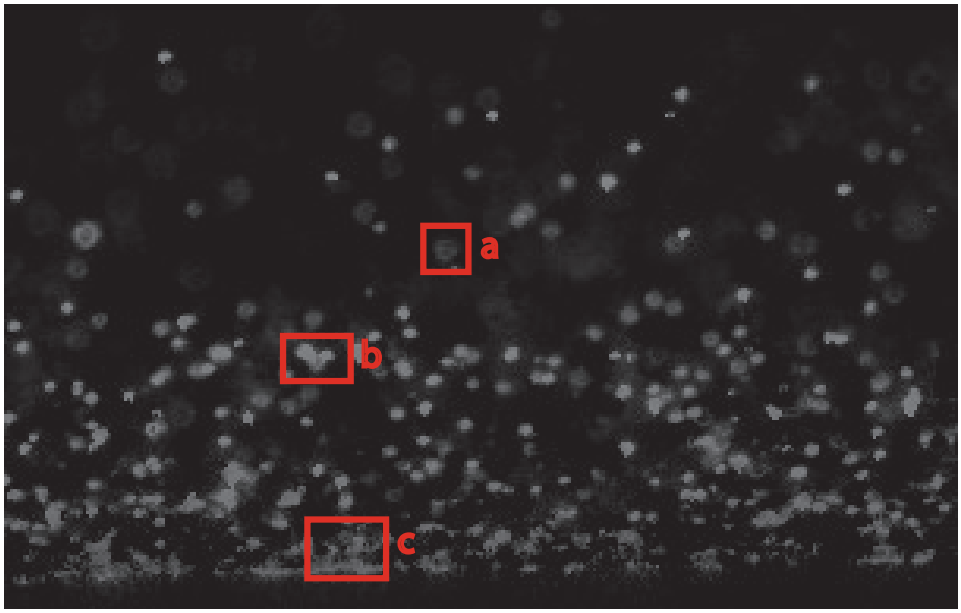

Figure 3.9: Discarded objects within the two-phase image a) Dim and out of focus particles b) Large clumps of multiple particles identified as a single particle c) Plumes of suspended particles very close to the bed

characterized by high particle volume fraction near the bed surface and the flow becomes dilute as one moves away from the surface. It is also characterized by high velocity gradients and hence standard particle tracking algorithms fail to capture these important details. In order to estimate the velocity field of the dispersed phase, a super-resolution or hybrid PIV/PTV algorithm has been implemented [42] to improve the performance in high particle concentration regions, while still retaining the flexibility inherent to PTV to resolve multi-valued velocity displacements within a given interrogation window (Fig. 3.11).

A coarse PIV pass is carried out on the dispersed phase images when the number of particle images in an interrogation window (64×64 pixels) is higher than a nominal threshold value to ensure that the cross-correlation information obtained is reliable (at least 5 particles in a single interrogation window). If the particle image concentration is too low, this step is skipped and the displacement estimate at this window location is set to zero. The second

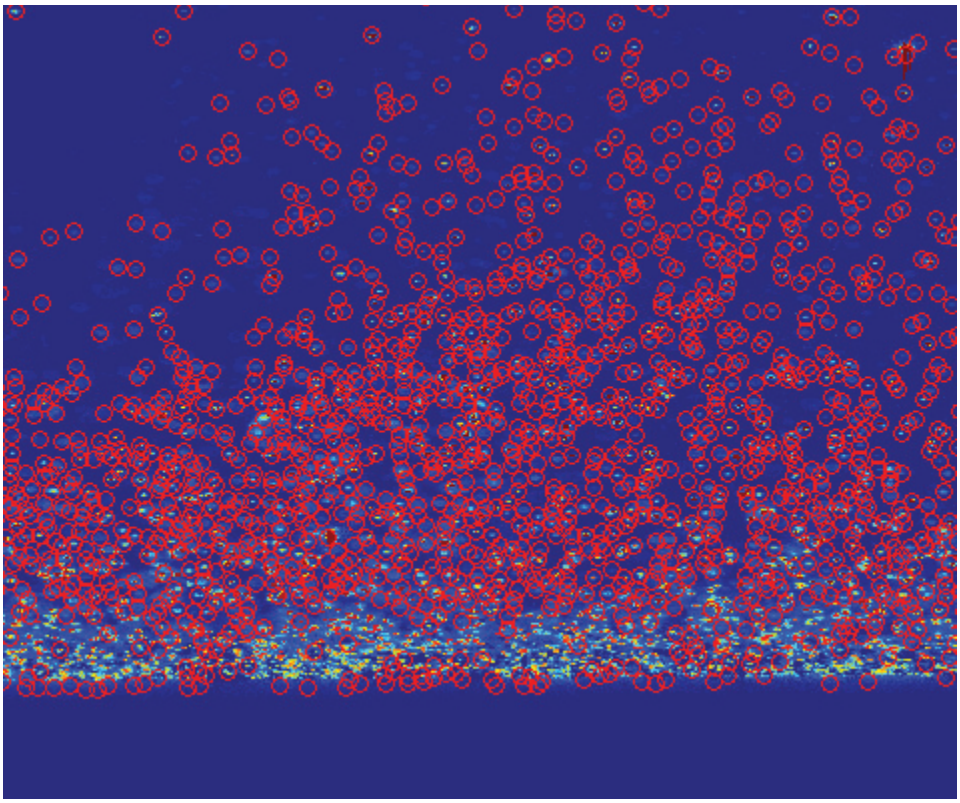

Figure 3.10: Image showing particles actually identified by the algorithm over the raw-image. The high concentration region near the bed is rejected due to the fact that particle images overlap and cause significant bias in particle identification

image sub-window is shifted by this displacement in the appropriate direction and the cross-correlation analysis is performed again. This process is repeated until the nearest integer value of the displacement goes to zero. If the value does not converge in three passes, the displacement estimate at that window is set to zero [43]. At the end of each PIV pass, spurious vectors are identified using a universal outlier detection median test as outlined by Westerweel and Scarano (2005) [44]. In the subsequent PTV step, particles in the first image are paired with particles in the second image and the position of particle in the second image is estimated using the mean interpolated displacement (dx) obtained from the PIV pass. A 12×12 sub-window (I) is centered on each particle location and a correlation analysis is done to estimate the final displacement

of the particle. In locations with no displacement estimate from PIV, a search window of size 16×16 pixels (I) is used to maximize the detection probability of a matching particle (maximum particle displacements were found to be 5 pixels with the delay time of $50\mu s$). Synthetic images with uniform displacement (Fig. 3.12) show the vast improvement of hybrid algorithm over standard PTV, especially at high concentrations.

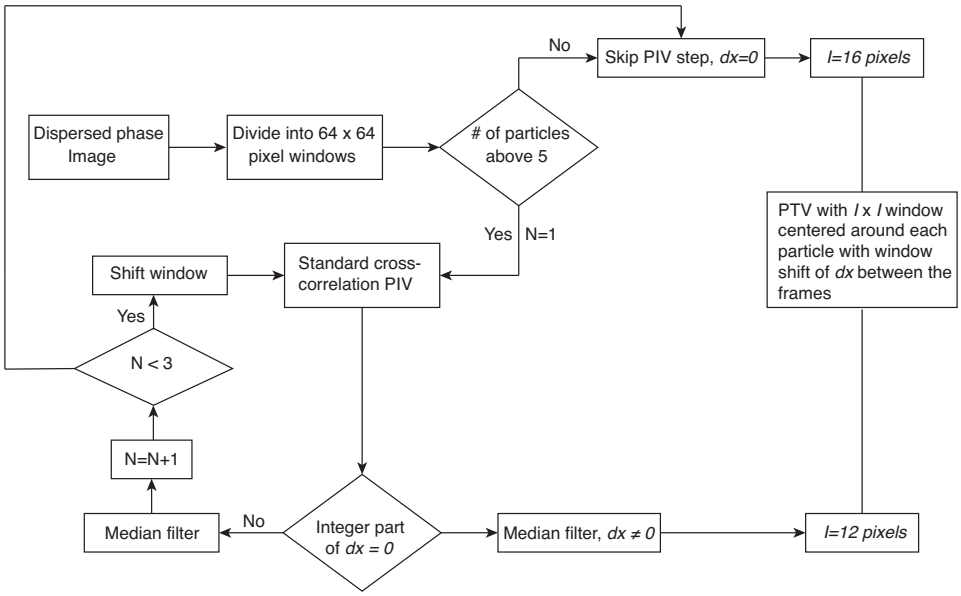

Figure 3.11: Super-resolution PIV/PTV algorithm

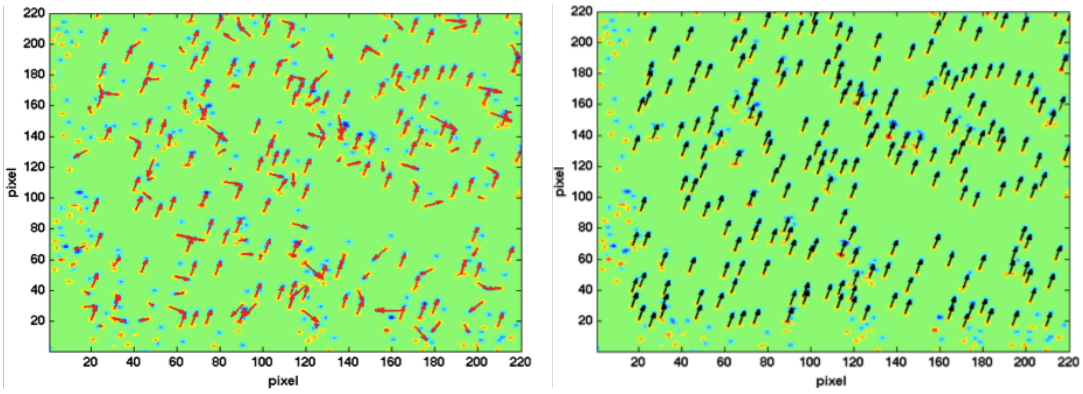

(a) Standard PTV (b) Hybrid PIV/PTV

Figure 3.12: Standard PTV and hybrid PIV/PTV showing improvement in uniform displacement case with high particle concentration

3.3.5 Validation with artificial data

Synthetic images have also been used to evaluate and optimize the performance of phase separation as well as hybrid PIV/PTV algorithm with a parametric space that included particle image density (N_A-fraction of total area occupied by particles), Stokes number, delay time and the sizes of interrogation windows. To capture essential features of this flow field, especially in regions with large velocity gradients and regions where particle paths cross each other, a Taylor-Green vortex flow has been used to generate artificial images. The fluid velocity at location *(x,y)* is given by

$$U_f = U_o \sin\left(\frac{2\pi x}{\lambda}\right)\cos\left(\frac{2\pi y}{\lambda}\right) \quad \text{where} \quad \frac{\lambda}{U_o} = 81.3 \text{ time units} \tag{19}$$

The image size is 512×512 pixels and the time-period for a fluid element to complete an orbit is about 12 time-steps. The particle equation of motion for this flow field is given by

$$\frac{du}{dt} = \frac{\sin x \cos y - u}{St} + \phi \sin x \cos x + \frac{1}{2}\phi(u \cos x \cos y - v \sin x \sin y) \tag{20}$$

$$\frac{dv}{dt} = \frac{-\sin x \cos y - v}{St} + \phi \sin y \cos y + \frac{1}{2}\phi(u \sin x \cos y - v \cos x \cos y) \tag{21}$$

$$\frac{dx}{dt} = u \quad \text{and} \quad \frac{dy}{dt} = v \tag{22}$$

where St is the particle Stokes number and ϕ is the density ratio of the fluid and the particles. The parametric space for this study included variation of particle Stokes number, particle image area ratios and the delay time between the frames. It should be noted that the particle image size remains constant at 1 pixel (radius) and that there is no artificial background noise for all the cases (Fig. 3.13).

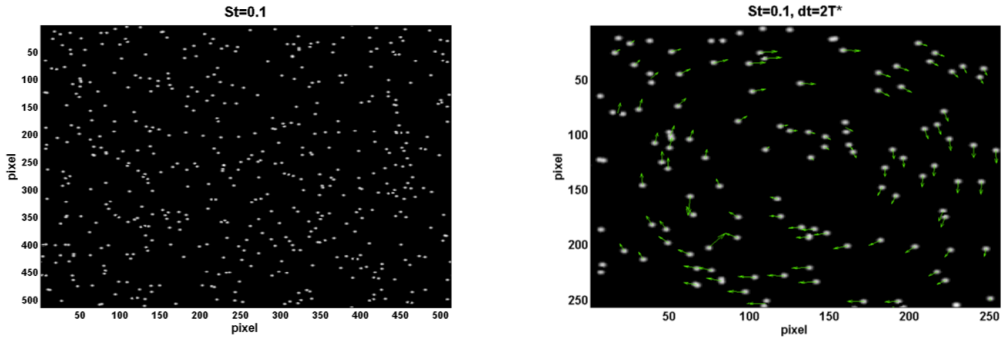

(a) Synthetic Image

(b) Vector Field obtained by the hybrid algorithm

Figure 3.13: Synthetic image showing identified particle locations and particle velocities at $St = 0.1$ and a maximum displacement of $dx = 6$ pixels

Particle identification effectiveness is close to 100% for low particle image densities ($N_A = 0.001$) and it decreased to 85% when the image density increased ten fold ($N_A = 0.01$), in large extent due to particle image overlapping. Most of the snapshots from actual experiments fall between these two extremes. Results indicate that the performance of hybrid algorithm is enhanced at higher particle image densities. For Stokes number of 0.1 and constant delay time, about 6% of calculated displacements were deemed spurious based on a deviation of more than 5% in magnitude from true displacement for moderate to high particle image densities. A maximum efficiency improvement of about 20% is seen at high particle image densities in estimating particle displacements, when compared to standard PTV for this case. However, performance efficiency decreases with increasing delay time and increasing Stokes number for all particle image densities.

4 Calibration of measurement volume

Determination of the effective measurement volume is essential for making quantitative concentration measurements of a dispersed phase when using particle-imaging technique for two-phase flows. Transport equations for both mass and momentum require accurate estimation of particle volume fraction along with particle velocities. The effective measurement volume (Fig. 4.1), while nominally determined by the local light sheet thickness, the actual value depends also on the dispersed phase identification characteristics used to detect the particles (relative brightness, size, etc.), and stray illumination such as scattering by tracer particles and wall reflections, necessitating use of local calibration techniques. A novel method is being investigated where the effective light sheet thickness is estimated using particle image correlation information of free falling dispersed-phase particles settling through a tilted light sheet along with size and brightness criteria of dispersed phase images.

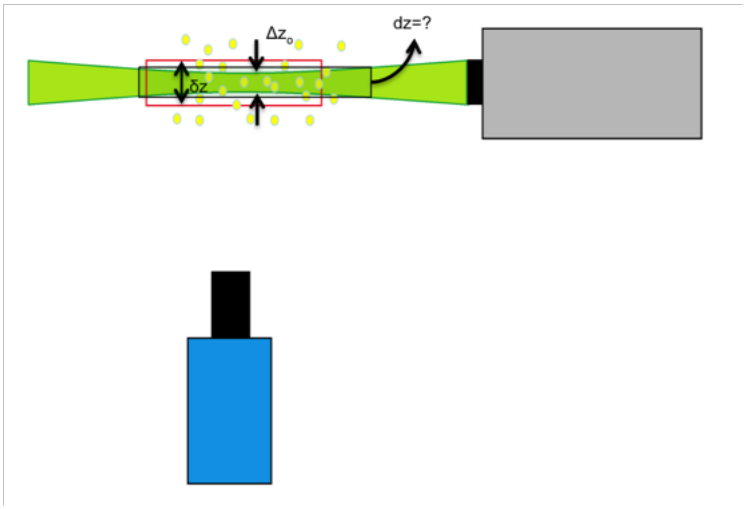

Figure 4.1: Schematic of typical PIV setup

Calibration of thickness of measurement volume has been done earlier in liquid-solid flows by Kiger and Knowles (2010) [45], where they used

threshold criteria based size and brightness of particle images to determine the proximity of the particles to the center of the light sheet. They embedded sediment particles at known concentrations in a refractive index matched hydro-polymer gel and traversed this "suspension" through the laser light sheet by fixed increments as shown in Fig. 4.2. The size and brightness of the particle images were then analyzed and thresholds were imposed to determine the thickness of measurement volume.

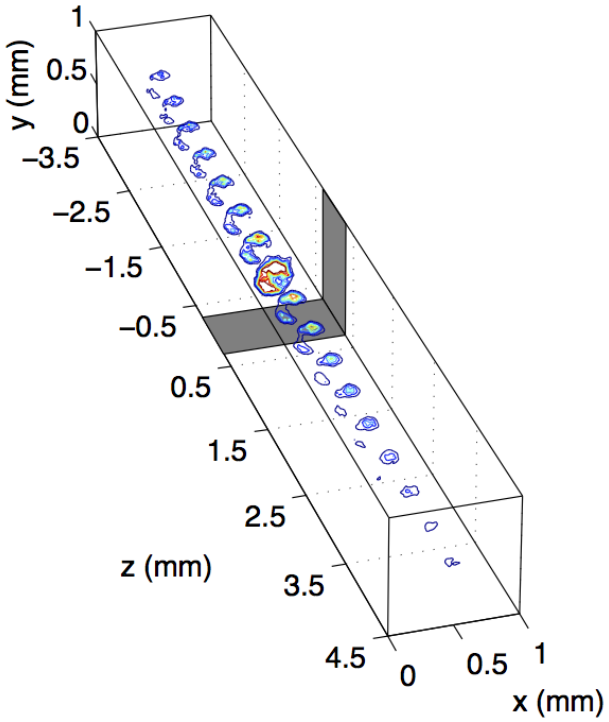

Figure 4.2: Iso-contours of particle brightness vs relative location for a typical single particle. Nominal light sheet position and $1/e$ thickness denoted by the grey band [45]

4.1 Tilted light sheet test for high speed PIV systems

Moving glass particles through air by fixed distances is tricky and hence a different approach is needed to estimate measurement volume for two-phase

PIV measurements in air. Tests have been conducted using a high-speed PIV imaging system working at 3000 Hz. The light sheet is tilted with respect to vertical and the camera is aligned perpendicular to the light sheet as shown in Fig. 4.3. Glass particles of 50 μm nominal diameter are dropped into the test section from a height of about 1m, so that they enter the test section moving at terminal velocity. So instead of having fixed displacement, a fixed velocity is chosen and the motion of these moving particles can be "frozen" using the high-speed camera. In order to prevent external air currents influencing the particle motion, a cylindrical PVC pipe is used to shield the falling particles. The terminal velocity of these particles is estimated to be about 1.84 m/s. The estimated depth of focus is 1.2 mm (105 mm lens, $f/4$) and the field of view is 8 cm^2. The light sheet thickness in the field of view is 1 mm (86.7%) as shown in Fig. 4.3

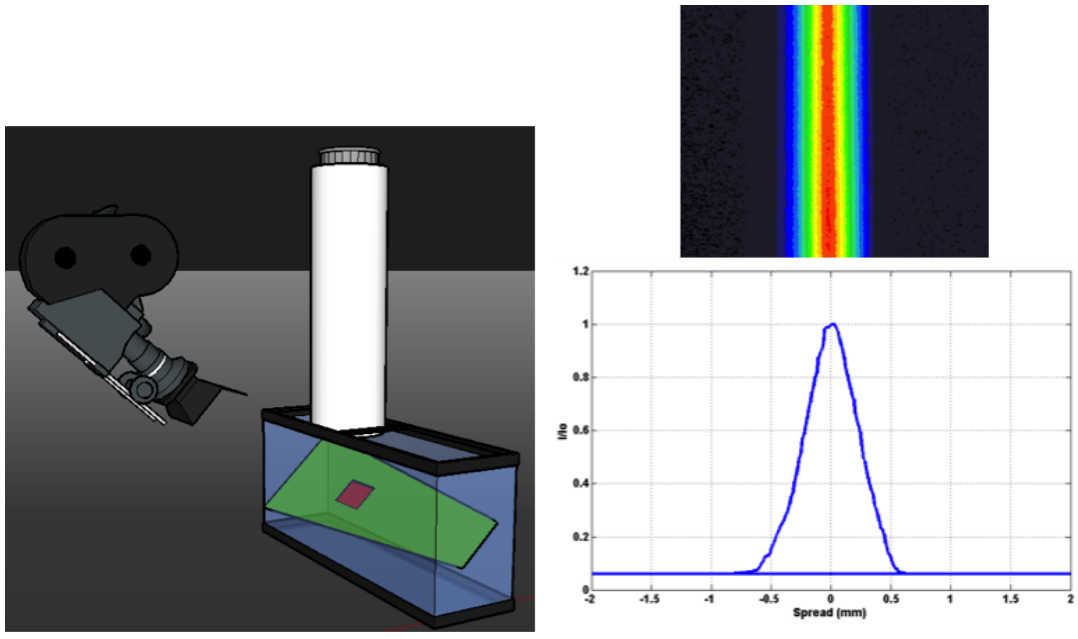

(a) (b)

Figure 4.3: (a) Schematic of test setup (b) Light sheet thickness estimated by a beam profile camera

These particles are imaged using a high-speed camera as they fall

through the light sheet as shown in the illustration. As particles move through the light sheet, their scattering characteristics and hence their size and brightness varies. Shown in Fig. 4.4 is the average peak brightness and size of several particle streaks. When the consecutive images are averaged, the particle paths appear as streaks in the average image. The average brightness and size are estimated from 35 such particle streaks from the ensemble, starting from the first instance when the particle enters the light sheet until the point where it leaves the light sheet. It is evident that the average brightness increases dramatically as the particles enter the measurement volume and the average size has a more gradual increase. It can be inferred that a particle image that has its peak brightness value above $0.05I_o$ (where I_o is the saturation limit for the camera) is within the effective measurement volume, which in this case turns out to be 2 mm.

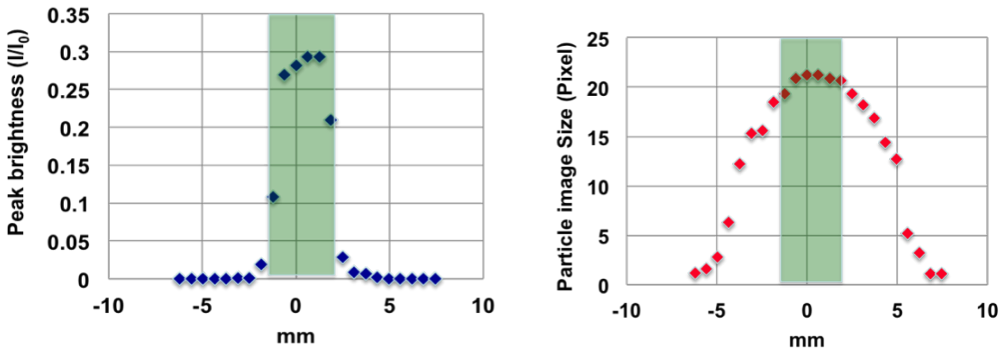

(a) (b)

Figure 4.4: Variation of particle image (a) brightness (b) size, as they fall through the tilted light sheet

4.2 Calibration volume for Phase-resolved systems

For a phase resolved low-speed PIV system, it is not possible to track size and brightness of individual particles as they pass through the light sheet. In

that case, a PTV correlation based criteria has been implemented that relies on decay of the correlation peak height with increasing delay time to identify the effective measurement volume. Fig. 4.5 is the ensemble average correlation peak height of all identified particles from 5000 images as a function of delay time. It is evident that the peak height drops due to out of plane motion of the particles with increasing delay time. When these peaks are normalized with the maximum peak height from the lowest delay time, we can look into the decay trend as shown in Fig. 4.5. The peak height drops off dramatically until $3\Delta T$ and remains flat as the delay time is further increased. This indicates that these particles take a time of $3\Delta T$ to traverse through the measurement volume and knowing the terminal velocity of these particles a priori, the effective light sheet thickness can be backed out, which turns out to be 1.85 mm. This is a proof of concept study and needs to be implemented for current work.

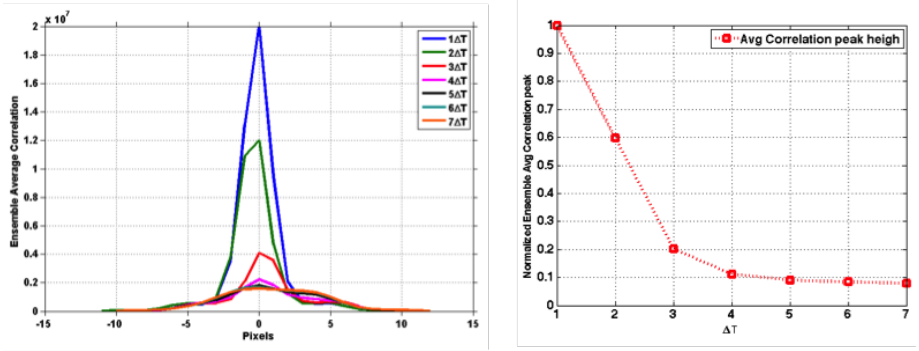

Figure 4.5: a) Average correlation peak height as a function of delay time and b) Normalized correlation peak height as a function of delay time

Both the methods outlined here need to be extended to take into account the varying light sheet thickness across the domain as well as scattering characteristics from tracers and bed surface, if any. In the end, the brightness based criteria has been adopted to determine the measurement volume of the current set of experiments. A brightness lower limit of 500 counts (with the saturation criteria of the camera sensor at 10000 counts) has been chosen to

give a uniform measurement volume thickness of 2 mm.

5 Results and Discussion

5.1 Characterization of the forced jet

The forcing of the speaker produces a pressure pulse that travels through the tunnel and causes the roll-up of the free-shear layer emanating from the edge of the nozzle, resulting in the formation of a vortex ring. Single-phase PIV has been employed to study the vortex formation, trajectory and it's subsequent interaction with the ground. An imaging plane directly under the edge of the nozzle, as shown in Fig. 3.4, is chosen to investigate the trajectory and circulation strength of the vortex ring. Phase-locked realizations are captured at a particular phase angle in the forcing cycle. Ensemble averages of 100 image pairs per phase angle of the forcing cycle were used to calculate the mean statistics.

In order to understand the results from the experiments, the symbols and notations of the quantities involved must be lucid. In this case, any physical quantity α can be split into a phase-averaged and a stochastic component.

$$\begin{aligned} \alpha &= \widehat{\alpha} + \alpha' \quad \text{where} \\ \widehat{\alpha} &= \frac{1}{N_s}\sum_{i=1}^{N_s} \alpha_i \quad \text{where} \end{aligned} \tag{23}$$

N_s is the total number of realizations in the ensemble acquired at that particular phase angle and $\widehat{\alpha}$ is the phase average that includes time average as well as the periodic component and α' is the stochastic component. An ensemble average of all the realizations from all phase angles can be calculated

to estimate the time average of the quantity, represented as $\bar{\alpha}$.

$$\overline{\alpha} = \frac{1}{\Psi} \sum_{1}^{\Psi} \widehat{\alpha} \quad \text{where} \tag{24}$$

Ψ is the total number of phase angles used to capture phase-locked samples. Subscripts are used wherever necessary. The subscripts p and f correspond to the particulate phase and the carrier phase respectively. The second set of subscripts r and y correspond to the orthogonal radial and wall-normal directions.

The operating conditions have been tuned to match the circulation strength of the micro-rotor from Sydney et al. (2011) [34], which was found to be 0.12 m^2/s. Shown in Fig. 5.1 are the single-phase fluid streamlines superimposed over vorticity contours. As the vortex ring approaches the ground, it accelerates the boundary layer causing an adverse pressure gradient. This results in the separation of the boundary layer, leading to the formation of a secondary counter-rotating vortex ring. The primary and the secondary rings interact three-dimensionally and undergo dissipation further downstream. This three-dimensionalization results not only in dissipation, but also increases the stochastic signature due to the non-linear interactions. The time-averaged flow field has the characteristics of a wall jet with a signature of embedded vorticity as shown in Fig. 5.2.

In the overlapping downstream planes, there is "jitter" in the location and strength of the primary vortex as it interacts with the ground and dissipates, as well as due to the averaging process itself. As a result, the primary vortex becomes sufficiently incoherent that triggering off of the original forcing signal no longer has much relevance to the location of the flow structure. Geiser and Kiger (2011) [36] presented more details on this aperiodic vortex

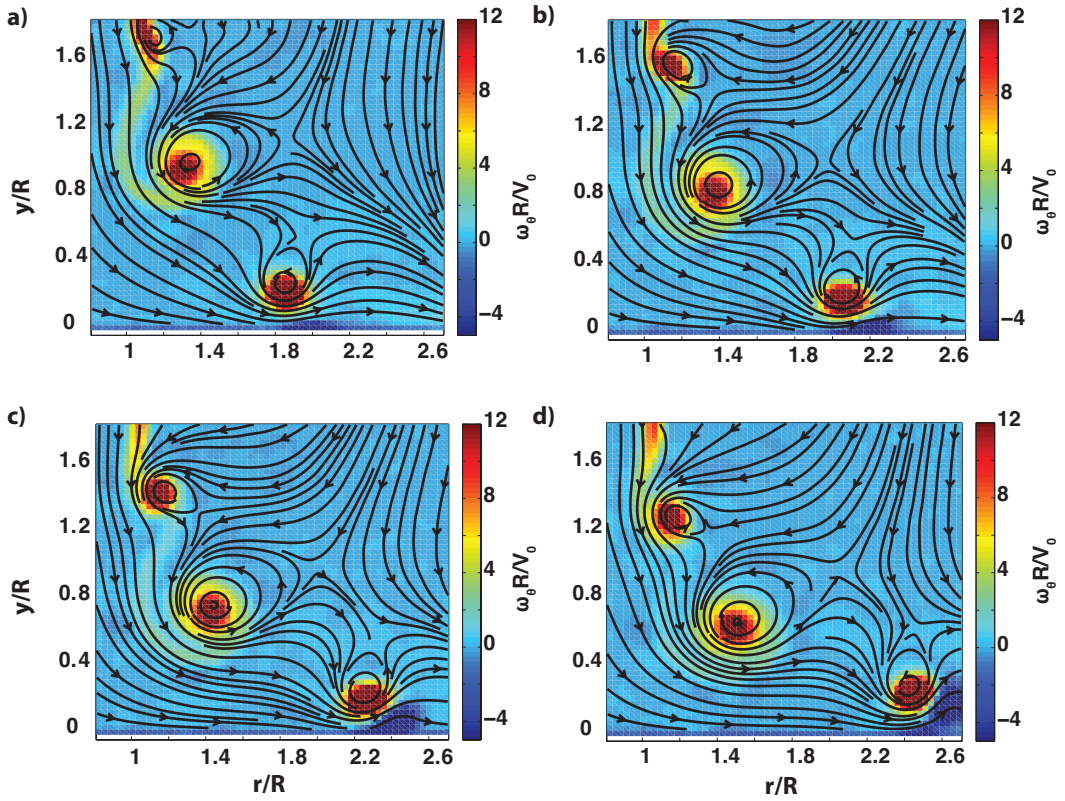

Figure 5.1: Single phase fluid velocity streamlines with normalized vorticity ($\omega_\theta R/V_o$) showing vortex ring generation and it's interaction with the ground at a) $t/T = 0.5$, b) $t/T = 0.58$ c) $t/T = 0.67$ and d) $t/T = 0.75$

behavior during its interaction with the ground plane. Nonetheless, some averaged structure is still visible, and hence is presented in the form of ensemble averaged fluid velocity fields Fig. 5.3. There is still a slight signature of the negative counter rotating vortex as the the primary vortex bounces along the surface.

Fig. 5.4 shows single phase time averaged radial fluid velocity profiles as a function of radial distance and it is evident that the fluid decelerates as one moves radially outward.

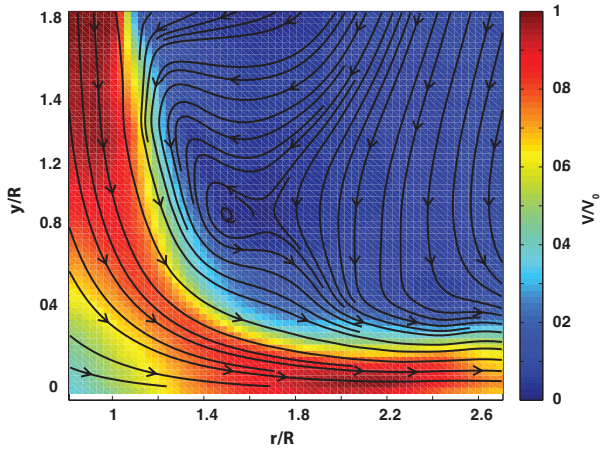

Figure 5.2: Single phase time averaged fluid velocity magnitude with streamlines

5.2 Two-phase measurements

Phase-resolved multiphase PIV measurements have been made in the downstream location as illustrated in Fig. 3.4. One of the recurring issues with the current two-phase experiments has been repeatability of particle behavior. The moisture content of the particles as well as that of the surrounding environment and ambient temperature had significant effect on the suspension process. It is difficult to keep these parameters same for all experiments but a protocol has been developed to minimize the impact of these external factors. The particles are sifted thoroughly before each experiment and then heated in a glass beaker inside a microwave oven with a dryer sheet in place. This removes the moisture as well as any electrostatic charge on the particles. Particles that have been used more than thrice are discarded and replaced with a new batch of particles. The experiments have been planned such that the data is taken on similar days during summer when the weather was relatively dry.

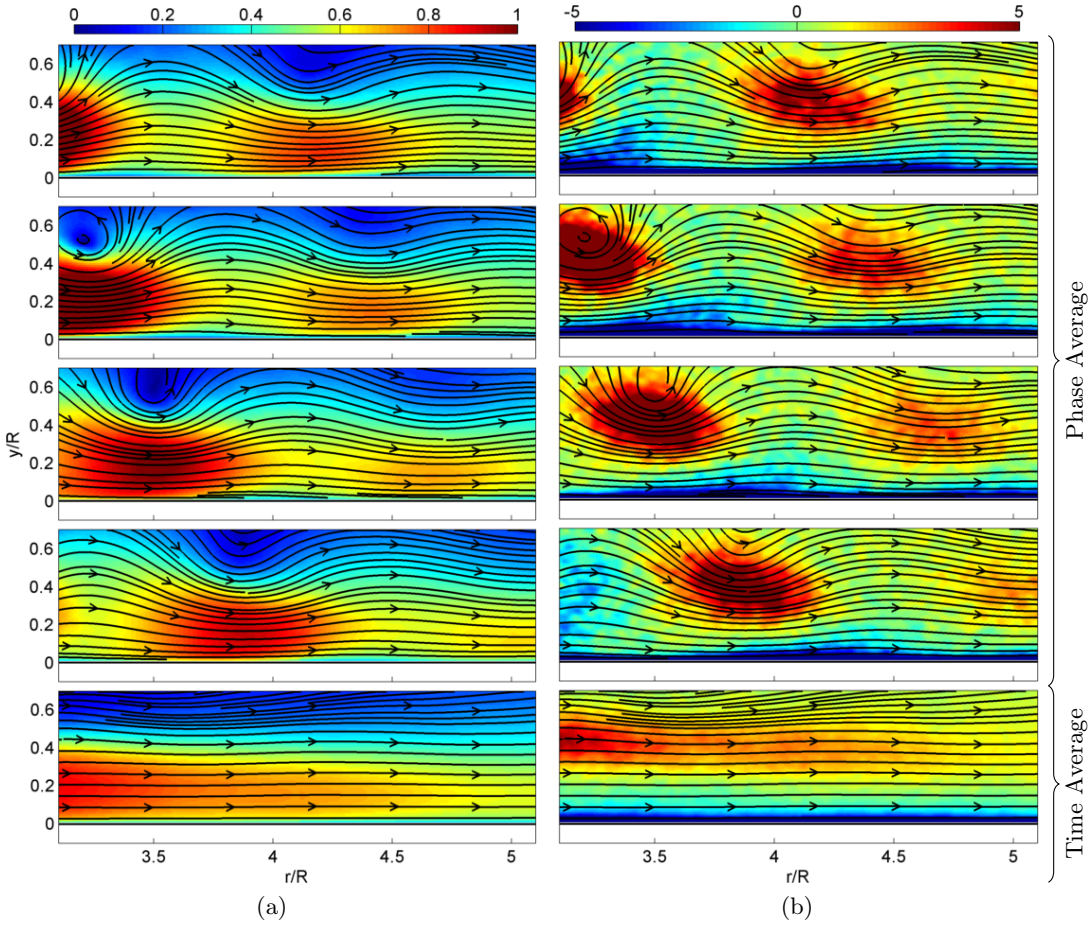

Figure 5.3: (a) Single-phase fluid velocity magnitude, u_f/V_o with fluid streamlines (b) Single-phase vorticity contours $\omega_\theta R/V_o$ with fluid streamlines. The four phase averages are calculated at $t/T = 0.25, t/T = 0.5, t/T = 0.75$ and $t/T = 1.0$

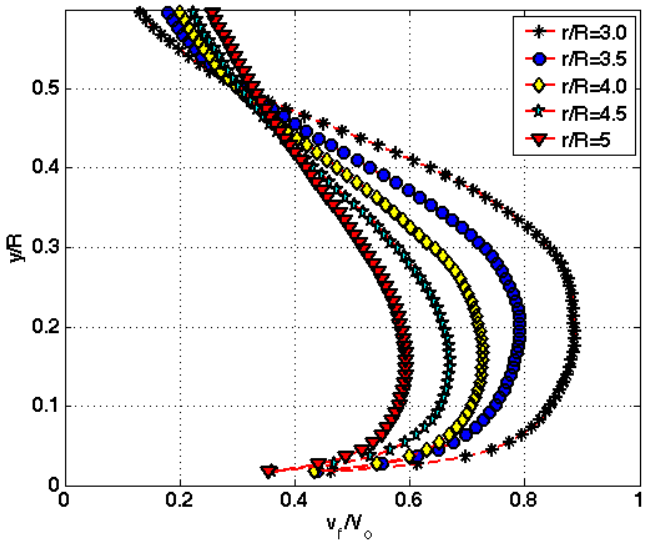

Figure 5.4: Single-phase time averaged radial fluid velocity profiles (u_{fr}/V_o) as a function of radial distance showing fluid deceleration

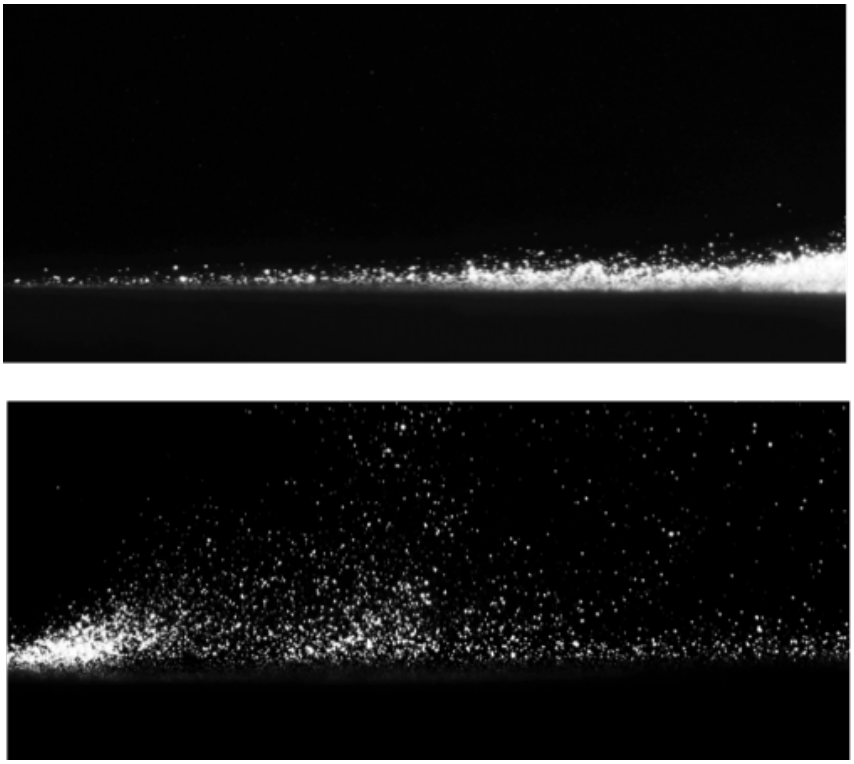

Figure 5.5: Suspension pattern at a) $t = 0$ and b) $t = 1s$

The sediment bed beneath the jet is initially nominally flat. When the bed surface evolves over time due to erosion, one can observe the formation of undulations or scour holes on the bed surface. It has been observed that the suspension process is highly intermittent and is very sensitive to local transient bed conditions. Fig. 5.5 shows a raw two-phase image at time $t = 0$ when the bed is completely flat. The suspended particles are very close to the bed and they appear to be moving predominantly in the radial direction. In the snapshot at $t = 1s$ (after the passage of approximately 50 primary vortex rings) and the flow features are completely different. As the bed erodes it starts forming transient topological features in both the radial and azimuthal directions on the surface that affect vortex interaction with the bed. In order to understand the effect of bed-form topology on sediment suspension, two cases have been studied:

1. **Flat bed case:** The samples are recorded after 100 vortex impacts on the sediment bed. It should be noted that the bed is not completely flat at this point and it is assumed that small amplitude and long wavelength of initial bed deformities did not adversely affect the dynamics of the interaction. 35 image pairs are recorded at a frequency of 6 Hz and the bed is scraped flat after each set has been acquired. This is an evolving flow and hence the bed topology changes if the acquisition time is longer than a few seconds. The specific limitation of 35 image pairs per set is imposed by the limited on-board memory of the cameras. The data transfer rate from the cameras to the local hard drive is not fast enough to clear the memory buffer on the fly without compromising the recording frequency. 16 such sets of 35 image pairs are acquired to form an ensemble of 560 image pairs for each phase angle, for a total of 8 phase angles.

2. **Eroded bed case:** The bed is allowed to evolve and images are recorded

after 4000 vortex impacts. The bed is not flat anymore and there are deep ripples formed on the surface due to erosion. Similar to the flat bed case, 35 image pairs are acquired for each set and 16 such sets form an ensemble of 560 image pairs per phase angle, for a total of 4 phase angles. After each set of 35 images has been acquired, the bed is scraped flat again and allowed to evolve before recording the next set. The eroded bed profile is shown in Fig. 5.6. The profiles were measured with the jet turned off to prevent suspended load from contaminating the bed elevation measurement. Scattering from the bed produced a bright band where the light sheet intersected the bed. The static images were smoothed with a Gaussian filter in the vertical direction, and the peak scattering intensity was used to mark the nominal bed height. A primary ripple with a depth of about 3 mm forms near the point of impingement of the primary vortex and a secondary ripple with a depth of 1.5 mm forms downstream. Fig. 5.7 shows the eroded bed profile in the measurement domain used for quantifying two-phase flow. From the profile, one can see the formation of a scour hole close to the point of impingement at $r/R = 2.3$. All the two-phase measurements are done at the location of the secondary ripple since the particles mobilized upstream are scouring and saltating along the bed surface and do not enter suspension until $r/R \approx 3.0$. The particles entrained into the flow are then pushed further out by the mean flow even after vortex dissipation. Hence the bed height does not go above the initial bed height unlike the erosion profiles shown by Munro et al (2009) [30] where there is no mean flow. These profiles are consistent with their work using small particles where they see no deposition of suspended particles downstream on the vortex. In the eroded bed case, the particle concentration near the bed ($y/R < 0.1$) is much higher compared to the flat bed case. Phase separation and particle identification is impossible

in this region without introducing a significant bias and hence has been excluded from the calculations.

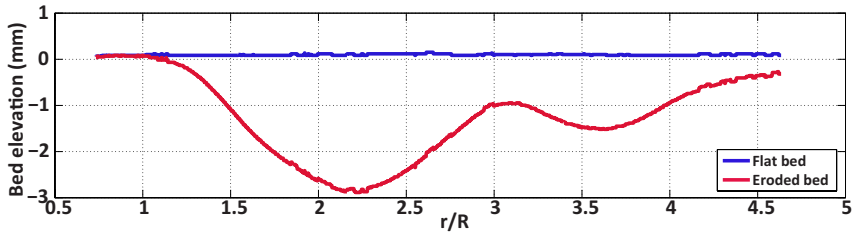

Figure 5.6: Erosion profile of the sediment bed 100 vortex impacts and after 4000 vortex impacts

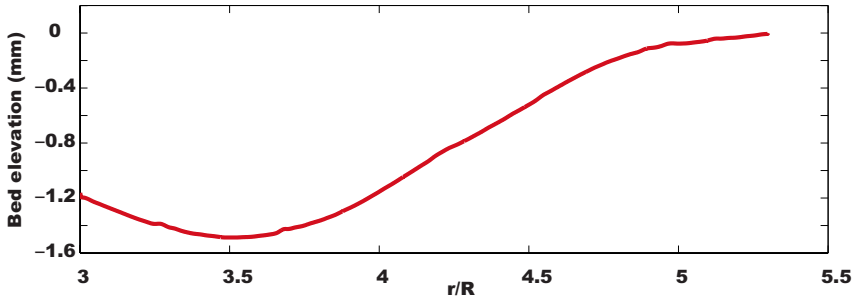

Figure 5.7: Erosion profile of the sediment bed after 4000 vortex impacts in two-phase measurement domain

These two cases are then compared against each other as well as with the single phase flow.

The diameter of the vortex core is based on the area occupied by vorticity greater than the threshold vorticity.

$$D_v = \sqrt{\frac{2A_v}{\pi}} \quad \text{where} \tag{25}$$

A_v is the area occupied by vorticity greater than 10% of the maximum vorticity at the centroid of the vortex core, which gives an effective core diameter of $1.0cm$ just prior the point of primary impingement. The Stokes number associated with the current flow conditions is estimated using the particle relaxation time, τ_p and a characteristic fluid time scale, τ_f. The fluid time scale

is based on the diameter of the vortex core before it interacts with the ground and the peak-to-peak velocity across the vortex.

$$\tau_p = \frac{\rho_p}{\rho_f} \frac{d_p^2}{18\nu} \tag{26}$$

$$\tau_f = \frac{D_v}{V_{pk-pk}} \tag{27}$$

$$St = \frac{\tau_p}{\tau_f} \approx 15 \tag{28}$$

The Stokes number in this case is estimated to be ≈ 15.

Fig. 5.8 and Fig. 5.9 depict the instantaneous realizations showing vorticity contours with fluid streamlines and identified particles from the phase-separation routine for the flat and eroded bed cases respectively at $t/T = 0.5$. Observing the qualitative features of suspension in the flat bed case, it is evident that the coherence of the vortex and its proximity to the bed has a big impact on suspension process. The suspended layer of particles is thin and relatively uniform. When the vortex is coherent but away from the bed, usually less number of particles are in suspension. If it is coherent and close to the bed, suspended particles seem to get entrained by the vortex but the number of particles is not necessarily very high. The suspended load seems to highest when the vortex has decayed and its remnants are scattered around $y/R \approx 0.3$. However, the role played by the particles in dissipation of the primary vortex is unclear since the vortex breakdown process in this region is highly stochastic.

In the eroded bed case, there is a strong spatial correlation between the suspended load, the location of crest on the surface f the bed form and the location primary vortex. Similar to the flat bed case, suspended load is higher when the vortex has dissipated. There are regions of high concentration in

the eroded bed case where the particle identification routine is not effective as shown in Fig. 5.9, hence these regions are excluded while estimating particle statistics. This results in a conservative approximation of particle volume fraction in the eroded bed case.

It should be noted that these tests were conducted at a fixed forcing frequency of 35 Hz. In terms of suspension, if the forcing frequency is increased, the particles entrained by a vortex into suspension will have less time to settle back onto the bed before another vortex traps them and keeps them suspended. This is akin to increasing the number of blades on the rotor thereby increasing the rate of generation of tip vortices. If the forcing frequency is reduced, the suspension state approaches that of an interaction of a single vortex embedded in a wall jet. The particles will have ample amount of time to get entrained into the flow, move radially outward and settle back onto the bed before another vortex starts the process all over again.

5.2.1 Concentration and Volume fraction

In this study, the particle-sampled statistics are binned on a regularly spaced grid to determine Eulerian statistical average quantities. The phase averaged concentration, defined as the average number of particles at a location (x, y) per unit volume on a uniform grid, is given by

$$\widehat{c}(x,y) = \frac{1}{\Delta V}\frac{1}{N_s}\sum_{N_s}\sum_{i=1}^{N_p}\delta((x - x_p^{(i)}),(y - y_p^{(i)})) \quad \text{where} \tag{29}$$

ΔV is the small averaging volume or bin given by $\delta x \delta y \delta z$ corresponding to real world dimensions of $1.6mm \times 0.5mm \times 2.0mm$. The thickness of the measurement volume is estimated based on the calibration technique outlined

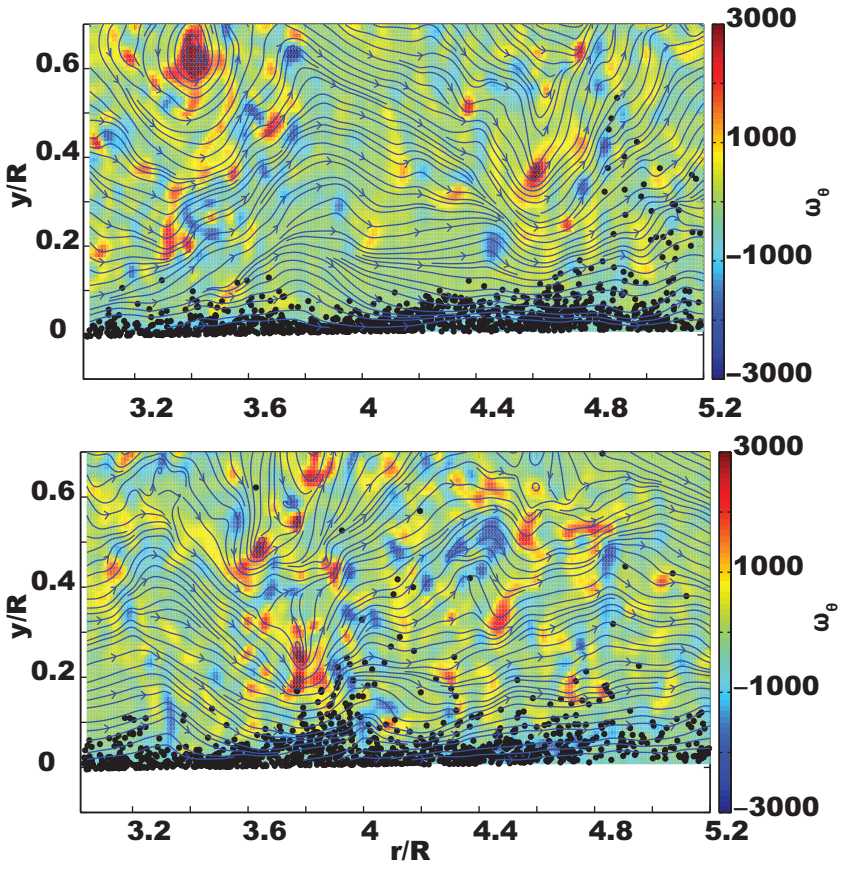

Figure 5.8: Instantaneous realizations showing vorticity contours with fluid streamlines and identified particles from the phase-separation routine for the flat bed case at $t/T = 0.5$

in Chapter 4. N_s is the total number of realizations captured at each phase angle and N_p is the total number of particles in each realization. It is apparent that $\delta((x - x_p^{(i)}), (y - y_p^{(i)})) = 1$ when the i^{th} particle centroid at (x_p, y_p) is inside the averaging bin at (x, y) or 0 otherwise. Concentration is related to volume fraction as

$$\Phi_v = c\frac{\pi d_p^3}{6} \tag{30}$$

The time average of the concentration can then be obtained by

$$\bar{c} = \frac{1}{\Psi}\sum \widehat{c} \quad \text{where} \tag{31}$$

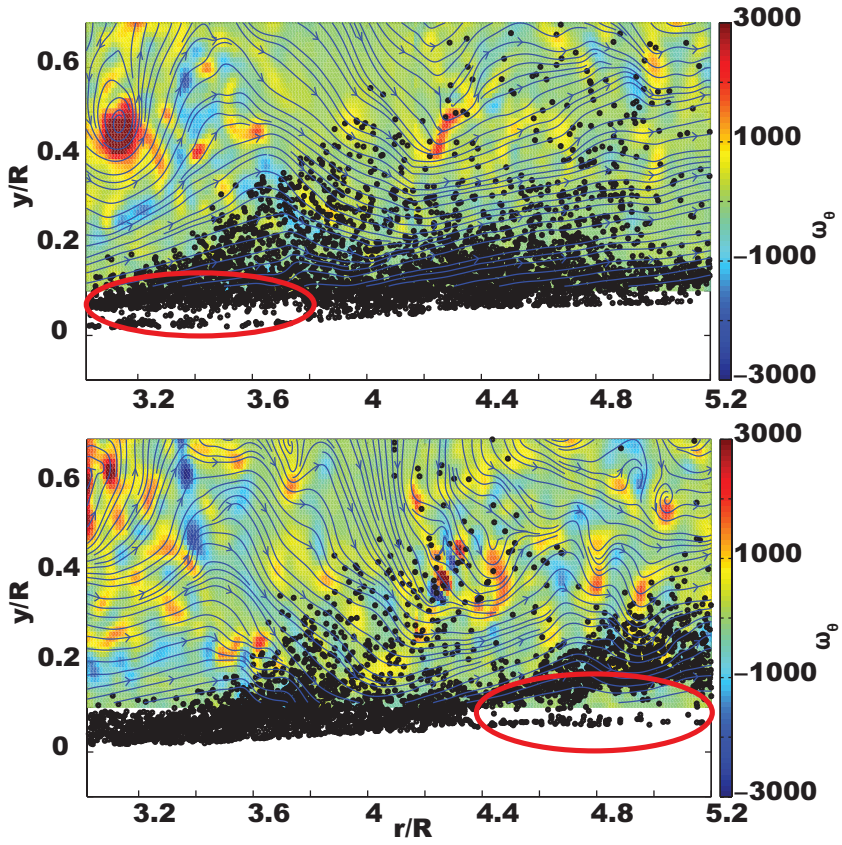

Figure 5.9: Instantaneous realizations showing vorticity contours with fluid streamlines and identified particles from the phase-separation routine for the eroded bed case at $t/T = 0.5$. Regions highlighted in red show the ineffectiveness of phase-separation routine in high concentration regions

Ψ is the total number of phase angles.

In order to obtain higher spatial resolution in the wall-normal direction for dispersed phase statistics, a rectangular grid with aspect ratio of 3:1 has been used. Statistics have been excluded at cells where the total number of particles over all phase realizations is below 15, in order to reduce noise. Although one might question the convergence of statistics due to limited number of samples taken (560 image pairs per phase angle of the cycle), we still believe the quantities are sufficiently converged (the standard deviation of mean particle velocities is less than 3%) to provide useful insights into the governing

mechanisms of the vortex-bed interaction and particle suspension process. The phase average particle velocity is then given by

$$\widehat{v_p}(x,y) = \frac{1}{N_a(x,y)} \frac{1}{N_p(x,y)} \sum_{N_a} \sum_{i=1}^{N_p} \delta\left((x - x_p^{(i)}), (y - y_p^{(i)})\right) v_p(x_p^{(i)}, y_p^{(i)}) \quad \text{where} \tag{32}$$

$N_a(x,y)$ is the number of realizations in the ensemble with at least one particle at location (x,y) and v_p is the i^{th} particle velocity located at $(x_p^{(i)}, y_p^{(i)})$.

Using the regular-spaced carrier phase PIV data, fluid velocity is extracted at each particle location by performing bi-cubic interpolation. Strictly speaking, the velocity of the fluid on the surface of a particle must match the motion of the local particle-fluid interface by virtue of the no-slip condition. However, for the current imaging and particle size conditions, this level of detail is beyond the resolution of the instrumentation. The velocities obtained by the PIV method (and hence the interpolated values used in the particle-conditioned average) inherently represent a volume-averaged velocity related to the size of the interrogation window. In order to estimate the local instantaneous slip velocity observed by individual particles, the instantaneous interpolated fluid velocity at the particle location is used in the definition. Therefore the average slip velocity is then obviously conditioned on the presence of the particle.

$$v_s(x_p^{(i)}, y_p^{(i)}) = v_{f@p}(x_p^{(i)}, y_p^{(i)}) - v_p(x_p^{(i)}, y_p^{(i)}) \tag{33}$$

$$\widehat{v_s}(x,y) = \frac{1}{N_a(x,y)} \frac{1}{N_p(x,y)} \sum_{N_a} \sum_{i=1}^{N_p} \delta((x - x_p^{(i)}), (y - y_p^{(i)})) v_s(x_p^{(i)}, y_p^{(i)}) \tag{34}$$

Shown in Fig. 5.10 are contours of particle volume fraction with slip velocities on the foreground for both the flat bed and eroded bed cases. The thick black lines at the bottom are the average bed profiles taken after each

data set has been acquired. These particles were initially mobilized by the excess stress from the vortex and are on an initial saltating trajectory as they are carried into the flow. This phenomenon is similar to particle mobilization in turbulent channel flows with one significant deviation in the form of a strong correlation between the location of the vortex core and volume fraction of particles. In the flat bed case, the particles are moving radially outward and the maximum height these particles get suspended corresponds to $y/R \approx 0.2$ at upstream locations. As the vortex gets dissipated and loses its coherence, the particles get entrained into the flow to greater heights ($y/R \approx 0.4$). The relative volume fraction also increases with increasing phase angle as the vortex undergoes stretching and its subsequent intensification, thus mobilizing even more particles on the bed surface. The ensemble averaged suspended flux for the flat bed conditions indicates a much thinner particle transport layer ($y/R < 0.2$), and a much greater spatial uniformity.

The slip velocity direction indicates that the particles are lagging behind the fluid close to the bed but as they enter suspension and gain momentum, they are leading the fluid at bed heights above $y/R \approx 0.3$. The magnitude of the slip is also highly influenced by the vortex, especially in the upstream region ($r/R < 4.2$), where it still has high coherence. In the eroded bed case, the volume fraction is much higher with a strong correlation to the location of crest on the bed profile at $r/R \approx 3$ (Fig. 5.6). The initial plume seen at $r/R \approx 3.2$ is due to vortex impinging on that crest and particles getting ejected and immediately entering suspension. The location of high volume fraction suspension clouds and maximum slip velocity are strongly correlated to the location and strength of the primary vortex. Similar to the flat bed case, the particles are lagging behind close to the ground but as suspension height increases, they are moving faster than the fluid. However, the magnitude of

slip velocity is almost twice compared to the flat bed case when the particles are leading in the eroded bed case. In both the cases, the slip velocity of particles in suspension higher than $y/R \approx 0.3$ is directed towards the ground indicating that these particles are moving away from the ground and their vertical component of velocity is greater than the fluid vertical velocity. They have gained enough momentum from the fluid and are being pushed further into the outer flow by virtue of their inertia.

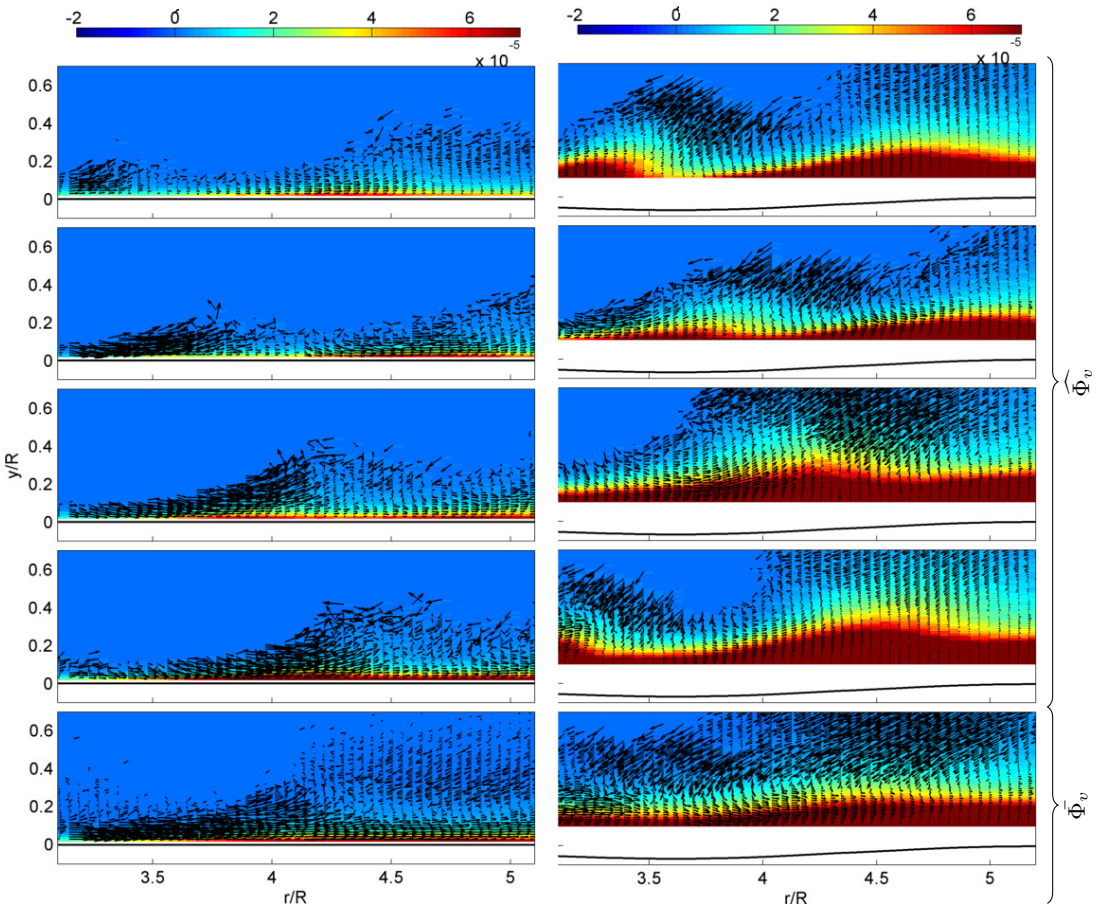

(a) Flat Bed (b) Eroded Bed

Figure 5.10: Contours of particle volume fraction (Φ_v) with slip velocities on the foreground for (a) Flat Bed (b) Eroded Bed. The four phase averages are calculated at $t/T = 0.25, t/T = 0.5, t/T = 0.75$ and $t/T = 1.0$

5.2.2 Particle Flux

The phase-averaged particle flux is defined as:

$$\widehat{cv_p}(x,y) = \frac{1}{N_s(x,y)} \sum_{N_a} \sum_{i=1}^{N_p} \delta((x - x_p^{(i)}), (y - y_p^{(i)})) v_p(x_p^{(i)}, y_p^{(i)}) \qquad (35)$$

Shown in Fig. 5.11 and Fig. 5.12 are the vertical fluid velocities and the mean vertical particle fluxes for the flat and eroded beds respectively. The vertical flux is predominantly positive in both the cases with a strong correlation to the positive vertical fluid velocity. There are small pockets of negative flux just below the primary vortex as it enters the measurement domain at $t/T = 0.25$. It shows that a small fraction of suspended particles get entrained by the secondary counter-rotating vortex and are pushed towards the ground as also qualitatively shown by Munro et al (2009) [30]. This is especially evident in the eroded bed case at $r/R = 3.2$ where a small plume of particles that are lagging behind the primary vortex are pushed towards the ground by the negative vorticity associated with the next vortex ring entering the measurement domain at $t/T = 1.0$. The steady state settling velocity of these particles assuming Stokes drag is about 0.15 m/s and the mean downward velocity in the region of negative flux is 0.2 m/s which indicates that the negative vorticity, even though not directly visible, has its effect on the suspended particles. It also means that the particles are actually bombarding the bed, which will potentially result in ejection of even more particles. As the primary vortex reaches the downstream imaging region, it begins to dissipate and the positive wall-normal particle flux becomes dominant, as the suspended particles from upstream are being carried radially outward and away from the ground by the mean flow. The particle flux calculated in the eroded bed case is a conservative estimate given the fact that the high concentration region near the bed is excluded. However, the vertical

flux is still nearly three times the vertical flux in the flat bed case owing to the presence of the crest at $r/R \approx 3$.

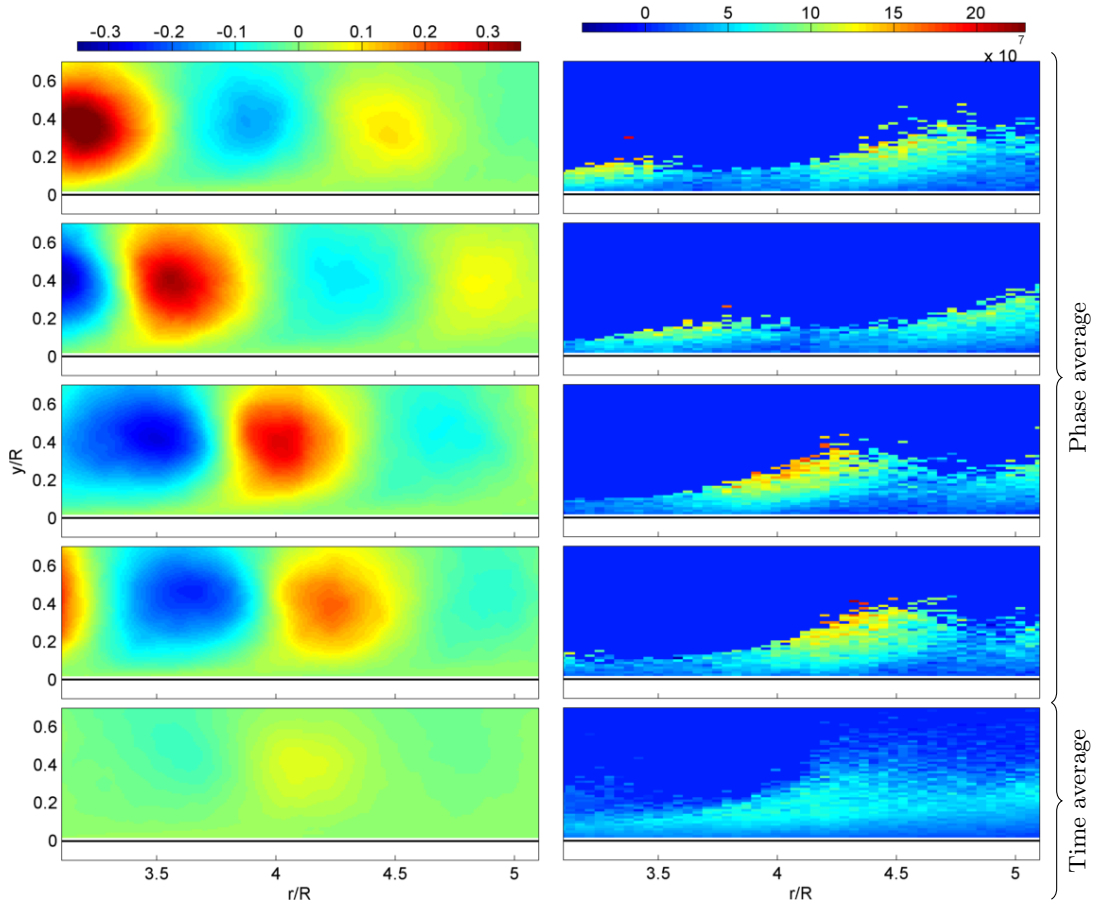

(a) Vertical fluid velocity (b) Vertical particle flux

Figure 5.11: (a) Contours of vertical fluid velocity (v_{fy}/V_o) for flat bed case, and (b) vertical particle flux (cv_{py}/V_o) for flat bed case. The four phase averages are calculated at $t/T = 0.25, t/T = 0.5, t/T = 0.75$ and $t/T = 1.0$

Fig. 5.13 depicts the contours of phase-averaged radial particle flux. Waves of suspended sediment are evident moving through the region, with significant positive flux as high as $y/R = 0.4$ for the flat bed case and $y/R = 0.6$ for the eroded bed case, occupying more than half the thickness of the wall-jet at this point. The phasing of the sediment cloud corresponds directly to the presence of the primary vortex, with a maximum flux slightly downstream of

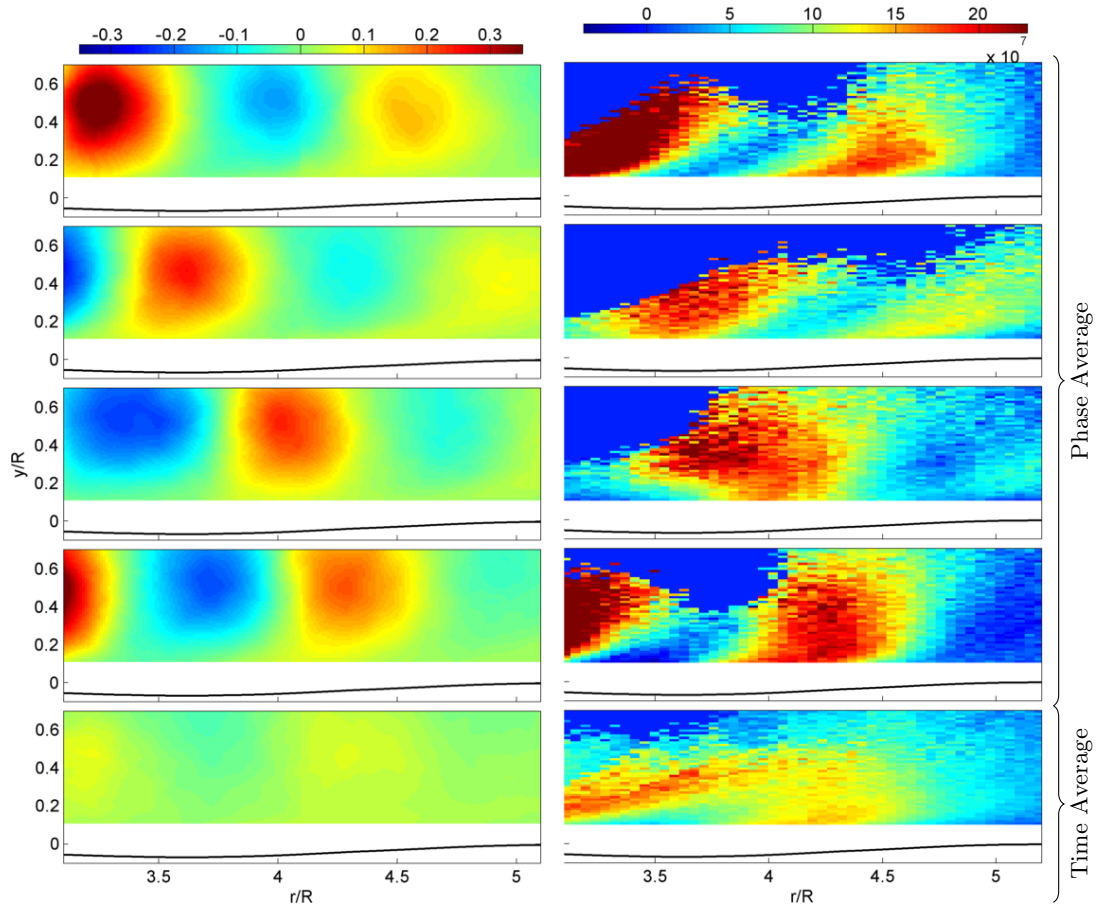

(a) Vertical fluid velocity (b) Vertical particle flux

Figure 5.12: (a) Contours of vertical fluid velocity (u_{fy}/V_o) for eroded bed case, and (b) vertical particle flux (cv_{py}/V_o) for eroded bed case. The four phase averages are calculated at $t/T = 0.25, t/T = 0.5, t/T = 0.75$ and $t/T = 1.0$

the primary vortex core. The total phase-averaged mass flux (depth integrated) per unit volume can be defined as

$$\widehat{\Upsilon} = \frac{\rho_p d_p^3}{6} \int_0^H \widehat{cv_{pr}} \delta z dy \tag{36}$$

Looking at the total particle mass flux (Fig. 5.14), one can see a strong spatial correlation between the location of the vortex core and local maxima of radial particle flux. From Fig. 5.15, it is evident that although there are strong temporal and spatial variations in the instantaneous flux, the time-averaged suspended transport for the eroded bed shows a fairly constant value over the measurement region, increasing only 30% as one approaches the second crest. In contrast to this, the flat bed conditions in the early flow evolution show a strongly evolving suspended flux rate, increasing continually from values near zero at $r/R = 3.0$, to about half the eroded bed flux at radial position of $r/R = 5$, showing an increase of nearly 90% along the radial direction. This would seem to imply that the flat bed case is still evolving towards its equilibrium conditions, with the rate of particles coming into suspension continually exceeding those falling back to the wall during their saltation events.

5.2.3 Particle-turbulence interaction

1. **Streamwise Velocity:**

   Now that the effect of fluid motion on particle motion has been examined, the next logical step would be to study the influence of particles on fluid motion to understand the coupling between the phases. Fig. 5.16 and Fig. 5.17 show the contours of magnitude of fluid and particle velocity for the flat and eroded bed cases. The fluid flow looks very similar in both the cases on first look but differences will emerge when one exam-

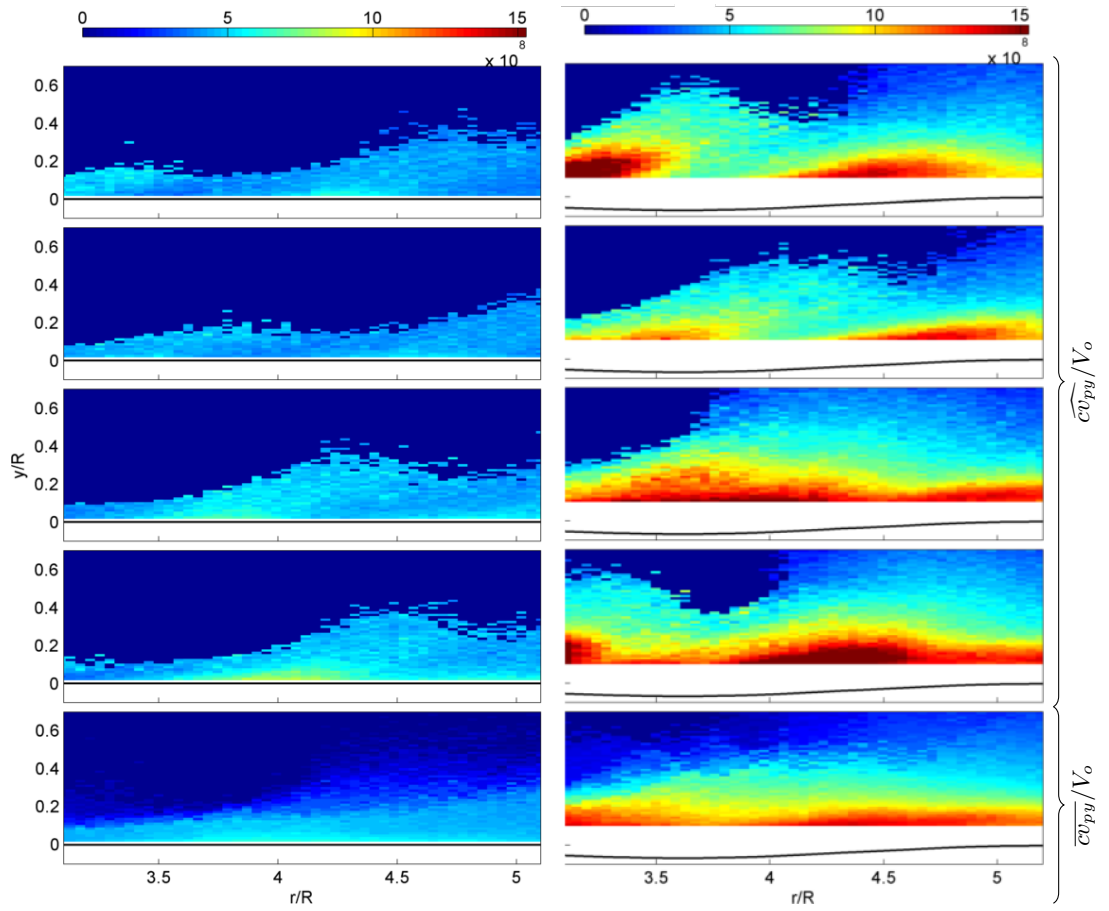

(a) Flat Bed (b) Eroded Bed

Figure 5.13: (a) Contours of phase-averaged radial particle flux (cv_{py}/V_o) for a) flat bed case, and (b) eroded bed case. The four phase averages are calculated at $t/T = 0.25, t/T = 0.5, t/T = 0.75$ and $t/T = 1.0$

ines the velocity profiles more carefully. Fig. 5.18 represents the radial fluid velocity for the single-phase flow, two-phase flow as well as the radial particle velocity under flat bed and eroded bed conditions at four different radial locations. It is observed that the presence of the particles modulates both the velocity gradients as well as the magnitude of the fluid velocity. The behavior is not consistent in the flat bed case as it starts out with damping near the wall at $r/R = 3$. At farther radial locations, the fluid velocity in the flat bed case gets augmented and even-

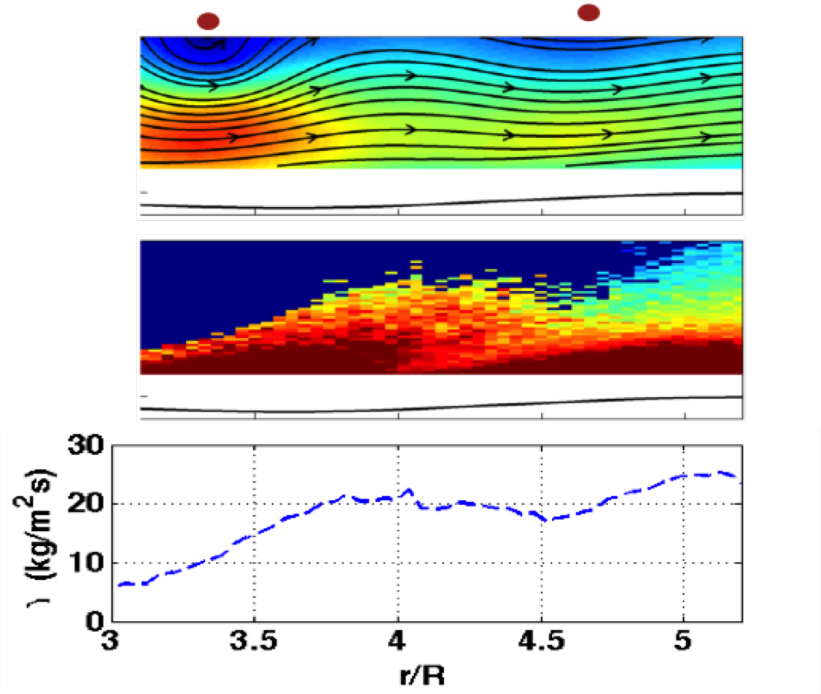

Figure 5.14: Phase-averaged fluid velocity showing location of the vortex core and its spatial correlation with radial particle flux and total radial sediment transport at $t/T = 0.25$

tually reaches a state similar to the eroded bed case (damping close to the wall and augmentation away from the wall). In the eroded bed case, the fluid velocity is damped close to the wall and is augmented in the outer flow. It means that the fluid Reynolds stresses decrease where the particle concentration is high close to the bed and increase where the particle concentration is low in the outer flow. This will be discussed further in a later section. The height where this switch in fluid behavior happens is a function of both radial location and particle concentration. It indicates that the particles are extracting momentum from the fluid in the inner flow and giving it back to the fluid in the outer flow. This mechanism is also supported by fact that the momentum flux of the fluid increases for both flat and eroded bed cases with increasing radial location (Fig. 5.19).

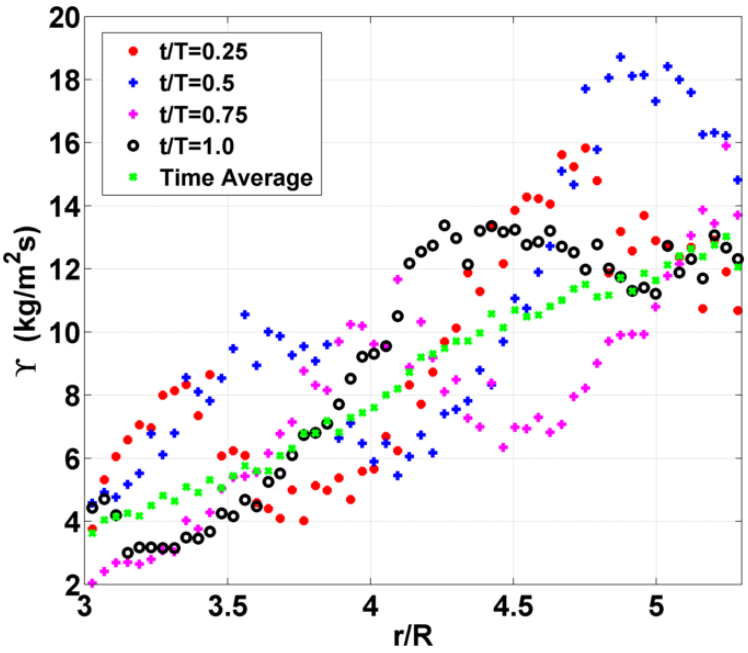

(a) Flat Bed

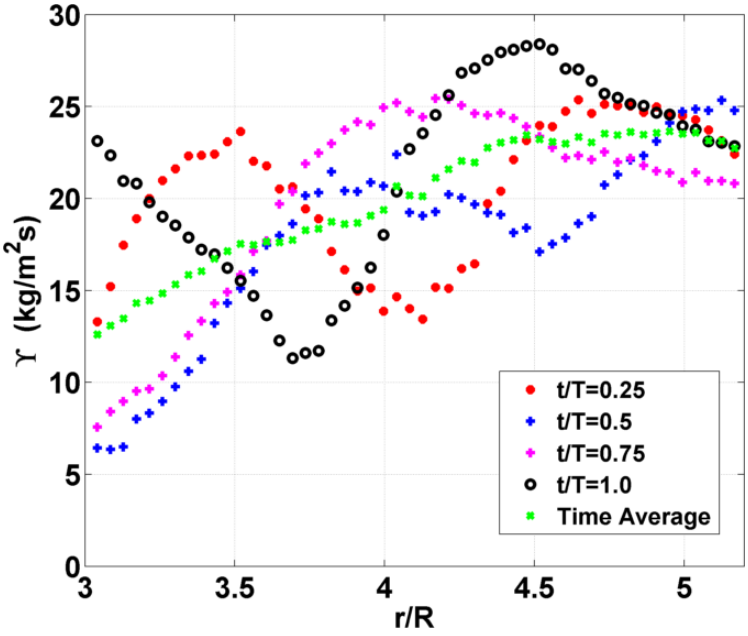

(b) Eroded Bed

Figure 5.15: Depth averaged particle mass flux as a function of radial position

Momentum flux is calculated by

$$K = \int_0^\infty r u_r^2 dy. \tag{37}$$

The value of K is normalized by the momentum flux at $r/R = 4.0$ for the single-phase flow. The momentum flux decays by about 15% as one moves from $r/R = 3.0$ to $r/R = 5.0$ in the single-phase flow, which is expected due to friction from the wall. The decrease in momentum flux in the current forced jet case is 3 times higher in magnitude compared to the measurements made by Krishnan and Mohseni [46] for their free wall-jet. Fig. 5.19 also shows that the fluid momentum increases with increasing radial location in the presence of particles (about 18% for flat bed case and 25% for eroded bed case), indicating that the momentum is being transferred back to fluid by the suspended particles. This behavior is consistent with the findings of Kaftori et al. (1998) [47] for small particle sizes ($d_p = 100\mu m$), where they looked at dilute suspensions of near-neutrally buoyant particles in turbulent channel flow.

The damping effect close to the bed surface is also observed in gas/solid and solid/liquid flows ([25], [27]). Examining the radial velocity of the particle-phase, it is obvious that the particles consistently lag behind the fluid for the flat bed case while in the eroded bed case, the particles are moving faster than the fluid at radial locations $r/R > 4.0$. Such velocity distributions are similar to those observed by previous researchers for both gas-solid ([51], [52]) and liquid-solid ([48], [25]) flows.

2. **Wall-normal velocity**

Looking at the wall-normal velocity profiles at the same locations in Fig. 5.20, it is evident that the particles are moving faster than the fluid in both flat and eroded bed cases. The fluid velocities are augmented as well as attenuated depending on the radial position.

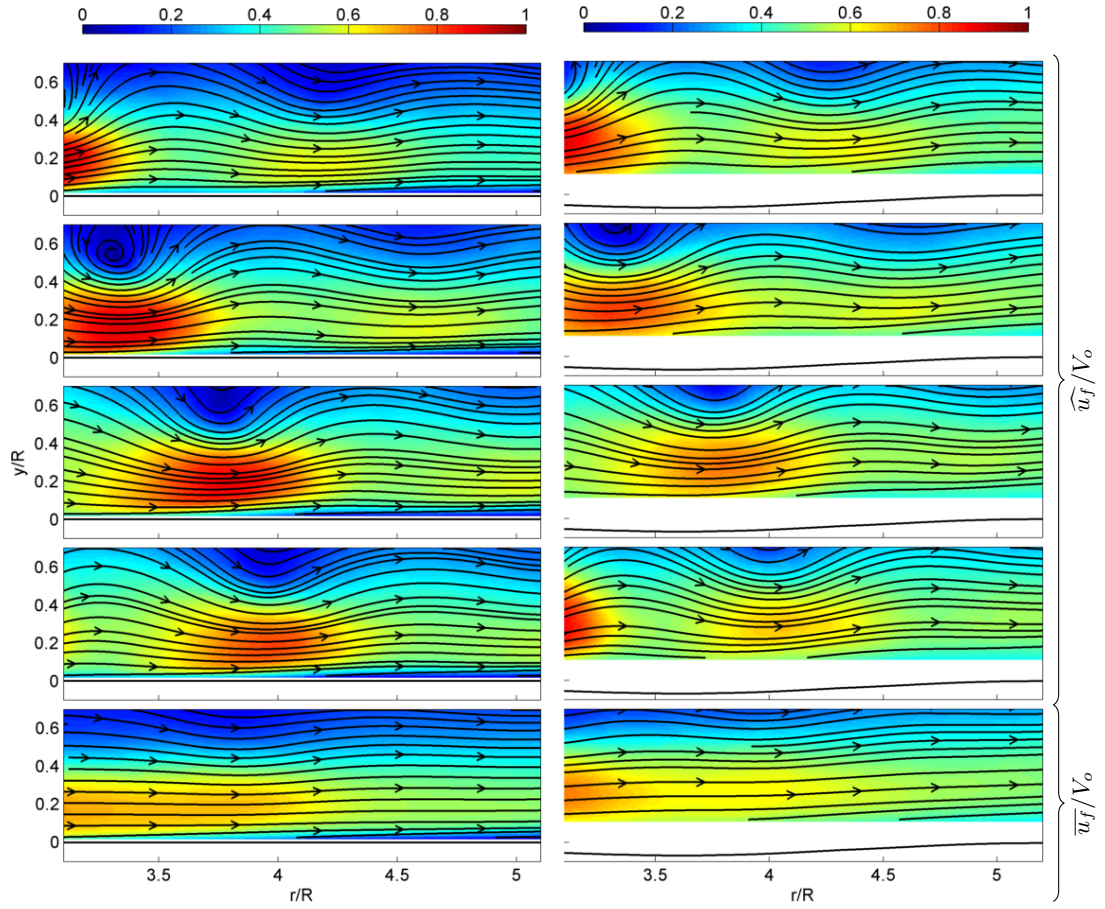

(a) Flat Bed (b) Eroded Bed

Figure 5.16: (a) Contours of fluid velocity magnitude u_f/V_o with fluid streamlines for a) flat bed case, and (b) eroded bed case. The four phase averages are calculated at $t/T = 0.25, t/T = 0.5, t/T = 0.75$ and $t/T = 1.0$

3. Fluid Turbulence fluctuations

Fig. 5.21 and Fig. 5.22 show the streamwise and wall-normal fluid RMS velocities at different radial locations. The maximum of $u_{f,rms}$ and $v_{f,rms}$ occurs at $y/R \approx 0.4$. The presence of the particles translates these profiles into the outer flow except at $r/R < 4.0$ for the flat bed case, where it is translated closer to the bed surface. At all other radial locations for flat bed case and every radial location in the eroded bed case, there is also a significant amount of damping in the RMS velocities for $y/R < 0.5$

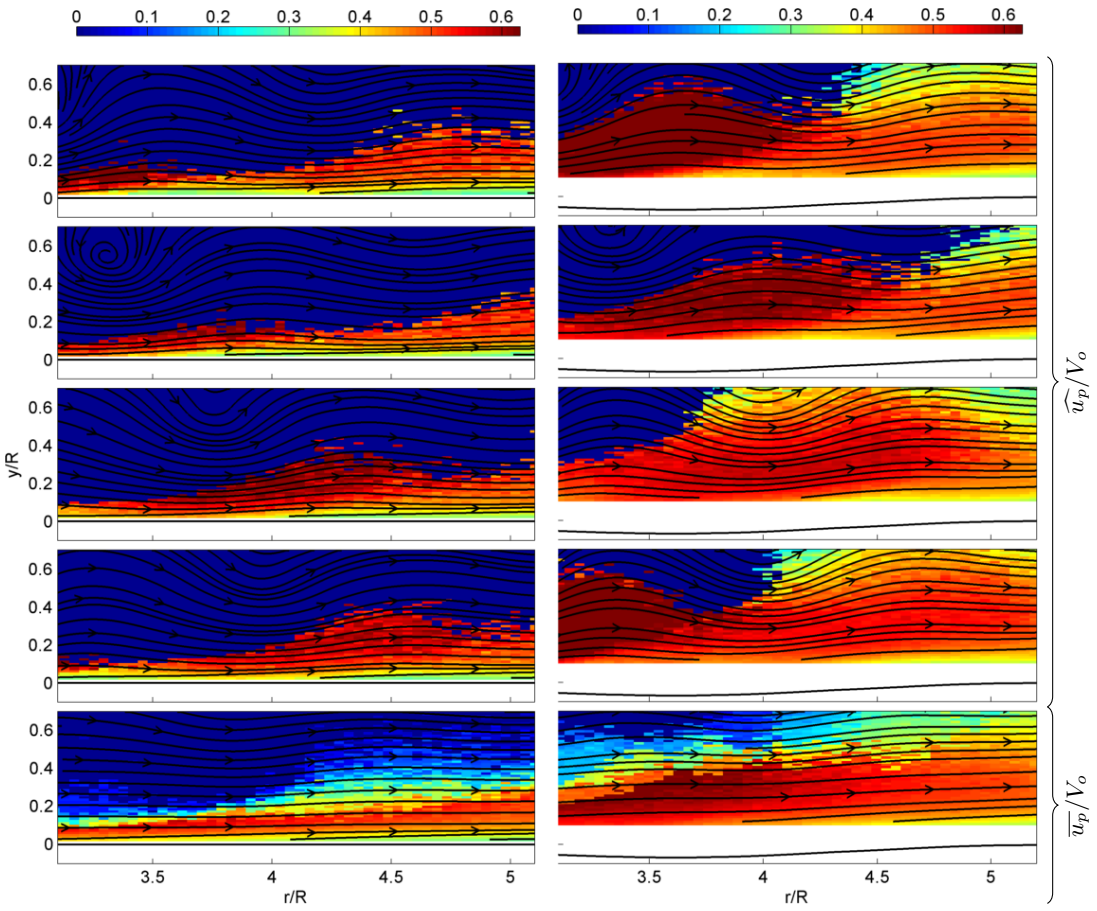

(a) Flat Bed (b) Eroded Bed

Figure 5.17: (a) Contours of particle velocity magnitude u_p/V_o with fluid streamlines for a) flat bed case, and (b) eroded bed case. The four phase averages are calculated at $t/T = 0.25, t/T = 0.5, t/T = 0.75$ and $t/T = 1.0$

for the eroded bed case, while in the outer flow, both $u_{f,rms}$ and $v_{f,rms}$ are augmented. The damping is higher for the eroded bed case (10 - 15% based on the peak value). This indicates that the attenuation of turbulence fluctuations is a strong function of particle volume fraction. In the outer flow, the presence of the particles enhances both stream wise and wall normal RMS velocities.

The behavior of the stream wise RMS velocities for eroded bed case is consistent with the results from Tanière et al. (1997) [52] where they reported

a similar decrease in the streamwise fluid fluctuations for $y/\delta < 0.35$, where δ is the boundary layer thickness, with a slight increase in the outer region for similar density ratio and Stokes number ($\rho_p/\rho_f \approx 2100$ and $St \approx 4$). Li et al [27] also reported similar behavior for the stream wise RMS velocities in their experiments with a similar Stokes number but a lower density ratio ($\rho_p/\rho_f \approx 1000$ and $St \approx 4.7$). The unsteady nature of this flow not only magnified the modulation of turbulence fluctuations but also propagated the damping effect further into the outer flow compared to these two studies conducted in turbulent channel flows. Rashidi et al. (1990) [49] and Wu et al. (2006) showed a similar fluctuation increase in the outer flow for large particles ($d_p = 1100\mu m$), with low Stokes numbers ($St \approx 0.3$). However, some studies contradict this behavior, for example results of Tsuji and Morikawa (1982) [51] from a horizontal pipe flow indicate a strong damping of the streamwise fluid fluctuations from fine particles ($50 < St < 150$) over all cross-stream locations, as do the vertical channel results of Kulick et al. (1994) [53] ($10 < St < 50$).

The damping of wall-normal RMS velocities and subsequent augmentation in the outer flow is due to the large vertical velocity gradients introduced by the vortex. The suspension is dominated by this large scale fluid structure as opposed to rough wall effects in turbulent channel flows. Therefore this behavior is not consistent with existing literature, in fact, most of the turbulent channel flow studies ([25], [54] and [55]) indicate the opposite behavior, i.e., the wall-normal turbulent fluctuations are enhanced close to the wall due to the rough-wall effect while in the outer flow, the fluctuations are slightly suppressed. These are however, fully-developed turbulent channel flows and an important distinction between these studies and the present case is that there is a periodic, coherent

large scale fluid structure embedded within the mean flow.

4. **Fluid Reynolds Stresses**

   The effect of particles on fluid Reynolds stress, as shown in Fig. 5.24 and Fig. 5.23 is similar to their effect on RMS velocities. For example, the presence of the particles enhances fluid Reynolds stress for $y/R > 0.5$ compared to the single phase flow, while it is suppressed at heights $y/R < 0.5$ for the eroded bed case. Righetti and Romano (2004) [54] also observed similar phenomenon, although at higher mass loadings.

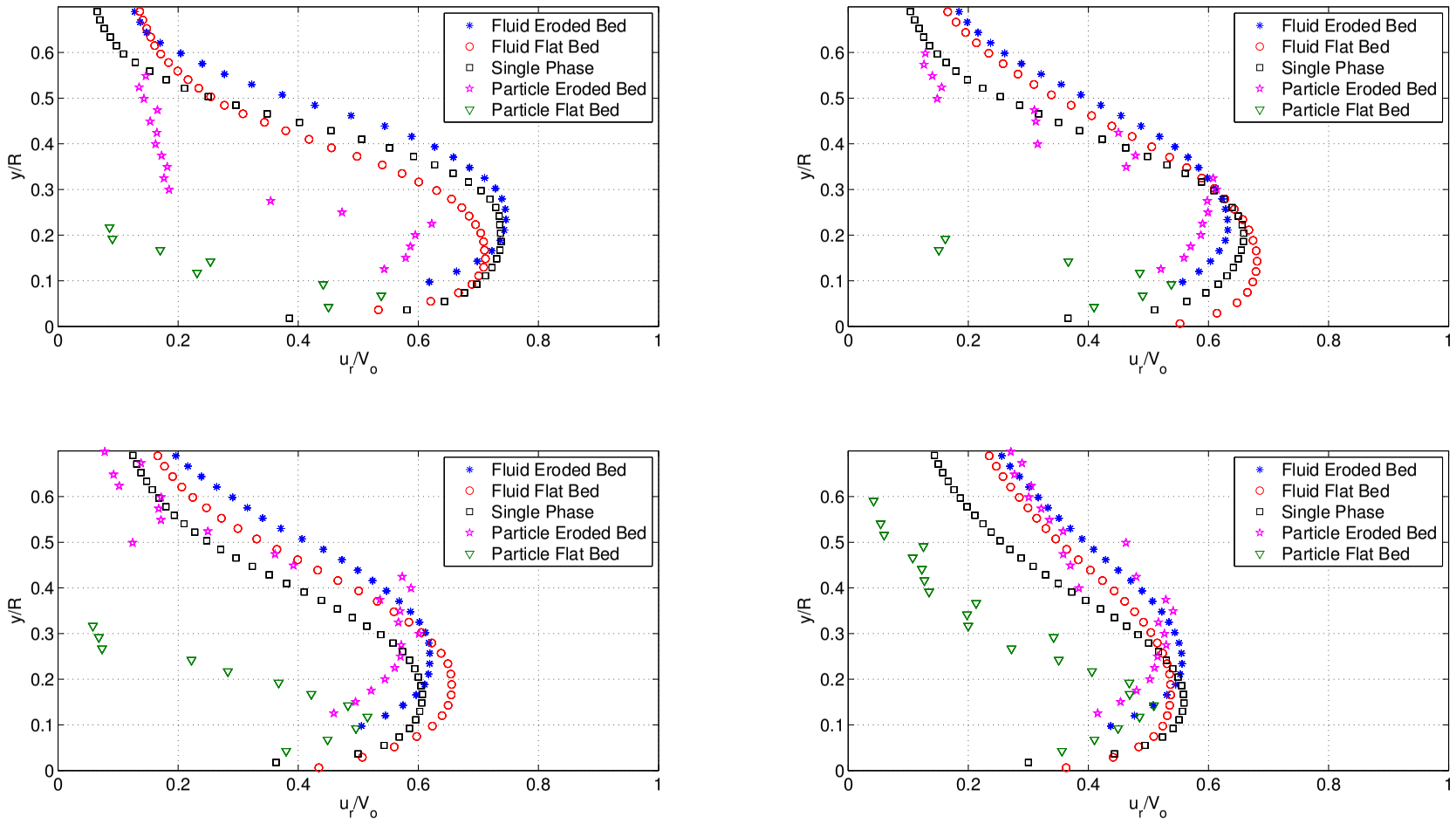

Figure 5.18: Time averaged streamwise fluid and particle velocities at a) $r/R = 3.0$, b) $r/R = 3.5$, c) $r/R = 4.0$, d) $r/R = 4.5$.

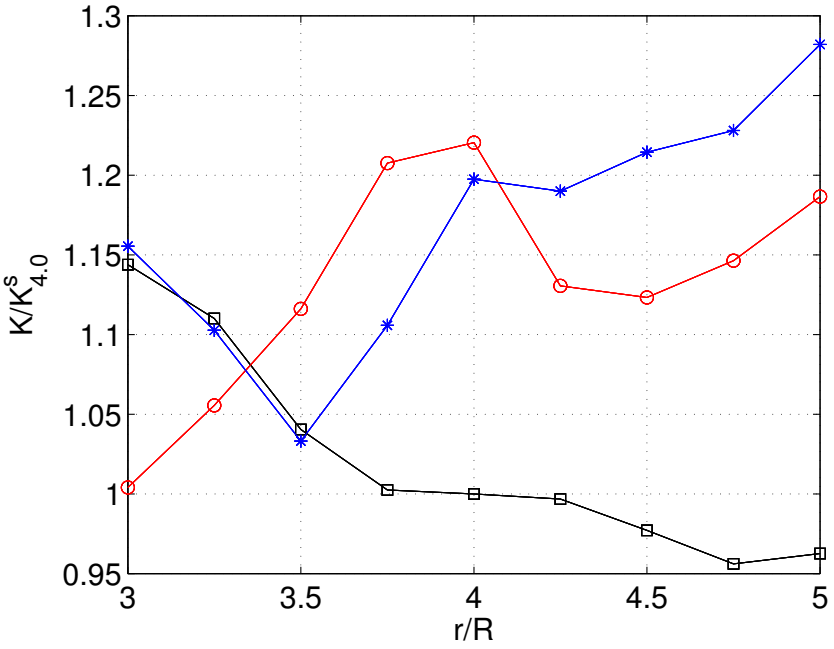

Figure 5.19: Normalized momentum flux for single-phase and two-phase flow conditions

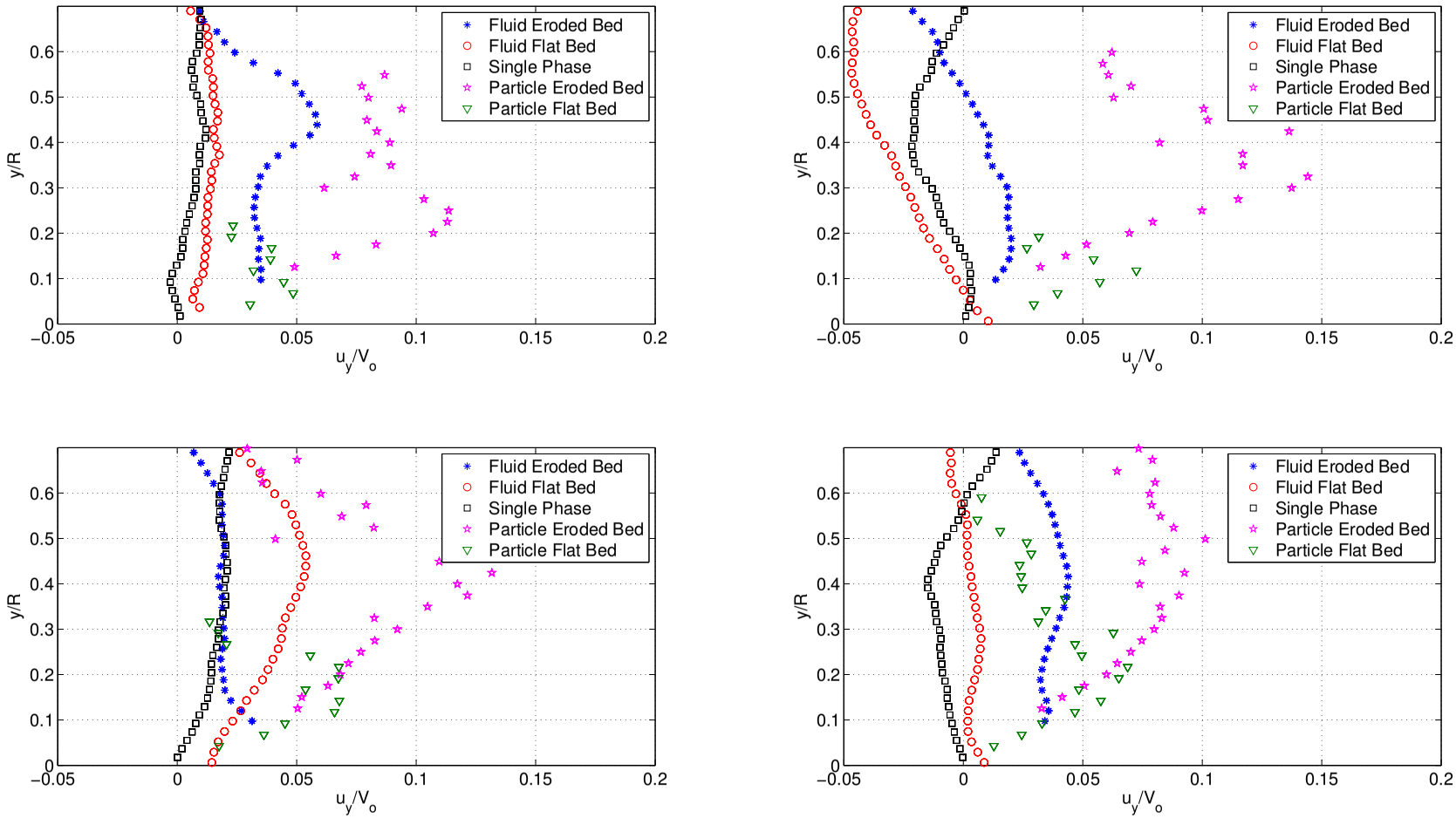

Figure 5.20: Time averaged wall-normal fluid and particle velocities at a) $r/R = 3.0$, b) $r/R = 3.5$, c) $r/R = 4.0$, d) $r/R = 4.5$.

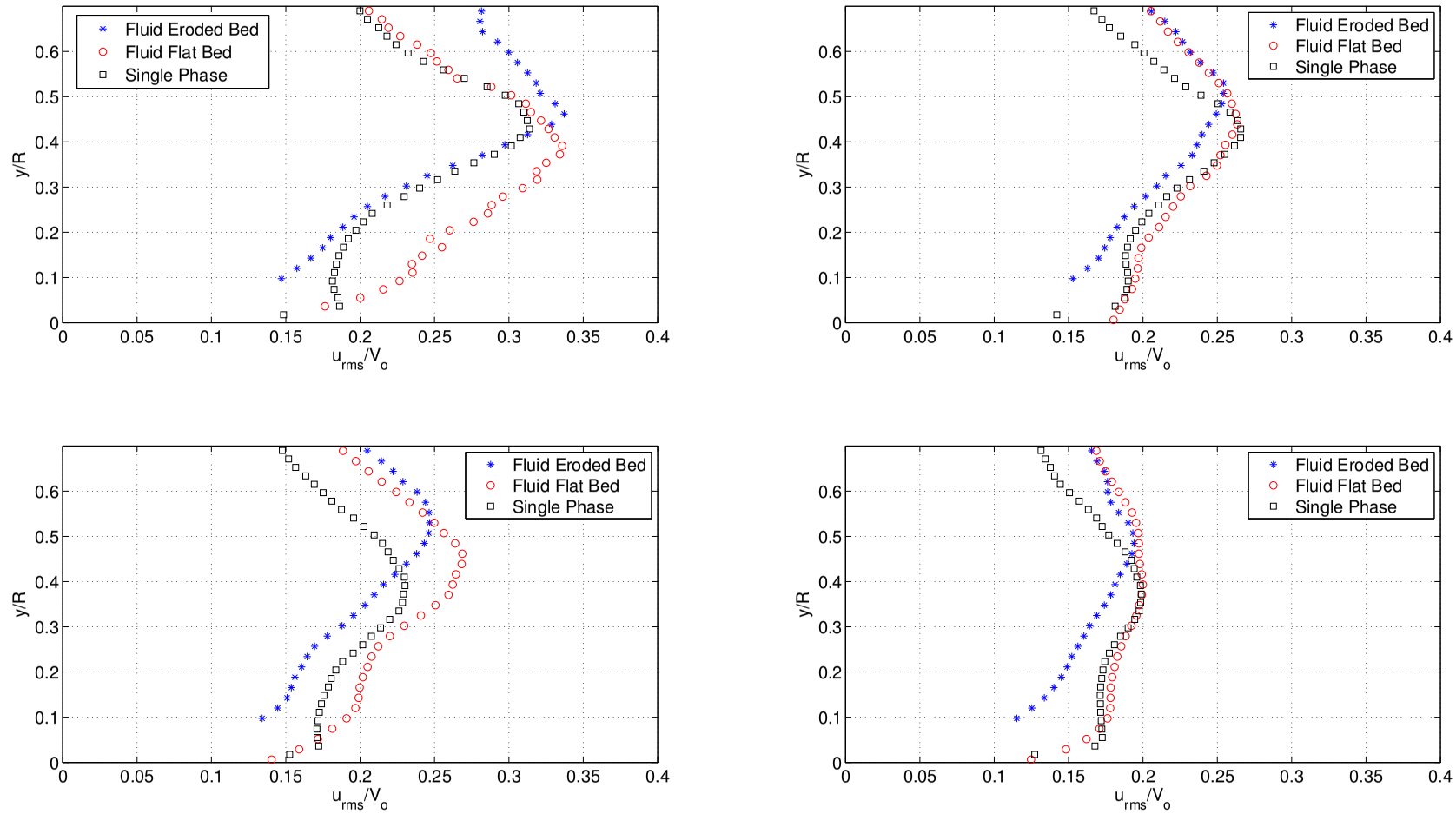

Figure 5.21: Time averaged streamwise fluid RMS velocities ($\overline{u_{f,rms}}$) at a) $r/R = 3.0$, b) $r/R = 3.5$, c) $r/R = 4.0$, d) $r/R = 4.5$

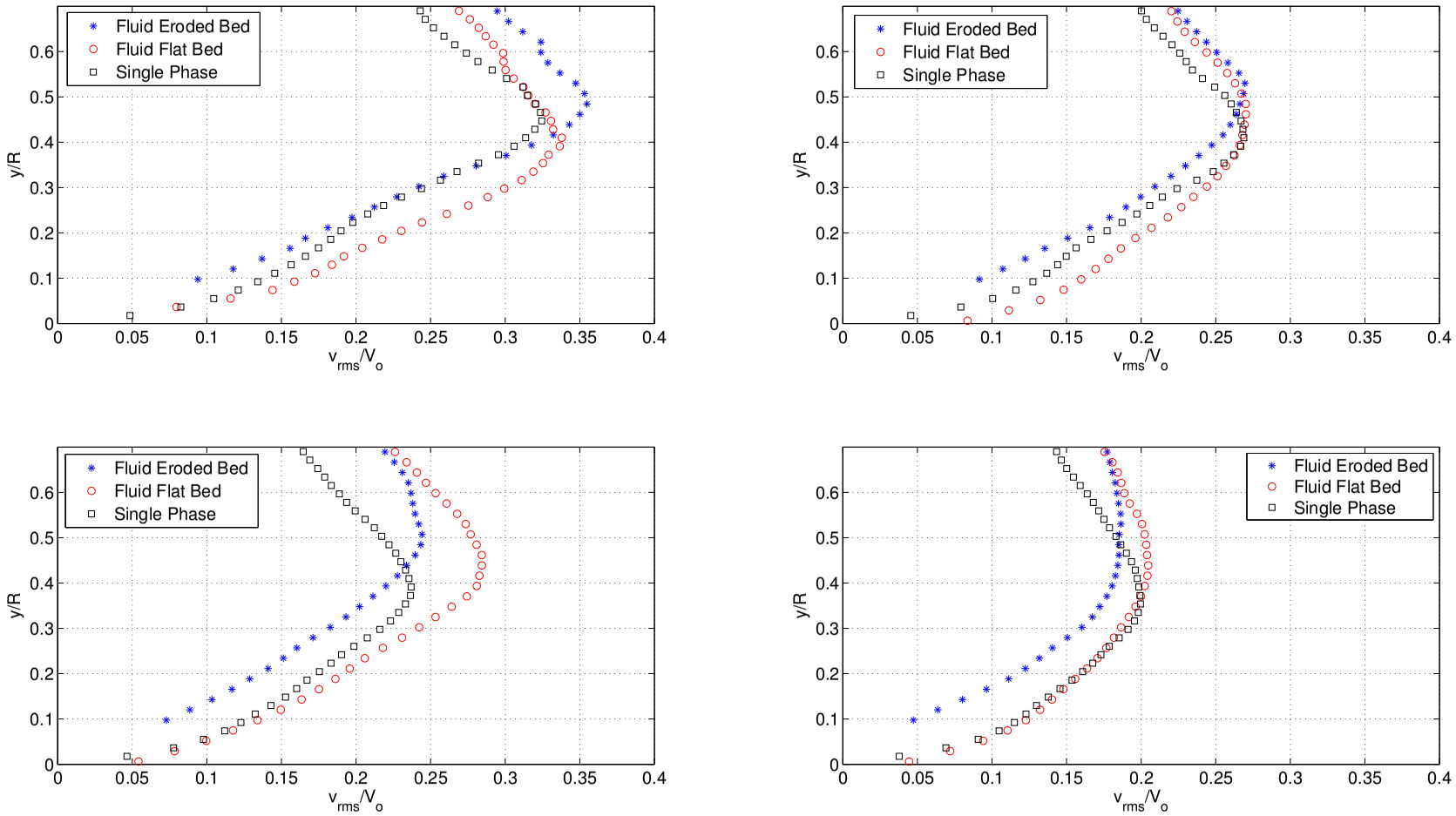

Figure 5.22: Time averaged wall-normal fluid RMS velocities ($\overline{v_{f,rms}}$) at a) $r/R = 3.0$, b) $r/R = 3.5$, c) $r/R = 4.0$, d) $r/R = 4.5$

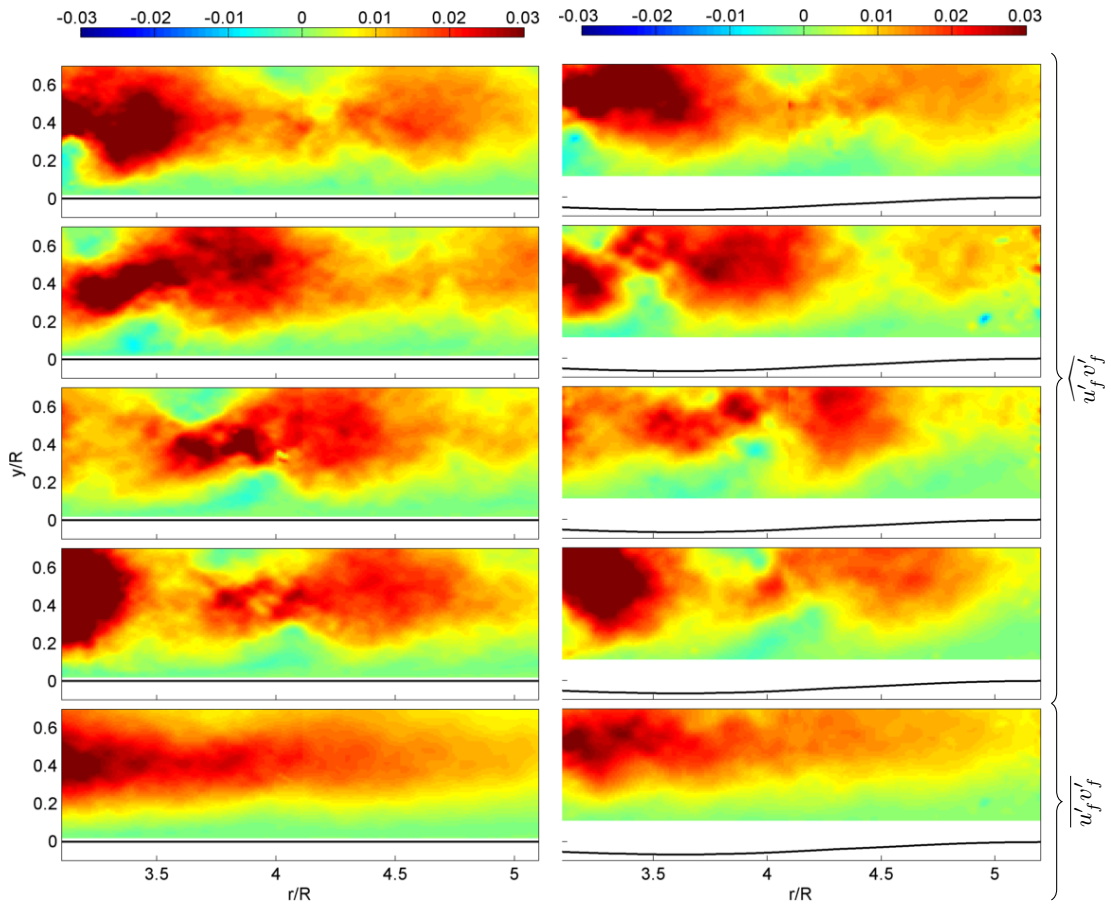

(a) Flat Bed (b) Eroded Bed

Figure 5.23: (a) Contours of fluid Reynolds stresses $\left(u'_f v'_f\right)$ for a) flat bed case, and (b) eroded bed case. The four phase averages are calculated at $t/T = 0.25, t/T = 0.5, t/T = 0.75$ and $t/T = 1.0$

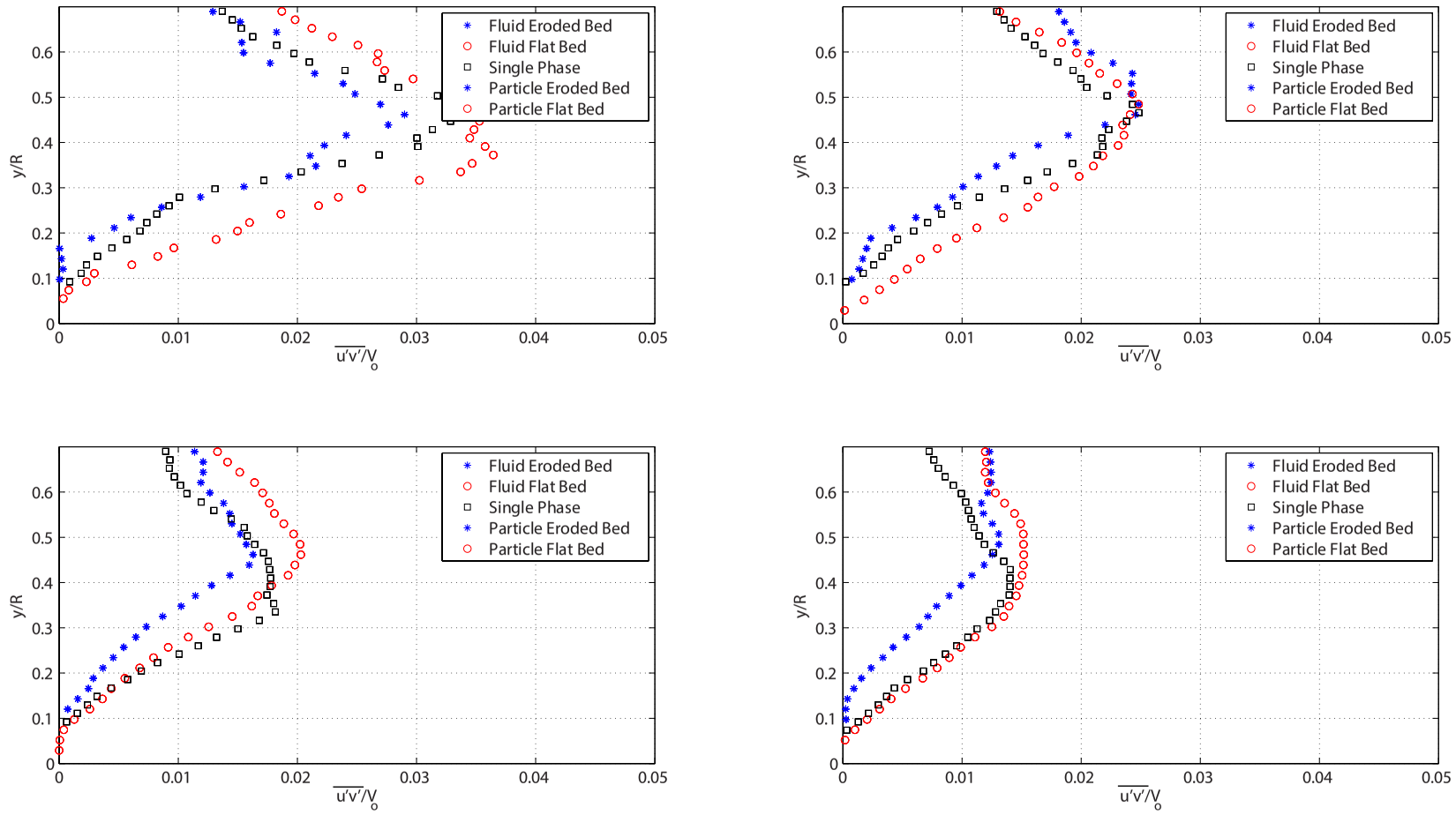

Figure 5.24: Time averaged fluid Reynolds stress ($\overline{u'v'}$) at a) $r/R = 3.0$, b) $r/R = 3.5$, c) $r/R = 4.0$, d) $r/R = 4.5$

5.2.4 Inter-phase momentum transfer

The inter-phase momentum transfer couples the momentum equations for the carrier and dispersed phases. In general, the drag force, the added mass effect, Bassett history force and lift forces are considered. However, DNS simulations by Armenio and Fiorotto (2001) [56] have shown that over a wide range of turbulence to particle time scales, with Stokes numbers varying from 0.025 to 10 and density ratio's of 2.6 and above, the particle drag is roughly an order of magnitude larger than the Bassett history force and three orders of magnitude larger than the added mass and lift forces. So the interfacial momentum exchange is approximated to a first order by taking only the dominant drag force into consideration while neglecting all the other terms.

Equations 9 and 10 from chapter 2 define the drag force as a function of local concentration. The drag coefficient is a function of both slip velocity magnitude as well as concentration and therefore will have mean and fluctuating component. Applying the averaging operator on the drag force, we get

$$\widehat{\boldsymbol{F_d}} = \left(\widehat{C_d} + C_d'\right)\left(\widehat{c}\widehat{\boldsymbol{v_s}} + \widehat{c'\boldsymbol{v_s'}}\right) \tag{38}$$

The drag coefficient is given by

$$C_d = \frac{\rho_f \nu}{d_p^2}\left(18.0 + 0.3Re_p\right)\frac{1}{(1-\Phi_v)^n} \tag{39}$$

The factor n depends on the particle Reynolds number as follows:

$$n = \begin{cases} 4.35Re_p^{-0.03} - 1 & 0.2 \leqslant Re_p \leqslant 1.0 \\ 4.45Re_p^{-0.1} - 1 & 1.0 \leqslant Re_p \leqslant 500 \\ 1.39 & 500 \leqslant Re_p \end{cases} \tag{40}$$

Since the maximum particle volume fraction is of the order of 10^{-4}, the effect of local volume fraction on the drag coefficient can be neglected. Under the assumption of dilute flow, the drag coefficient is a function of Reynolds number alone. Shown in Fig. 5.25 is the spatial variation of phase-averaged radial Reynolds number based on slip velocity, which is used to calculate the local radial drag coefficient. The maximum phase-averaged particle Reynolds number for both flat and eroded bed cases is about 4. By neglecting the stochastic variation of Reynolds number, the average drag equation becomes

$$\widehat{\boldsymbol{F_d}} = \widehat{C_d}\left(\widehat{c}\widehat{\boldsymbol{v_s}} + \widehat{c'\boldsymbol{v_s'}}\right) \tag{41}$$

The first term on the right hand side is the contribution from ensemble phase-averaged components of concentration and slip velocity while the second term is the contribution from stochastic variations in concentration and slip velocity. The stochastic component is calculated indirectly because when no particles are present in the averaging volume, c' is its maximum negative value, while v_s' is undefined (because slip velocity is a conditional averaged term, only calculated when a dispersed phase particle is present). To circumvent this ambiguity, these terms are calculated using the identity:

$$\widehat{\alpha'\beta'} = \widehat{\alpha\beta} - \widehat{\alpha}\widehat{\beta} \tag{42}$$

Fig. 5.26 shows the phase-averaged radial drag component which is dispersed into the upwash region of the flow and reaches a maximum as a large positive flux of particles gets ejected from the surface in the upstream region ($r/R < 4.0$) for both flat and eroded bed cases. In the downstream plane ($r/R > 4.0$), larger magnitude of the slip velocity of the particles moving

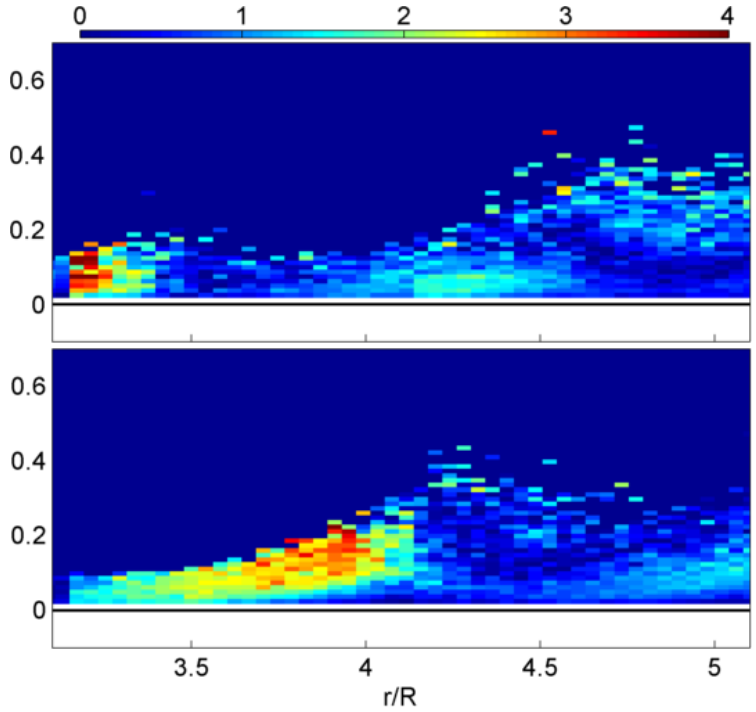

(a) Flat Bed

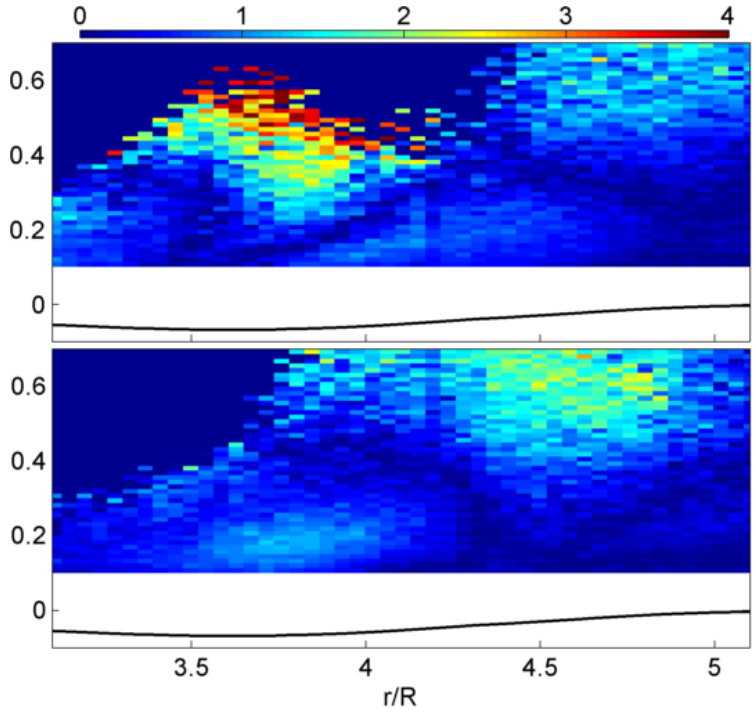

(b) Eroded Bed

Figure 5.25: Phase averaged particle Reynolds number at $t/T = 0.25$ and $t/T = 0.75$ for flat and eroded bed cases

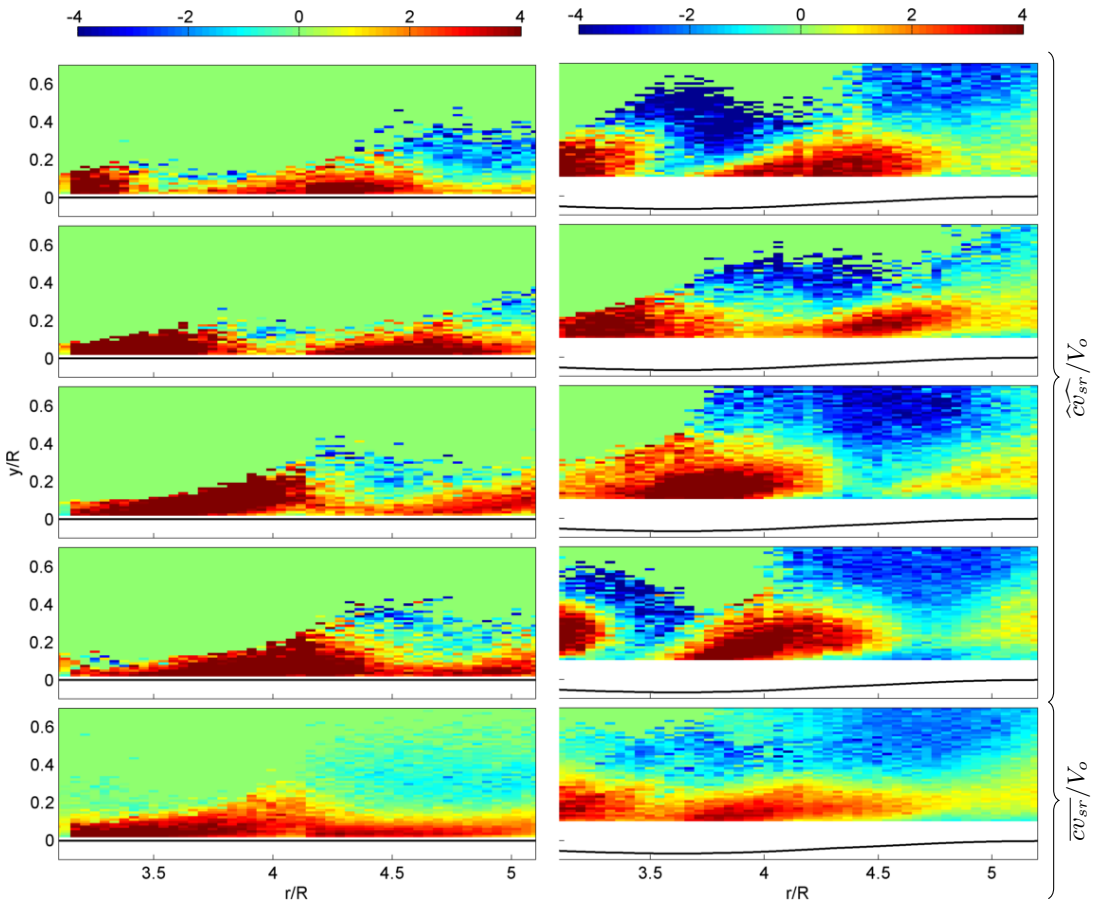

(a) Flat Bed (b) Eroded Bed

Figure 5.26: (a) Contours of phase-averaged and time-averaged radial drag (cv_{sr}/V_o) for a) flat bed case, and (b) eroded bed case. The four phase averages are calculated at $t/T = 0.25, t/T = 0.5, t/T = 0.75$ and $t/T = 1.0$

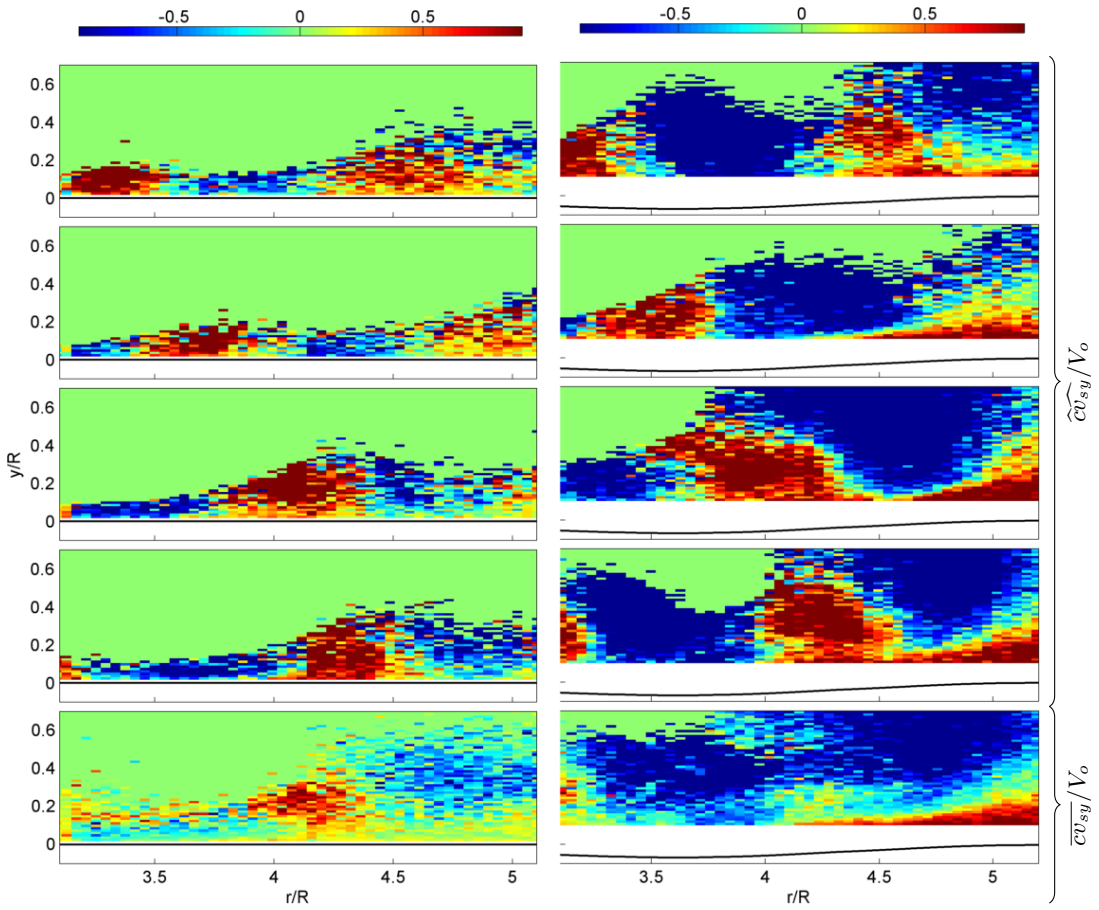

(a) Flat Bed (b) Eroded Bed

Figure 5.27: (a) Contours of phase-averaged and time averaged vertical drag ($\widetilde{cv_{sy}}/V_o$) for a) flat bed case, and (b) eroded bed case. The four phase averages are calculated at $t/T = 0.25, t/T = 0.5, t/T = 0.75$ and $t/T = 1.0$

radially outward due to the mean flow contributes greatly to the mean drag component. The drag is negative in the outer flow since the inertia of particles is much higher than that of the fluid phase and slip velocity becomes negative. In the time average contours, the inner flow is dominated by positive horizontal drag indicating momentum being transferred from the fluid to the particles while in the outer flow, the particles are leading and the momentum exchange is in the opposite direction.

The vertical mean drag in Fig. 5.27 shows alternating positive and negative regions associated with positive and negative vertical fluid velocity. The positive phase-averaged vertical drag component is about an order of magnitude lower than the corresponding radial component indicating that the mean flow of the wall jet has a stronger effect on momentum exchange between the phases when compared to the vortex-particle interaction.

The radial stochastic drag component Fig. 5.28 is an order of magnitude smaller than the mean drag in the outer region, but is of comparable magnitude along the bed surface, indicating large transient variations in particle concentrations and slip velocities near the point of impingement in the upstream plane for both flat and eroded bed cases. This could be representative of multiple particle collisions with the bed and other particles, increasing the variability in the slip velocity. It is also possible that this is an artifact of the measurement technique in the presence of low imaging quality in this region. The one argument against this, however, is that the fluctuation intensity of the particles is actually smaller near the wall than in the outer flow. If the trend were to be a result of noise contamination, the particle velocity fluctuation would be expected to be quite large in this region as well. The vertical stochastic drag component Fig. 5.29 is very noisy owing to variations in instantaneous slip velocity in the vertical direction and is of comparable

magnitude to the horizontal stochastic component.

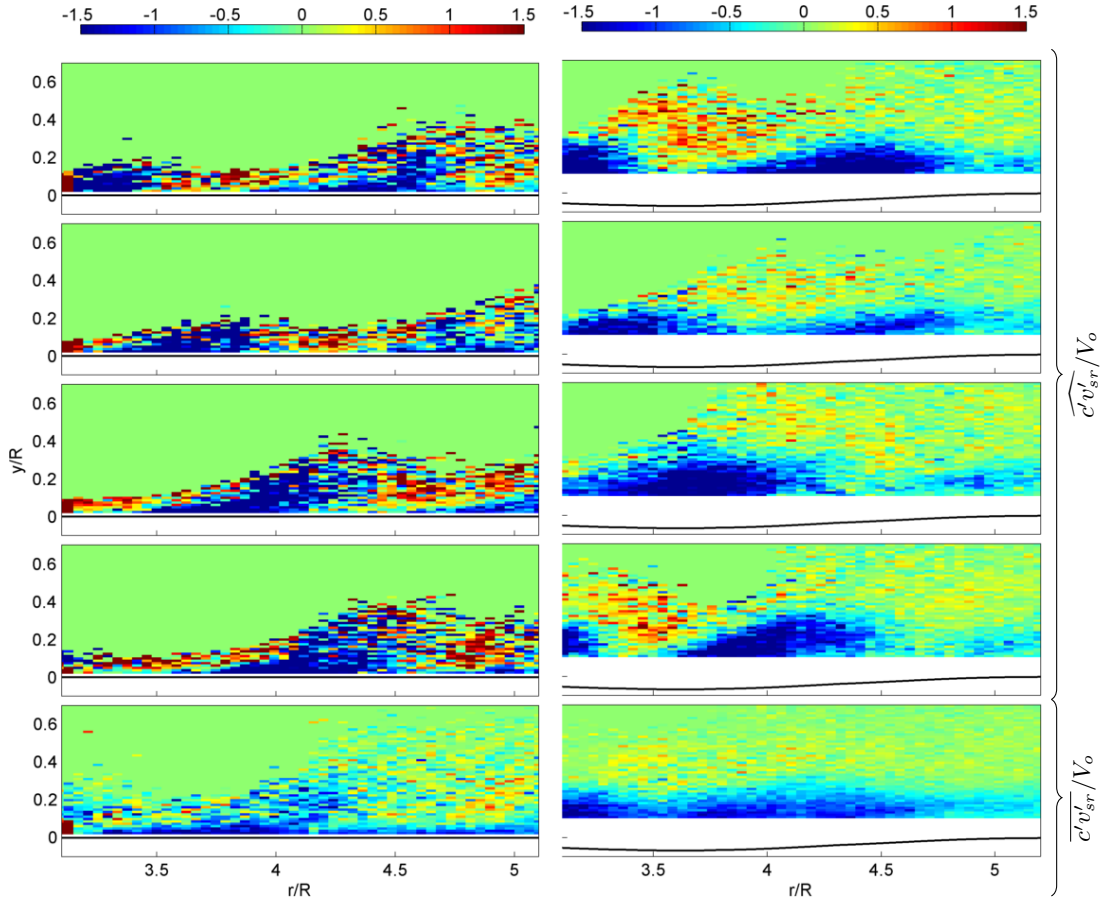

(a) Flat Bed (b) Eroded Bed

Figure 5.28: (a) Contours of phase and time averaged stochastic radial drag ($c'v'_{sr}/V_o$) for a) flat bed case, and (b) eroded bed case. The four phase averages are calculated at $t/T = 0.25, t/T = 0.5, t/T = 0.75$ and $t/T = 1.0$

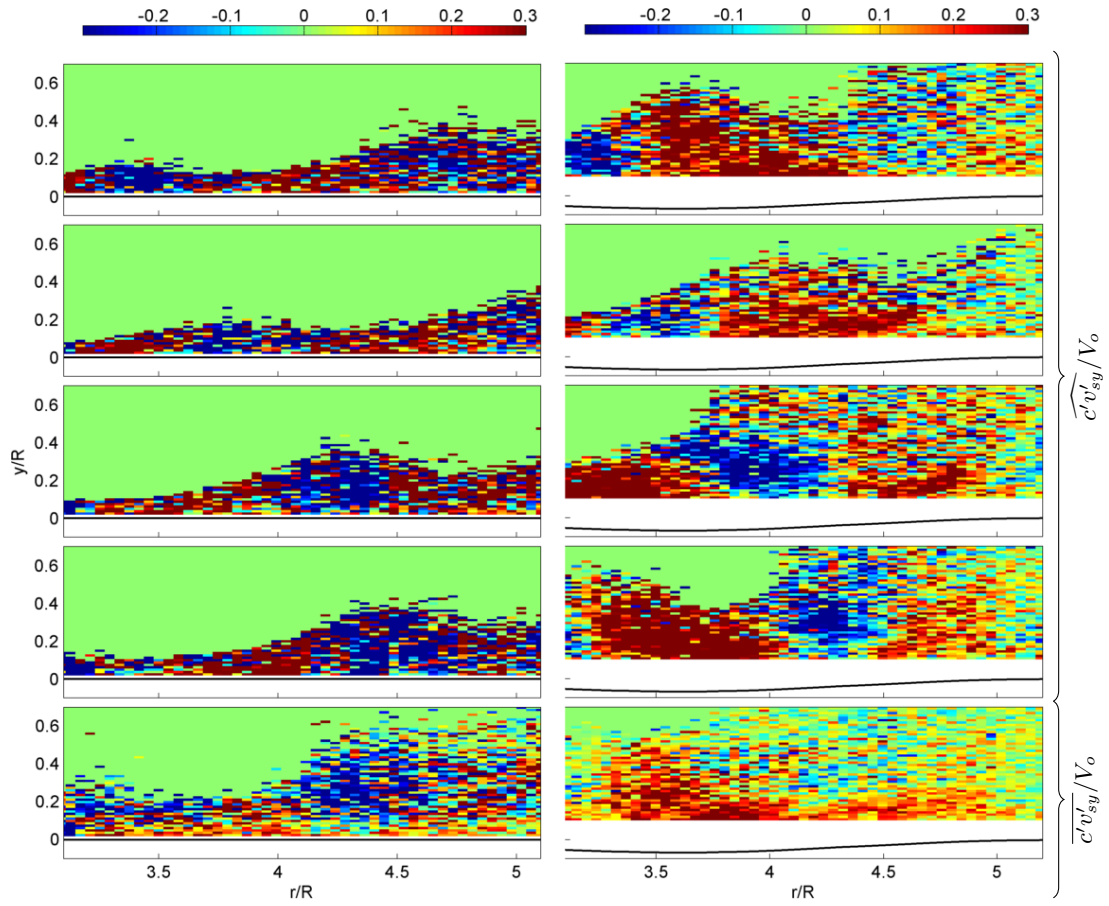

(a) Flat Bed (b) Eroded Bed

Figure 5.29: (a) Contours of phase and time averaged stochastic vertical drag ($c'v'_{sy}/V_o$) for a) flat bed case, and (b) eroded bed case. The four phase averages are calculated at $t/T = 0.25, t/T = 0.5, t/T = 0.75$ and $t/T = 1.0$

5.3 Velocity partitioning - Mesoscopic Eulerian formalism

Interactions between the dispersed and continuous phases affect not only volume fraction, but also lead to correlation of the velocities of neighboring particles. For small-inertia particles, neighboring velocities will be spatially correlated through the interactions with the same local fluid flow, while for large inertia with response times that are long compared to the fluid turbulence macroscales, neighboring particle velocities are uncorrelated since these particles maintain a stronger connection to their interactions with very distant, and independent, turbulent eddies. Février et al. (2005) [57] proposed a velocity partitioning approach to study the effect of particle inertia on spatial features of particle velocity. This mesoscopic Eulerian formalism (MEF) is based on the presumed chaotic behavior of inertial particles interacting with fluid turbulence and it enables the decomposition of the instantaneous particle velocity into two contributions.

1. **Mesoscopic Eulerian particle velocity field (MEPVF):** A turbulent contribution from an underlying continuous velocity field of the particulate phase that is local and time-dependent. This velocity is described in Eulerian coordinates which is shared by all the particles and accounts for interactions with the entire spectrum of fluid turbulent motions.

2. **Quasi-Brownian velocity distribution (QBVD):** A velocity distribution satisfying the assumption of molecular chaos, i.e. not correlated in space. A Lagrangian coordinate system is appropriate for the QBVD as it is associated with each particle separately.

Numerical results from Férvier et al. (2005) [57] showed that increasing particle inertia increased the contribution of quasi-Brownian component in gas-solid flows and that in the limiting case of large inertia, particle motion becomes stochastically equivalent to a Brownian motion with a random spatial distribution of positions and velocities. They also showed that the fraction of the kinetic energy residing in the mesoscopic field decreases with particle inertia as the square root of the ratio of the total particulate-phase kinetic energy to that of the fluid.

In MEF, the instantaneous Eulerian particle velocity field on a uniform grid is given by

$$\widetilde{v_p}(x,y) = \frac{1}{N_p(x,y)} \sum_{i=1}^{N_p} \delta((x - x_p^{(i)}), (y - y_p^{(i)})) v_p(x_p^{(i)}, y_p^{(i)}) \quad \text{where} \tag{43}$$

$\widetilde{v_p}(x,y)$ is the instantaneous MEPVF of the particle phase. Note that the mean of MEPVF is equal to the mean velocity of the particulate phase. The stochastic fluctuation of the particle velocity based on this instantaneous MEPVF and the ensemble average particle velocity then becomes

$$\widetilde{v_p}'(x,y) = \widetilde{v_p}(x,y) - \widehat{v_p}(x,y) \tag{44}$$

The average Eulerian kinetic energy of the dispersed phase can be defined as

$$\widehat{\widetilde{q_p^2}} = \frac{1}{2N_a} \sum_{1}^{N_a} \widetilde{v_p'}^2 \tag{45}$$

The quasi-Brownian component is then extracted from instantaneous particle velocity and the background MEPVF:

$$\delta v_p(x_p, y_p) = v_p(x_p, y_p) - \widetilde{v_p}(x,y) \quad \text{where} \tag{46}$$

$\delta v_p(x_p, y_p)$ is the Brownian velocity component. The corresponding kinetic energy for the Brownian component is given by

$$\widehat{\delta q_p{}^2}(x,y) = \frac{1}{2}\frac{1}{N_a(x,y)}\frac{1}{N_p(x,y)}\sum^{N_a}\sum_{i=1}^{N_p}\delta((x-x_p^{(i)}),(y-y_p^{(i)}))\delta v_p^2(x_p^{(i)},y_p^{(i)}) \tag{47}$$

Fig. 5.30 shows fluid kinetic energy for the flat and eroded bed cases. There is a large region of high kinetic energy associated with the location of the vortex at each phase angle. As the vortex undergoes stretching and dissipation, its kinetic energy decays with increasing radial distance. The high volume fraction in the eroded bed case is responsible for diminished fluid kinetic energy as the energy residing in large scale vortex structure is absorbed by the particles. This is especially evident near the bed where the reduction in fluid kinetic energy is maximum owing to high local particle volume fraction. Contours of particle total kinetic energy (Fig. 5.31) show a strong correlation with the kinetic energy of the vortex. By employing velocity partitioning, one can visualize the MEPVF and QBVD components of kinetic energy in flat bed and eroded bed cases. Fig. 5.32 shows the MEPVF component as a fraction of total particle kinetic energy. The dominant existence of MEPVF for both flat and eroded bed cases is anticipated since the particle motion with an underlying fluid flow is characterized by spatially correlated motions, especially in the outer flow where the entrained particles extract energy from the surrounding fluid. The inertia associated with these particles is not high enough to assume a chaotic and uncorrelated behavior even though the fluid is lagging in that region. The contributions by QBVD are more subtle (Fig. 5.33). Very close to the bed, the Brownian component dominates due to high particle concentration, high velocity gradients and inter-particle as well as particle bed collisions. The spatial velocity correlations are increasingly affected by the

QBVD, especially for small separations. This is evident when looking at the eroded bed case where high volume fraction (and small separation) resulted in a higher Brownian component at similar spatial coordinates. At $r/R > 4.2$ and $y/R < 0.2$, nearly 30% of the total energy in the eroded bed case is from QBVD contribution where as in the flat bed case, the maximum QBVD contribution is about 15% and it does not penetrate as high into the outer flow.

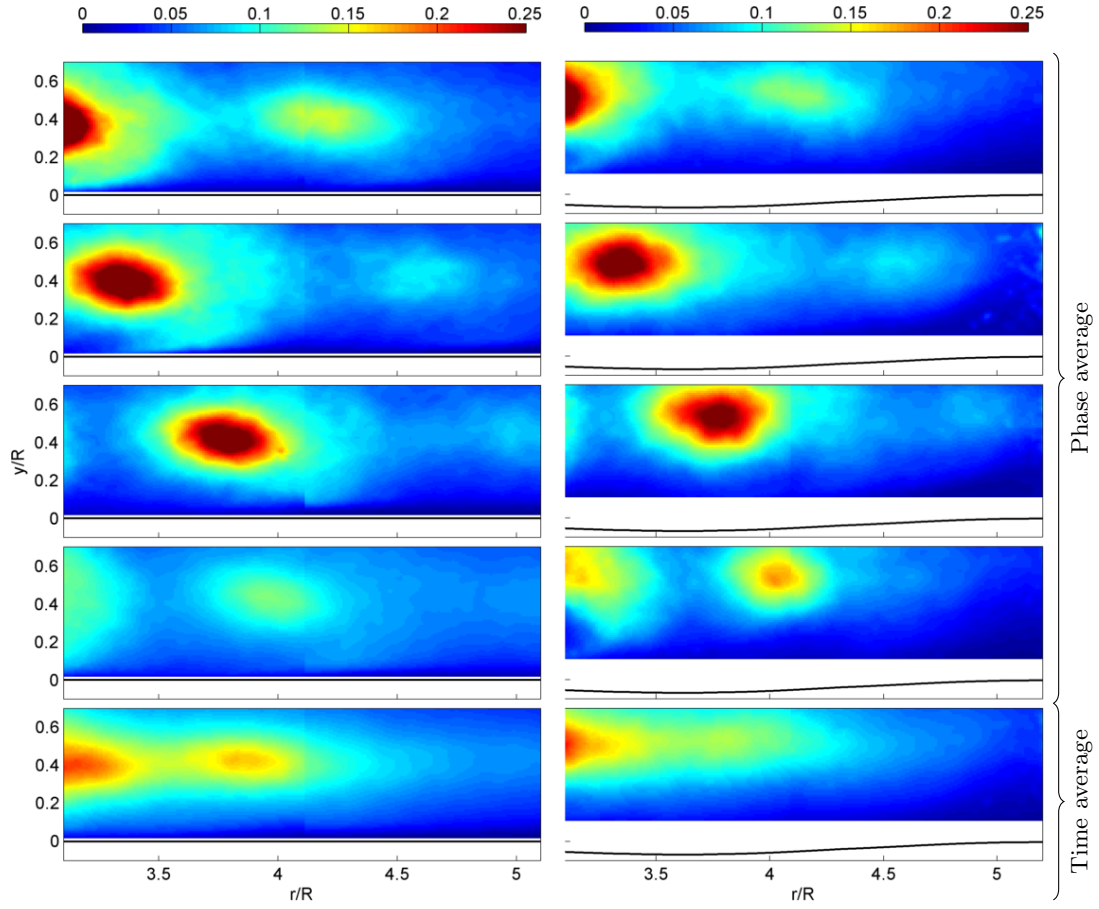

(a) Flat Bed (b) Eroded Bed

Figure 5.30: (a) Contours of fluid kinetic energy q_f^2/V_o^2 for a) flat bed case, and (b) eroded bed case. The four phase averages are calculated at $t/T = 0.25, t/T = 0.5, t/T = 0.75$ and $t/T = 1.0$

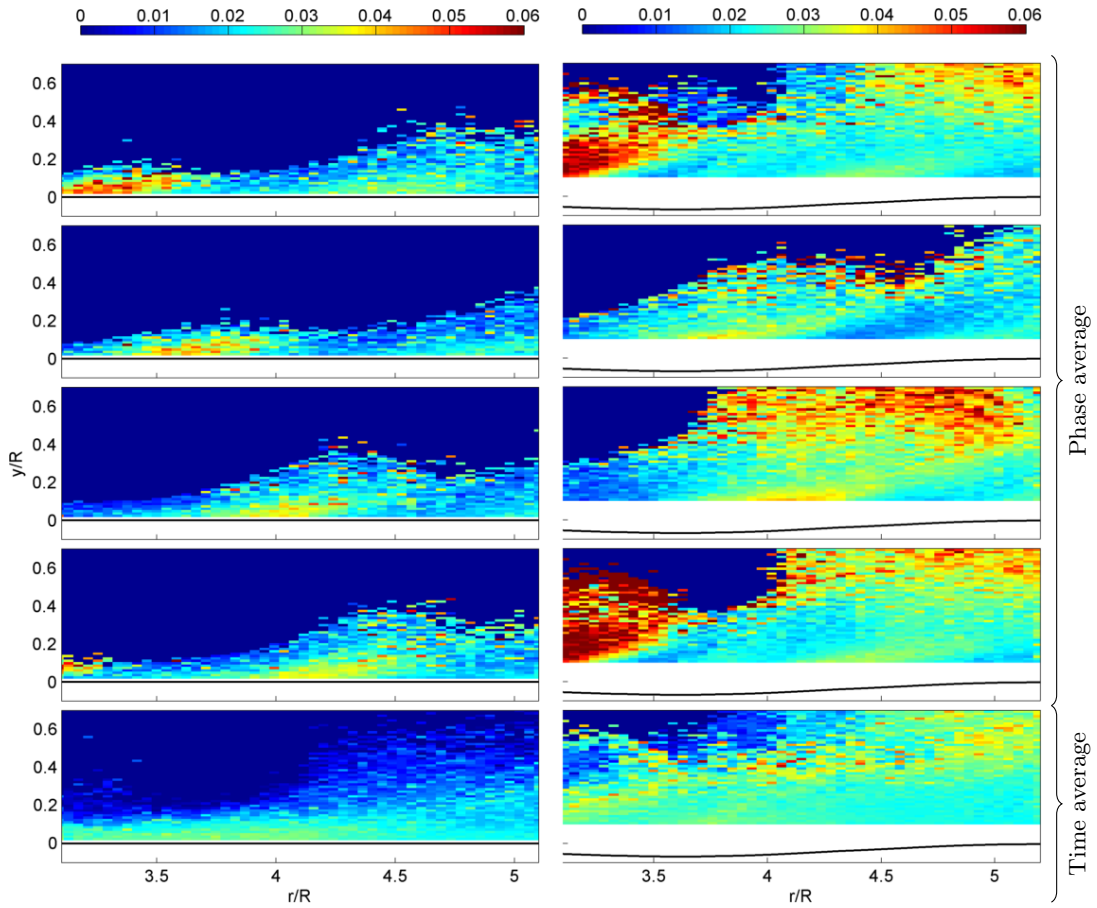

(a) Flat Bed (b) Eroded Bed

Figure 5.31: (a) Contours of total particle kinetic energy q_p^2/V_o^2 for a) flat bed case, and (b) eroded bed case. The four phase averages are calculated at $t/T = 0.25, t/T = 0.5, t/T = 0.75$ and $t/T = 1.0$

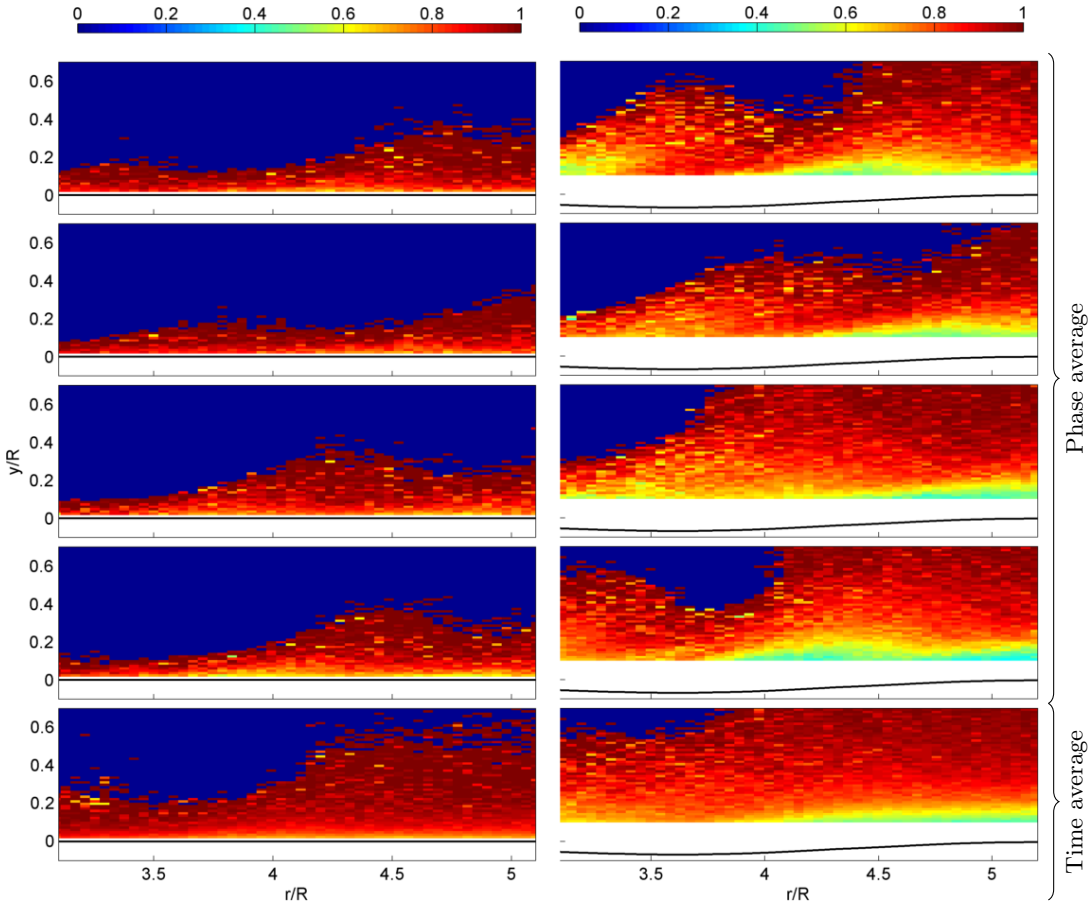

(a) Flat Bed (b) Eroded Bed

Figure 5.32: (a) Contours of particle Eulerian kinetic energy as a fraction of total particle kinetic energy $\widetilde{q_p^2}/q_p^2$ for a) flat bed case, and (b) eroded bed case. The four phase averages are calculated at $t/T = 0.25, t/T = 0.5, t/T = 0.75$ and $t/T = 1.0$

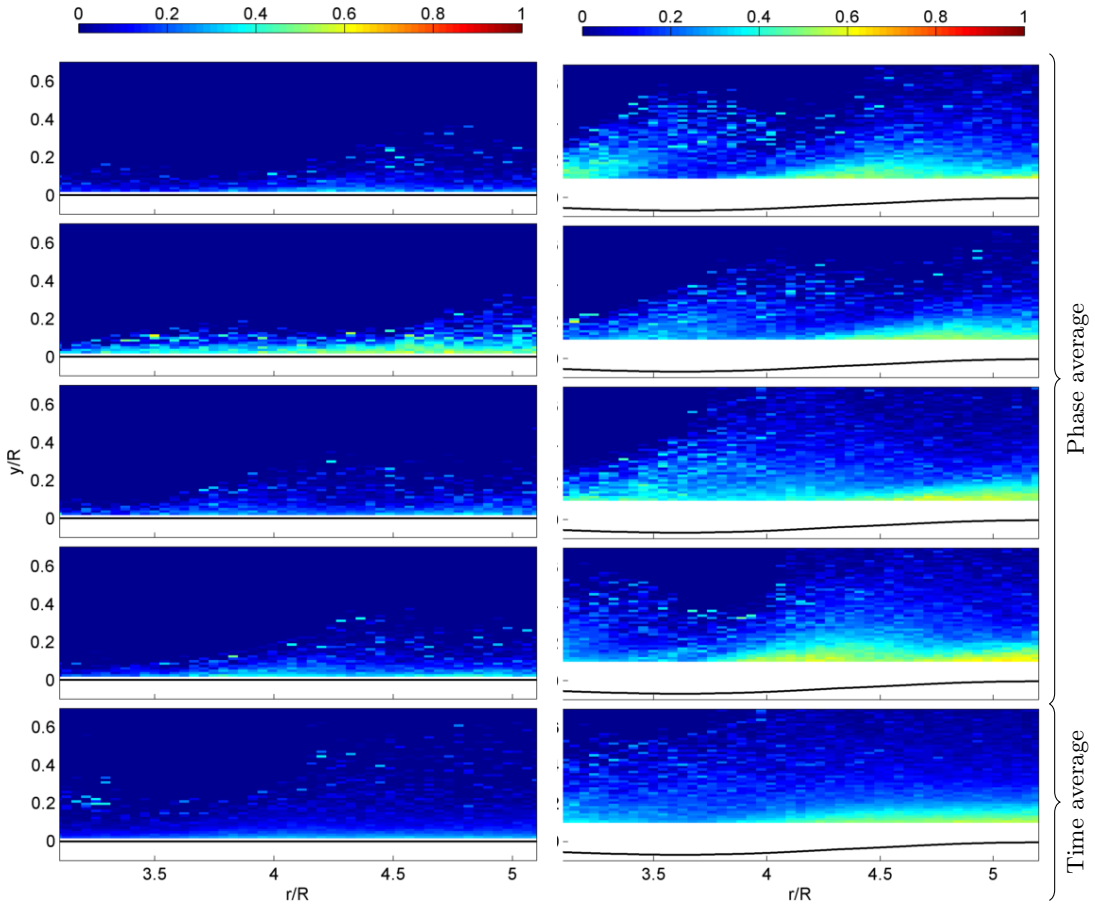

(a) Flat Bed (b) Eroded Bed

Figure 5.33: (a) Contours of particle Brownian kinetic energy as a fraction of total particle kinetic energy $\delta q_p^2/q_p^2$ for a) flat bed case, and (b) eroded bed case. The four phase averages are calculated at $t/T = 0.25, t/T = 0.5, t/T = 0.75$ and $t/T = 1.0$

6 Conclusions

6.1 Summary

Detailed dual phase PIV measurements of a forced impinging jet on a mobile sediment bed have been studied with the goal of understanding the process of particle mobilization and sediment suspension. Due to the transient and three-dimensional nature of the flow, integration of several multi-phase PIV techniques was required to make quantitative measurements. The single phase fluid flow was characterized to study the vortex trajectory as well as its circulation strength. Simultaneous velocity measurements of the fluid and dispersed phase in two vertical planes were then analyzed to examine the role of vortex interaction and its subsequent breakdown on sediment transport process. Two cases, a nominally flat bed and an eroded bed were examined to study the influence of the topology of bed surface on particle suspension. Particular emphasis was placed on particle-turbulence interaction within the suspension.

6.2 Contributions of this work

1. Implementation as well as validation of phase-separation and super-resolution PIV routines to analyze particle suspension mechanisms in gas-solid flows with moderate suspended loads and high velocity gradients.

2. Calibration of measurement volume to estimate the effective light sheet thickness used in the calculation of local volume fractions.

3. Quantification of interaction of a coherent, large-scale fluid structure with a mobile sediment bed in gas-solid flows.

4. Investigation of the effect of evolving bed-forms on sediment transport and its implications.

5. Detailed analysis of particle-turbulence interactions and momentum coupling between the suspended particle and ambient fluid.

6.3 Specific conclusions

6.3.1 Single phase flow

The vortex ring follows a hyperbolic trajectory and undergoes intensification as it approaches the ground due to vortex stretching phenomenon. As it approached the boundary layer, it created an adverse pressure gradient that resulted in separation and the formation of a secondary counter-rotating vortex. As the vortex continued its radial motion, it interacted with the ground plane and underwent 3-dimensional destabilization and eventually dissipated beyond $r/R > 4.7$ under current experimental conditions.

6.3.2 Dual-Phase PIV experiments - phase separation and PTV

Phase separation routine based on second order intensity gradients and saturation criteria has been implemented to identify and separate the dispersed phase particles and carrier phase tracers. Parametric experiments were conducted to establish the robustness of the routine using different particle sizes and the algorithm has been fine-tuned to identify more than 99% of dispersed phase particles under dilute conditions. Super-resolution PIV or hybrid PIV/PTV technique has been implemented to estimate particle velocities. Artificial images with dispersed phase particles released into a Taylor-Green vortex flow at

different Stokes numbers and particle concentrations have been used to validate the particle identification and particle tracking routines.

6.3.3 Volume fraction and particle fluxes

The vortex played a significant role in the particle mobilization and uplift process whereas the mean flow determined the radial expansion of the suspension. A strong spatial correlation between the vortex and plumes of mobilized particles is evident from contours of volume fraction. The results show a predominantly radial scouring of sediment particles, which eventually get entrained, by the vortex into suspension near the point of closest approach. Slip velocity is positive close to the bed indicating that the particles are lagging in the inner flow. As they move into the outer flow, these particles gain momentum from the surrounding fluid and lead the fluid, especially in the vertical direction owing to the vertical fluid velocities induced by the vortex. The eroded bed case showed higher volume fractions due to the presence of a crest at $r/R \approx 3.0$.

The radial particle flux was predominantly positive throughout the domain and depth integrated particle flux showed that the flat bed case has an evolving suspension where number of particles entering into suspension at all radial locations is higher than the number of particles that are settling down. In the eroded bed case, the suspension has reached an equilibrium state and the time-averaged particle flux had a fairly constant value at all radial locations. Contours of vertical flux showed regions where particles were returning to the bed with velocities higher than the settling velocities due to entrainment by the counter-rotating secondary vortex. This caused the "bombardment" phenomenon that ejected even more particles from the surface.

6.3.4 Particle-Turbulence Interaction

The presence of particles modulated both the mean and stochastic components of the fluid velocities. The fluid velocity was attenuated close to the bed where the volume fraction was high and while it was augmented in the outer flow, where the local volume fraction was relatively low. The fluid RMS velocities and fluid Reynolds stresses showed similar behavior and the modulation increased with increasing radial distance for both flat and eroded bed cases, indicating that it is a strong function of local volume fraction within the flow.

6.3.5 Momentum transfer

Phase-averaged and stochastic particle-fluid drag components were estimated and it was found that the radial phase-averaged drag component is dispersed into the upwash region of the flow and reaches a maximum as a large positive flux of particles gets ejected from the surface in the upstream plane for both flat and eroded bed cases. The drag is negative in the outer flow due to increased inertia of suspended particles. The phase-averaged vertical drag has alternating positive and negative regions that strongly correlate to the vertical fluid velocity. Conversely, the fluctuating drag component is highest along the bed surface indicating large transient variations in particle concentrations and slip velocities near the point of impingement.

6.3.6 Velocity Partitioning and MEF

Mesoscopic Eulerian formalism showed that the Eulerian component of particle velocity dominates in the outer flow where the particles have a uniform background motion. Close to the bed, the Brownian component takes over

due to high velocity gradients, high volume fraction, particle-particle collisions and particle-bed collisions. The behavior is more chaotic and is spatially uncorrelated with the velocities of neighboring particles.

6.4 Future work

This work has examined the influence of vortex superimposed over a mean flow on particle suspension. The present work focused on a limited number of parameters that control this complex flow there are definitely a lot of avenues to pursue in order to understand this problem and validate/in-validate these results.

1. These experiments were conducted at threshold mean jet conditions for one particle size at a particular stand-off height. As the mean velocity conditions and the vorticity embedded within the flow are changed, the vortex trajectories, bed topology and suspension patterns will change. As the particle size increases, so does its inertia and the chaotic behavior within the suspension becomes more prominent. However as the particle size reduces, cohesion and tribo-electric charging become issues and suspension of cohesive particles is much more complicated. Lowering the standoff height (in steps or continuously) will make the vortex trajectory flatter and at the same time, the vortex will not have enough time to strengthen before it interacts with the ground. Results of such experiments with different permutations and combinations of experimental parameters will definitely be of interest.

2. The present work provided a large data base of detailed two-phase flow measurements of vortex impinging on sediment bed. These results can be used to validate numerical schemes and those models can then be used to

extrapolate the results to the more complex and full scale brownout flow. These results show that the volume fractions are of the order of 10^{-6} in the outer flow and 10^{-5} in the inner flow. So an expensive two-way coupling scheme can be implemented to model a thin layer close to the bed and a cheaper one-way coupling model can be used to describe the suspension in the outer flow.

3. Calibration of thickness of the measurement volume needs further detailed analysis to account for the variations in light sheet thickness across the domain as well as attenuation/augmentation of light sheet due to scattering from the particles and the bed surface.

4. Volumetric measurements of concentration and velocities of the phases involved would provide an unprecedented level of understanding of these types of flows. Recently, with the introduction of TOMO-PIV, 3-dimensional simultaneous velocity measurements in small volumes has become a possibility. Analyzing 3-dimensional nature of the vortex interaction with the sediment bed and the resulting suspension would vastly improve our current understanding of this flow.

References

[1] Johnson, B., Leishman, J.G and Sydney, A., Investigation of sediment entrainment using dual-phase, high-speed particle image velocimetry. *J. Am. Helicopter Society* **55** (2010):042003.

[2] Syal, M., Development of Lagrangian-Lagrangian Methodology to Predict Brownout Dust Clouds. *PhD Thesis, University of Maryland* (2012).

[3] Bagnold, R. A., An approach to the sediment transport problem from general physics. *Geological Survey Professional Paper*, **422-I** (1966).

[4] Shields, I. A., Anwendung der Aehnlichkeitsmechanik and der Turbulenzforschung auf die Geschiebebewegung. *Mitt. Preuss. Versuchanstalt* (1936).

[5] White, S.J., Plane bed thresholds for fine grained sediments. *Nature, London*, **228(5267):152-3** (1970).

[6] Brownlie, W.R., Flow depth in sand-bed channels. *Journal of Hydraulic Engineering*, **109: 7** (1983), 959-990.

[7] Meyer-Peter, E. and Müller, R., Formulas for bed-load transport. *Proc. 2nd IAHR Congress, Stockholm*, (1948).

[8] Wilson, K. C., Bed-load transport at high shear stress. *Journal of the hydraulics division*, **92(HY6)** (1966), 49-59.

[9] Ribberink, J. S., Bed-load transport for steady flows and unsteady oscillatory flows. *Coastal Eng.*, **34** (1998), 59-82.

[10] Elghobashi, S., On predicting particle-laden turbulent flows. *Applied Scientific Research*, **52** (1994), 309-329.

[11] Elghobashi and S., Truesdell, G., On the two-way interaction between homogeneous turbulence and dispersed solid particles. I: Turbulence modification.*Physics of Fluids*, **5(7)** (1993), 1790-1801.

[12] Eaton, J. and Fessler, J., Preferential concentration of particles by turbulence. *International Journal of Multiphase Flow*, **20(1)** (1994), 169-209.

[13] Drew, D. A., Mathematical modeling of two-phase flow. *Annual Review of Fluid Mechanics*, **15** (1983), 261-291.

[14] Longo,S., Two-phse flow modeling of sediment motion in sheet-flows above plane beds. *Journal of Hydraulic Engineering*, **131(5)** (2005), 366-379.

[15] Richardson, J. F. and Zaki, W.N., Sedimentation and fluidization, *Trans. Instn. Chem. Egnrs.*, **32** (1954), 35-53.

[16] Squires, K. and Eaton, J., Particle response and turbulence modification in isotropic turbulence. *Physics of Fluids*, **2(7)** (1990), 1191-1203.

[17] Squires, K. and Eaton, J., Effect of selective modification of turbulence on two-equation models for particle-laden turbulent flows. *Trans. ASME I: Journal of Fluids Engineering*, **116** (1994), 778-784.

[18] Boivin, M., Simonin, O., and Squires, K., Direct numerical simulation of turbulence modulation by particles in isotropic turbulence. *Journal of Fluid Mechanics*, **375** (1998), 235-263.

[19] Dritselis, C.D. and Vlachos, N. S., Numerical study of educed coherent structures in the near-wall region of a particle-laden channel flow. *Experiments in Fluids*, **53** (2012), 1385-1403.

[20] Amoudry, L., Hsu, T.-J. and Liu, P. L.-F., Two-phase model for sand transport in sheet flow regime. *Journal of Geophysical Research*, **113** (2008), C03011.

[21] Ozdemir, C. E., Hsu, T.-J. and Balachander, S., Simulation of fine sediment transport in oscillatory boundary layer. *Journal of Hydro-environment Research*, **3** (2010), 247-259.

[22] Soldati, A. and Marchioli, C., Sediment transport in steady turbulent boundary layers: Potentials, limitations, and perspectives for Lagrangian tracking in DNS and LES. *Advances in Water Resources*, **48** (2012), 18-30.

[23] Sumer, B.M. and Oğuz, B., Particle motions near the bottom in turbulent flow in an open channel. *Journal of Fluid Mechanics*, **86** (1978), 109-127.

[24] Niño, Y. and Garcia, M. H., Experiments on particle-turbulence interactions in the near-wall region of an open channel flow: implications for sediment transport. *Journal of Fluid Mechanics*, **326** (1996), 285-319.

[25] Kiger, K. T. and Pan, C., Suspension and turbulence modification effects of solid particulates on a horizontal turbulent channel flow. *Journal of Turbulence*, **3, N19** (2002).

[26] Hout, R., Time-resolved PIV measurements of the interaction of polystyrene beads with near-wall-coherent structures in a turbulent channel flow. *International Journal of Multiphase Flow*, **37** (2011), 346-357.

[27] Li, J., Wang, H. and Liu, Z., An experimental study on turbulence modification?in the near-wall boundary layer of a dilute gas-particle channel flow. *Physics of Fluids*, **20:055** (2008), 103-112.

[28] Sutherland, A., Proposed mechanism for sediment entrainment by turbulent flows. *Journal of Geophysical Research*, **72** (2008), 6183-6194.

[29] Chung, J.N. and Troutt, T. R., Simulation of particle dispersion in an axisymmetric jet. *Journal of Fluid Mechanics*, **186** (1988), 199-222.

[30] Munro, R.J., Bethke, N. and Dalziel, S. B., Sediment resuspension and erosion by vortex rings. *Physics of Fluids*, **21** (2009), 046601.

[31] Bethke, N. and Dalziel, S. B., Resuspension onset and crater erosion by a vortex ring interacting with a particle layer. *Physics of Fluids*, **24** (2012), 063301.

[32] Nathan, N. and Green, R., Measurements of a Rotor Flow in Ground Effect and Visualisation of the Brownout Phenomenon. *64th Annual Forum Proceedings of the American Helicopter Society, Montreal Canada*, April 29-May 1 2008.

[33] Johnson, B., Leishman, J. G. and Sydney, A., Investigation of Sediment Entrainment using Dual-Phase, High-Speed Particle Image Velocimetry. *Journal of the American Helicopter Society*, textbf55 (2010).

[34] Sydney, A., Baharani, A. and Leishman, J. G., Understanding Brownout Using Near-Wall Dual-Phase Flow Measurements. *67th Annual Forum Pro- ceedings of the American Helicopter Society*, April 29-May 1 2008.

[35] Thomas, S., A GPU-accelerated, hybrid FVM-RANS methodology for modeling rotorcraft brownout. *PhD Thesis, University of Maryland* (2013).

[36] Geiser, J., Development of a Lagrangian-Lagrangian Methodology to Predict Brownout Dust Clouds. *Masters' Thesis, University of Maryland* (2011).

[37] Brücker, C. *PIV in two-phase flows; in: Particle Image Velocimetry and associated techniques, Lecture Series 2000-01 von Karman Institute for Fluid Dynamics, Rhode Saint Genése, Belgium*

[38] Philip, O.G, Schmidl, W.D. and Hassan, Y.A., Development of high speed particle image velocimetry technique using fluorescent tracers to study steam bubble collapse, *Nucl. Eng. Des* **149** (1994), 375-385.

[39] Lindken, R. and Merzkirch, W., A novel PIV technique for measurements in multiphase flows and its application to two-phase bubbly flows, *Experiments in Fluids* **33** (2002), 814-825.

[40] Kiger, K. and Pan, C., PIV technique for the simultaneous measurement of dilute two-phase flows, *Journal of Fluids Engineering* **122** (2000), 811-818.

[41] Khalitov, D. and Longmire, E., Simultaneous two-phase PIV by two-parameter phase discrimination, *Experiments in Fluids* **32** (2002), 252-268.

[42] Keane, R.D., Adrian, R.J. and Zhang, Y., Super-resolution particle image velocimetry, *Meas Sci Technology* **6** (1995), 754-768.

[43] Cowen, E.A. Monismith, S.G., A hybrid digital particle tracking velocimetry technique, *Experiments in Fluids* **22** (1997), 199-211.

[44] Westerweel, J. and Scarano, F., Universal outlier detection for PIV data, *Experiments in Fluids* **39** (2005), 1096-1100.

[45] Kiger, K. T. and Knowles, P., Quantification of Dispersed Phase Concentration Using Light Sheet-Based Imaging Methods, *15th International Symposium on Applications of Laser Techniques to Fluid Mechanics* Lisbon, Portugal 2010.

[46] Krishnan, G. and Mohseni, K., On a Radial Wall Jet Formed by a Normally-Impinging Round Synthetic Jet, *47th AIAA Aerospace Sciences Meeting Including The New Horizons Forum and Aerospace Exposition* Orlando, Florida, 2009.

[47] Kaftori, D., Hetsroni, G. and Banerjee, S., The effect of particles on wall turbulence, *Int. J. Multiphase Flow* **24, 3** (1998), 359-386.

[48] Kaftori, D., Hetsroni, G. and Banerjee, S., Particle behavior in the turbulent boundary layer. II. Velocity and distribution profiles, *Physics of Fluids* **7** (1995), 1107-1121.

[49] Rashidi, M., Hetsroni, G. and Banerjee, S., Particle?turbulence interaction in a boundary layer, *Int. J. Multiphase Flow* **16** (1990), 935-949.

[50] Wu, Y., Wang, H., Liu, Z., Li, J., Zhang, L. and Zheng, C., Experimental investigation on turbulence modification in a horizontal channel flow at relatively low mass loadings, *Acta Mech Sinica* **22** (2006), 99-108.

[51] Tsuji, Y. and Morikawa, Y., LDV measurements of an air-solid two-phase flow in a horizontal pipe, *Journal of Fluid Mechanics* **120** (1982), 385-409.

[52] Tanière, A. Oesterlé, B. and Monnier ,J. C., On the behaviour of solid particles in a horizontal boundary layer with turbulence and saltation effects, *Experiments in Fluids* **23** (1997), 463-471.

[53] Kulick, J.D., Fessler, J. R. and Eaton, J. K., Particle response and turbulence modification in fully developed channel flow, *Journal of Fluid Mechanics* **277** (1994), 109-134.

[54] Righetti, M. and Romano, G. P., Particle?fluid interactions in a plane near-wall turbulent flow, *Journal of Fluid Mechanics* **505** (1994), 93-121.

[55] Chan-Braun, C., García-Villalba, M. and Uhlmann, M., Numerical simulation of fully resolved particles in rough-wall turbulent open channel flow, In: *Proceedings of the 14th international conference on multiphase flow* (2010) Tampa, USA.

[56] Armenio, V. and Fiorotto, V., The importance of the forces acting on particles in turbulent flows, *Physics of Fluids* **13(8)** (2001), 2437-2440.

[57] Férvier, P., Simonin, O. and Squires, K.D., Partitioning of particle velocities in gas?solid turbulent flows into a continuous field and a spatially uncorrelated random distribution: theoretical formalism and numerical study, *Journal of Fluid Mechanics* **533** (2005), 1-46.